



INVESTIGATION OF THE EXPANSION OF THE TROPICAL ZONE AND ITS  
EFFECT ON CLIMATE IN THAILAND



A Thesis Submitted in Partial Fulfillment of the Requirements  
for Doctor of Philosophy (PHYSICS)  
Department of PHYSICS  
Graduate School, Silpakorn University  
Academic Year 2021  
Copyright of Silpakorn University

การศึกษาการขยายของเขตร้อนชื้นและผลต่อภูมิอากาศในประเทศไทย



วิทยานิพนธ์นี้เป็นส่วนหนึ่งของการศึกษาตามหลักสูตรปรัชญาดุษฎีบัณฑิต  
สาขาวิชาฟิสิกส์ แบบ 1.1 ปรัชญาดุษฎีบัณฑิต  
ภาควิชาฟิสิกส์  
บัณฑิตวิทยาลัย มหาวิทยาลัยศิลปากร  
ปีการศึกษา 2564  
ลิขสิทธิ์ของมหาวิทยาลัยศิลปากร

INVESTIGATION OF THE EXPANSION OF THE TROPICAL ZONE  
AND ITS EFFECT ON CLIMATE IN THAILAND



By  
MR. Wanchalerm CHANALERT

A Thesis Submitted in Partial Fulfillment of the Requirements  
for Doctor of Philosophy (PHYSICS)  
Department of PHYSICS  
Graduate School, Silpakorn University  
Academic Year 2021  
Copyright of Silpakorn University

Title Investigation of the expansion of the tropical zone and its effect on  
climate in Thailand  
By Wanchalerm CHANALERT  
Field of Study (PHYSICS)  
Advisor Professor Dr. Serm Janjai

---

Graduate School Silpakorn University in Partial Fulfillment of the  
Requirements for the Doctor of Philosophy

..... Dean of graduate school

(Associate Professor Jurairat Nunthanid, Ph.D.)

Approved by

..... Chair person

(Assistant Professor Dr. Itsara Masiri )

..... Advisor

(Professor Dr. Serm Janjai )

..... External Examiner

(Associate Professor Dr. Wilawan Kamharn )



60306802 : Major (PHYSICS)

Keyword : Climate change, Tropical expansion, Greater Mekong Subregion, ERA, Convection, Hadley circulation, High cloud cover, Standardized Precipitation Index

MR. WANCHALERM CHANALERT : INVESTIGATION OF THE EXPANSION OF THE TROPICAL ZONE AND ITS EFFECT ON CLIMATE IN THAILAND THESIS ADVISOR : PROFESSOR DR. SERM JANJAI

Amongst the issues associated with global climate change, the expansion of the tropics has become increasingly important. This expansion is normally demonstrated in the form of changes in the Hadley circulation. The first part of the study will show a series of data sets consisting of brightness temperature from HIRS-UTWV, high cloud cover, precipitation and evaporation from ERA-Interim reanalysis data, deep cloud convection from ISCCP, and aerosol optical depth from MERRA were used to examine the poleward expansion of the Hadley cell in the Greater Mekong Subregion (GMS) over the period 1979 to 2018. A pronounced poleward tropical expansion was found during the winter season but no trends were found for the summer season. Much of the poleward movement appears to be dominated by equatorial convection as measured by high cloud cover. There are some evidences of a shrinking dry zone where precipitation minus evaporation is less than 0. The second part of the study aims to investigate the changes of the Hadley circulation using high cloud cover from the ERA-Interim reanalysis data over the globe. Trends of zonal-mean cloud cover computed over the period 1979-2017 in both hemispheres show that poleward expansion of the Hadley circulation is about 1.6 and 1.2 degree of latitude per 39 years in northern hemisphere and southern hemisphere, respectively. In addition, the expansion for all four seasons was also analysed. The analysis results show that poleward expansion occurs mostly in all seasons and the expansion of the Hadley circulation results in a poleward expansion of the subtropical dry regions. The third part of the study presents the effect of the tropical expansion on climate in Thailand. We calculated the Standardized Precipitation Index (SPI) over Thailand to indicate flood and drought. Then we estimated the correlation between the SPI and tropical expansion indices. The result suggested that the SPI trend is increased in all regions of Thailand and the whole country according to the tropical expansion. That is the tropical expansion induces more convection in the equatorial zone which causes more rain in the Thailand region.

## ACKNOWLEDGEMENTS

A thesis entitled “Investigation of the expansion of the tropical zone and its effect on climate in Thailand” is submitted in partial fulfillment of the requirements for the degree of Doctor of Philosophy (Physics), Graduate School, Silpakorn University.

I would like to thank the Royal Golden Jubilee (RGJ) Ph.D. program of TSRI (no. PHD/0201/2559) for financially supporting my Ph.D. research.

I would like to express my sincere thanks to my advisor, Professor Dr. Serm Janjai for their helpful guidance, enthusiastic encouragement, and support throughout this study. I am also highly thankful to Asst. Prof. Dr. Sumaman Buntoung and Asst. Prof. Dr. Korntip Tohsing for their valuable suggestions and generous encouragement throughout this research work.

I am deeply indebted to Asst. Prof. Dr. Manuel Nunez from the University of Tasmania, Australia for his guiding assistance on the necessary technique for my research.

I would like to express my gratitude to Professor Dr. Jie Cao from Yunnan University, China for advising on the research. I also would like to thank Dr. Shu Gui for hosting and giving advice. I greatly appreciate their effort to be helpful throughout my visit to Yunnan University.

Besides my above acknowledgments, I would like to thank my thesis committee: Asst. Prof. Dr. Itsara Masiri and Assoc. Prof. Dr. Wilawan Kamharn for their insightful comments and valuable suggestions.

My sincere thanks to all researchers and students in the Solar Energy Research Laboratory of Silpakorn University for their encouragement, and friendship throughout my studying time.

Finally, I wish to thank my family for their support and entirely care.

MR. Wanchalerm CHANALERT



# TABLE OF CONTENTS

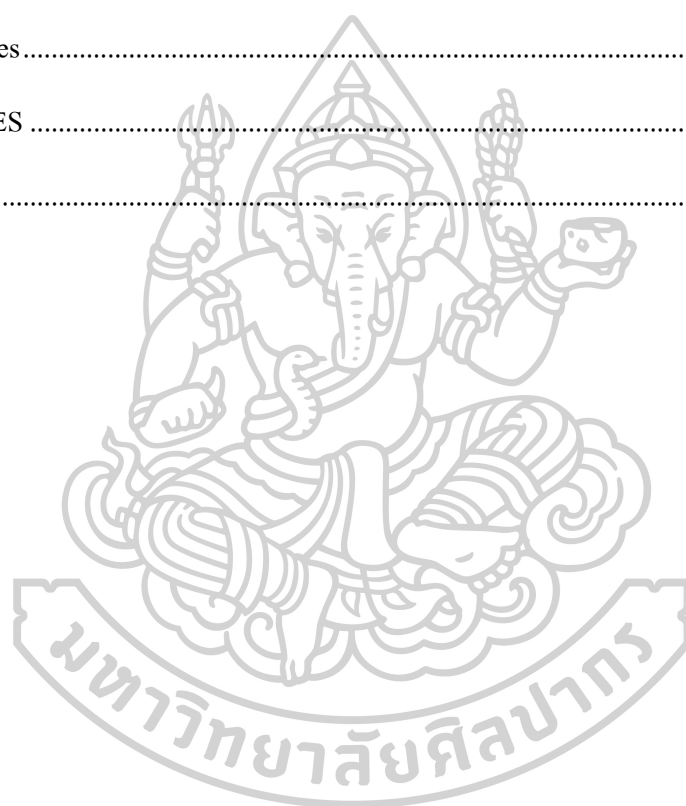
	<b>Page</b>
ABSTRACT.....	D
ACKNOWLEDGEMENTS.....	E
TABLE OF CONTENTS.....	F
Chapter 1.....	1
Introduction.....	1
1.1 Rationale of the study.....	1
1.2 Objectives.....	2
1.3 Organization of this thesis.....	2
Chapter 2.....	3
Theory and literature review.....	3
2.1 Atmospheric circulation.....	3
2.2 Intertropical convergence zone (ITCZ).....	4
2.3 Greater Mekong Subregion.....	7
2.4 Literature reviews.....	11
Chapter 3.....	18
The Greater Mekong Subregion (GMS) and Tropical Expansion: A Regional Study of Convection and Precipitation.....	18
3.1. Introduction.....	18
3.2 Data and methodology.....	21
3.2.1 Data.....	22
3.2.1.1 HIRS-UTWV.....	22

3.2.1.2 ISCCP .....	23
3.2.1.3 ERA-Interim .....	23
3.2.2 Methodology .....	25
3.2.2.1 Comparison of the ERA-Interim and TRMM precipitation data.....	25
3.2.2.2 Data processing and display .....	26
3.2.2.3 Metrics used for expansion indices.....	27
3.3 Results .....	30
3.3.1 Precipitation (P) .....	30
3.3.2 Precipitation minus evaporation (P-E).....	32
3.3.3 Brightness temperature ( $T_B$ ).....	33
3.3.4 High cloud cover ( $C_H$ ).....	33
3.3.5 Summary of trends .....	34
3.3.6 Latitudinal movement of three indices of expansion.....	35
3.3.7 Convection characteristics in the tropical zone during DJF .....	36
3.3.8 Regional wind flow .....	44
3.3.9 Relationships with climate indices.....	45
3.4 Discussion .....	46
3.5 Conclusion.....	48
Chapter 4.....	51
An investigation of poleward expansion of the Hadley circulation using high cloud cover .....	51
4.1 Introduction .....	51
4.2 Data .....	52
4.3 Results .....	54
4.4 Conclusion.....	57



Chapter 5 .....	58
Effects of tropical expansion on climate in Thailand .....	58
5.1 Flood and drought .....	58
5.1.1 Flood .....	58
5.1.2 Drought .....	59
5.2 Standardized Precipitation Index (SPI) .....	59
5.3 Calculation of SPI .....	61
5.4 The indices of the expansion .....	65
5.5 Method .....	65
5.6 Results and Discussion .....	65
5.7 Conclusion .....	68
Chapter 6 .....	70
Conclusion .....	70
Appendix 1 .....	71
Mapping solar irradiation from ground- and satellite-based data over Thailand using a simple semi-empirical model .....	71
1 Introduction .....	71
2 Materials and Methods .....	72
2.1 Materials .....	72
2.1.1 Satellite data .....	72
2.1.2 Ground-based data .....	73
2.2 Methods .....	75
2.2.1 Modeling .....	75
2.2.2 Evaluation of model performance .....	79

2.2.3 Mapping.....	80
3 Results and Discussion.....	83
4 Conclusion.....	85
Appendix 2.....	86
List of publications and conferences.....	86
Publications .....	86
Conferences .....	86
REFERENCES .....	92
VITA .....	102



# Chapter 1

## Introduction

### 1.1 Rationale of the study

Amongst the issues associated with global climate change, the expansion of the tropics has become increasingly important in the last decade. The phenomenon was first described in a paper by Fu et al. (2006) who examined Microwave Sounding Unit data from satellite observations to discover a trend towards enhanced tropospheric warming and stratospheric cooling around 15 to 45 degrees in both hemispheres. They related this pattern to a poleward shift of the subtropical jet. Subsequent studies revealed a pronounced poleward shift in global weather systems and climate zones (Birner et al., 2014; Fu & Lin, 2011; Seidel et al., 2007; Seidel & Randel, 2007). An expanded and more intense Hadley cell (HC) also relates to a poleward shift in the subtropical high-pressure regions with negative consequences on ecosystems worldwide (Bonan, 2008; Heffernan, 2016; Issac & Turton, 2014). Despite some available documents on the tropical expansion, there exists considerable uncertainty in the causes, and the spatial/temporal trends associated with this effect (Lucas et al., 2014). Studies by Birner et al. (2014), Davis and Rosenlof (2012) and Lucas et al. (2014) gave a rate of expansion of the HC of between 0 to 2 degrees per decade, while Quan et al. (2014) compared model and reanalysis data to arrive at a figure of around 0.1 to 0.2 degrees per decade. Much of the discrepancy is likely to arise from the different metrics used to measure the expansion rate (Lucas et al., 2014).

Most of the work in the tropical expansion investigation have been carried out over the globe and the regional study is very limited. Long-term studies at decadal time scales are very few in the Southeast Asia and particularly the Thailand. In addition, it is evident that few studies have examined the long-term interannual variability of tropical expansion and how a changing climate environment will affect future floods and droughts. Given the importance of a stable precipitation environment to agriculture in Thailand, it is important to determine how significant tropical expansion will be and

if this process will be associated with changes in floods and droughts events, or conversely, if extreme rainfall events will not be accompanied by tropical expansion. While the above literature discusses large-scale global processes, there is need for intensive regional studies within the GMS to observe what has been the pattern of expansion and how it relates to floods and droughts in Thailand.

Therefore, this work aims to investigate the tropical expansion in the GMS regions and the correlation between the tropical expansion and climate in Thailand.

## **1.2 Objectives**

The specific objectives of this study are as follows.

- 1) To investigate the tropical expansion in the GMS region.
- 2) To study the effect of the tropical expansion on climate in Thailand.

## **1.3 Organization of this thesis**

This thesis consists of 6 chapters. The first chapter is the rationale of the study. The second chapter is the theory and literature review. The third chapter presents the regional study in the Greater Mekong Subregion (GMS) and tropical expansion. The fourth chapter describes an investigation of poleward expansion of the Hadley circulation using high cloud cover over the globe. The fifth chapter presents an investigation of the effects of tropical expansion on climate in Thailand. The final chapter is the conclusion.

## Chapter 2

### Theory and literature review

#### 2.1 Atmospheric circulation

In each hemisphere, there are three-cells of circulation. These are Hadley cell (covering the latitude of 0 - 30°), Ferrel cell (circulating between the latitude of 30 - 60°) and Polar cell (covering the latitude of 60 - 90°). In the tropics, the air is warm and rises, causing cumulus clouds and thunderstorms to drive the Hadley cell. The rising warm air reaches the tropopause, causing the air to move poleward. The Coriolis force deflects the air to move toward the right in the northern hemisphere and toward the left in the southern hemisphere, resulting in the westerly wind in both hemispheres. The air moving poleward cools by giving up infrared radiation and then converged around the middle latitude (30°), causing the air to be relatively dry. Thus, the mass of the air increases and then descends to the surface. This results in clear skies and warm surface temperatures in this region called subtropical highs (Figure 2.1).

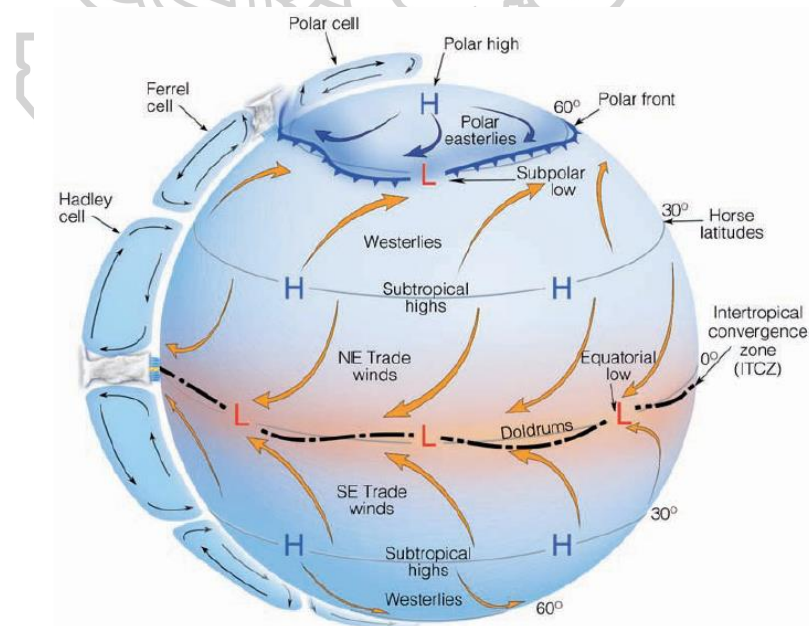


Figure 2.1 Diagram showing the general circulation of the air in the three-cell model.

Some of the surface air moves toward the equator and others move poleward. As there is the cold air blowing from the poles, these two air masses are not mixed well causing a boundary called the polar front around the latitude of  $60^\circ$ . The surface air in this region converges and rises resulting in developing clouds and storms (Figure 2.2). This air then diverges and some return to the subtropical high. This middle cell circulation is called a Ferrel cell. Apart from the air returning to the subtropical highs, some of the air moves to the poles and slowly sink, producing the circulation in this region called the Polar cell.

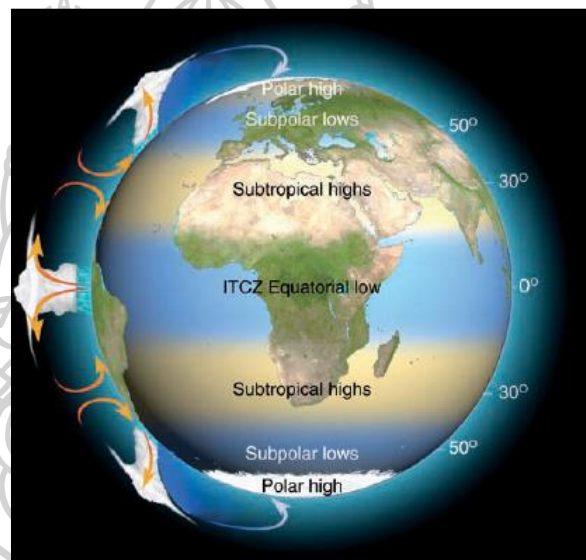


Figure 2.2 Diagram showing the locations of the subtropical high and ITCZ equatorial low

## 2.2 Intertropical convergence zone (ITCZ)

Intertropical convergence zone (ITCZ) or monsoon trough is the region of low pressure in which the trade winds of the northeast and southeast come together near the equator (Figure 2.2) (Ahrens, 1998). In this area, the air is warm, and winds are light referred to as the doldrums, which play critical roles in transporting heat, driving ocean circulation and supplying precipitation due to surface convergence, inducing large-scale monsoonal wind regimes. It can cause generates huge cumulus clouds and

thunderstorms. It is most active over continental landmasses by day and relatively less active over the oceans. The ITCZ is identified on the satellite image as the bands of bright clouds located just near the equator are shown in Figure 2.3.

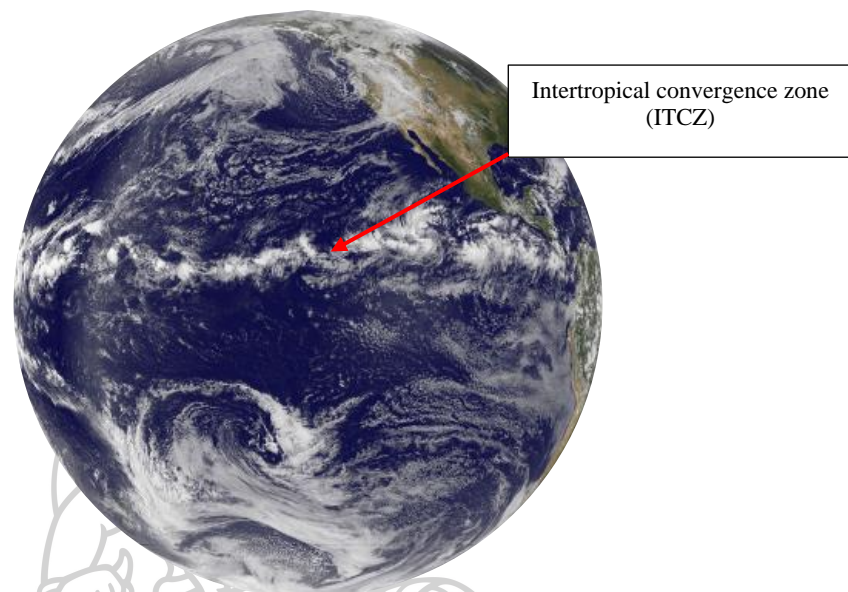


Figure 2.3 The ITCZ showing on the satellite image (NOAA GOES Project Science Office and NASA)

The ITCZ is not a stationary band but tends to migrate seasonally to the warmest surface areas following the annual cycle of surface solar heating. At the beginning of the year, the high solar radiation occurs in the Southern Hemisphere causing a southward displacement of the ITCZ (in January, Figure 2.4). After that, as the sun path moves to the Northern Hemisphere, the ITCZ also moves northward attaining its maximum northward displacement during the month of June and July (Figure 2.5).

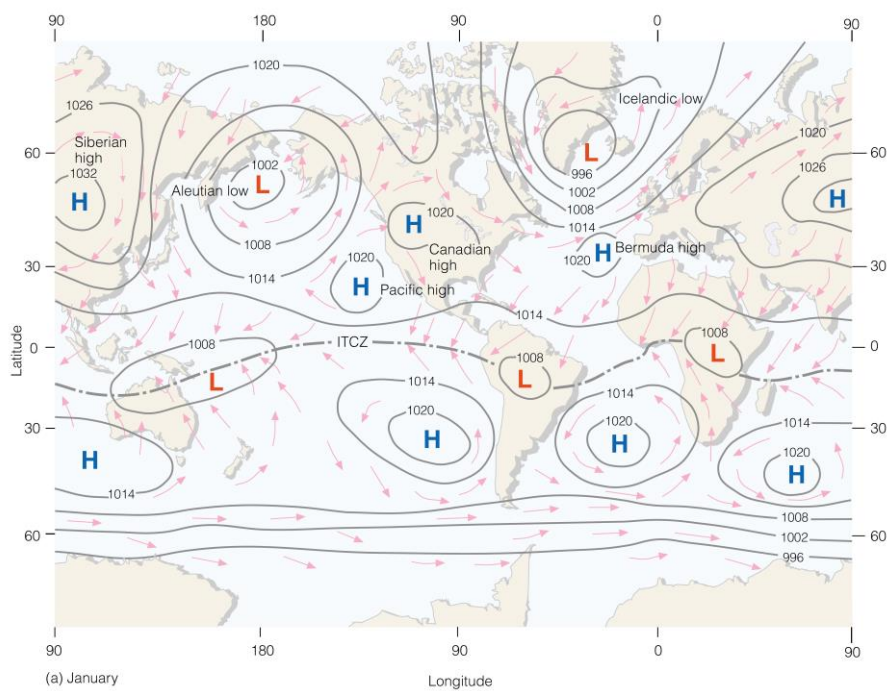


Figure 2.4 The heavy dashed line represents the position of the ITCZ in January (Ahrens, 1998).

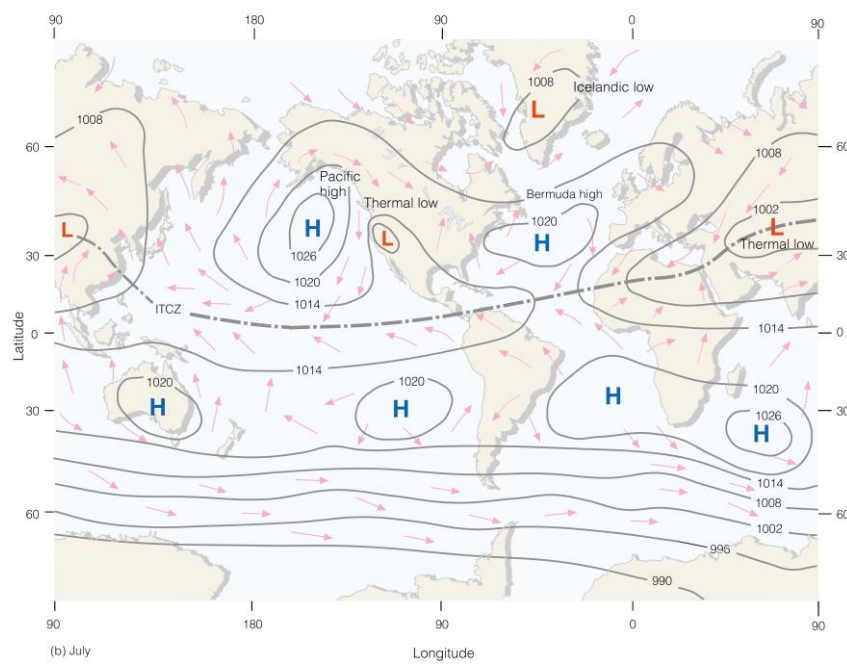


Figure 2.5 The heavy dashed line represents the position of the ITCZ in July (Ahrens, 1998).



As the ITCZ relates the ascending branch of the Hadley cell, the seasonal migration of the ITCZ can contribute to the movement of the Hadley cell.

### 2.3 Greater Mekong Subregion

Greater Mekong Subregion is a trans-national region of the Mekong River basin in Southeast Asia. This region consists of six countries: Cambodia, China (specifically Yunnan Province and Guangxi Zhuang Autonomous Region), Laos, Myanmar, Vietnam, and Thailand, covering 2.6 million square kilometers (Figure 2.6). There are more than 300 million people in the region.

The Greater Mekong Subregion holds irreplaceable natural and cultural riches and is considered to be one of the world's most significant biodiversity hotspots. The region is an important food provider and the site of many large-scale construction projects with important social and economic impacts.

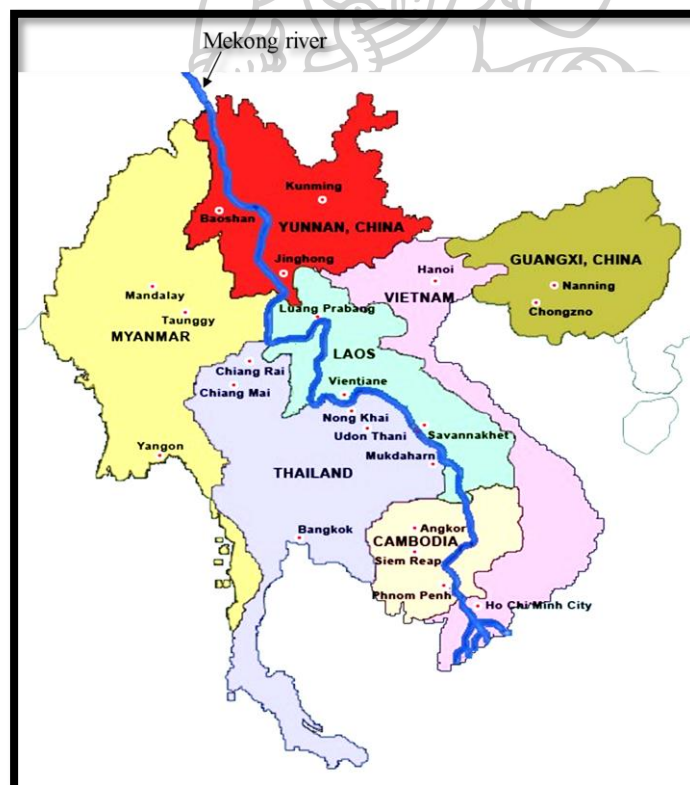


Figure 2.6 Area of the Greater Mekong Subregion.

(<http://investvine.com/focus-on-greater-mekong-subregion-tourism/>)

The Mekong river, one of the most important transboundary rivers in southeast Asia, starts in Tibet, flows from China's Yunnan Province to Vietnam, and finally end at the South China Sea. The entire Mekong River Basin (MRB) is divided into two regions, the Upper Mekong River Basin (UMRB), where the river is also called the Lancang Jiang, and the Lower Mekong River Basin (LMRB), with a boundary at approximately 21°N (Commission, 2005) (Figure 2.7). The geomorphology of the UMRB transforms from high mountains and deep valleys to low/medium mountains and wide valleys in a northwest–southeast orientation. Compared to the UMRB, the LMRB has a flatter land surface, lower elevation, and more precipitation.

The climate of the Mekong River Basin ranges from temperate to tropical. In the Upper Mekong River Basin, some of the taller peaks of the Tibetan Plateau are glaciated. In fact, much of this part of the Mekong River Basin is snow-covered in winter. Melting snow from the Tibetan Plateau feeds the Mekong River's dry-season flow, especially in the middle reaches. In the relatively lower elevations of the Yunnan province of China, the climate of the Mekong River Basin changes and the temperature gradually increases.

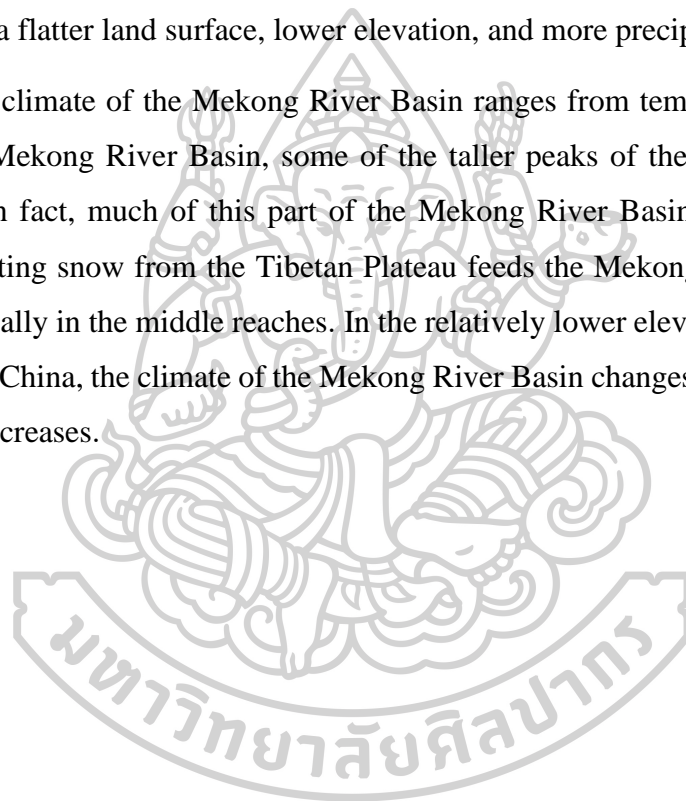




Figure 2.7 Mekong River Basin

June to October is the wet season in the LMRB; with the exception of two brief transition periods (Figure 2.8), the rest of the year in the LMRB is the dry season. The wet season results from the flow of moisture-laden air from the Indian Ocean in the summer. During the rest of the year, high-pressure systems over the Asian continent give rise to the dry season in the LMRB.

Cooler		Hot/Dry			Wet					Cooler	
Jan	Feb	Mar	Apr	May	Jun	Jul	Aug	Sept	Oct	Nov	Dec
NE monsoon		Transition			SW monsoon					NE monsoon	

Figure 2.8 Lower Mekong River Basin seasonal climate (Commission, 2010).

The climate of the LMRB, which is almost always hot and often humid, is classified as tropical monsoonal. In the warmest months of March and April, average temperature ranges from 30°C to 38°C. Cooler temperatures prevail from November to February. At higher elevations in the Lao People’s Democratic Republic (Lao PDR), winter temperature averages 15°C.

The LMRB experiences a typical monsoon climate (Figure 2.9). A monsoon climate is a dry and wet alternation with the wet season lasting from mid-May to October. During the rainy season, the region around the LMRB, which is influenced by the Indian summer monsoon (ISM) and East Asian summer monsoon (EASM), receives over 80% of its annual precipitation.

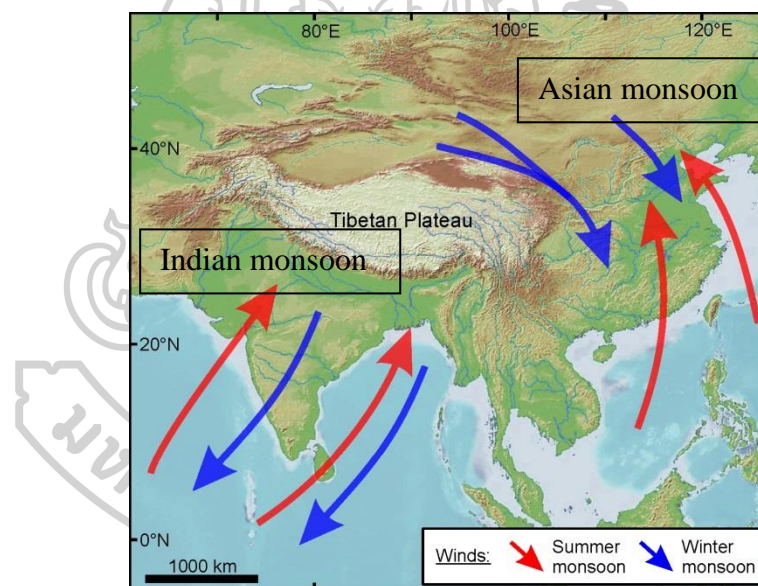


Figure 2.9 Indian monsoon and Asian monsoon

The distribution of mean annual rainfall over the basin follows a distinct east-to-west gradient. In the LMRB, the rain-soaked uplands in the Lao PDR and Cambodia receive the most precipitation (3,000 mm) and the semi-arid Khorat Plateau in northeast Thailand the least (1,000 to 1,600 mm). The UMRB is similar to the LMRB in that rainfall is regulated by the global monsoon system. In the Upper Basin, annual rainfall can be as little as 600 mm in the Tibetan Plateau and as much as 1,700 mm in the mountains of Yunnan.

Countries in the LMRB are among the most vulnerable locations in the world with respect to climate change. While the future impact of climate change is difficult to forecast, projections for the Mekong River Basin for the next 20 to 30 years, based on a global climate model, are as follows (Hoanh et al., 2003). Basin-wide temperature increase of 0.79°C, with greater increases in colder catchment areas in the north. Annual precipitation increase of 200 mm (a 13.5% rise). Increase in dry-season precipitation in northern catchments and decrease in southern catchments. Total annual runoff increase of 21%. Increase in flooding in all parts of the basin with the greatest impact on downstream catchments of the Mekong River.

Climate change is expected to affect natural ecosystems and agriculture throughout the Mekong River Basin, thereby exacerbating the challenges of meeting the increasing demand for resources from growing populations.

#### **2.4 Literature reviews**

As the Hadley circulation have influences on regional and global climate, there are a number of studies examining the concept of tropical expansion considering the change of the Hadley cell (Allen & Ajoku, 2016; Hu et al., 2018; Johanson & Fu, 2009; Lau & Kim, 2015; Lu et al., 2007; Quan et al., 2014; Seidel & Randel, 2007; Staten et al., 2018; Waugh et al., 2018). As shown in the work of Staten et al. (2018), they reviewed the studies which document a poleward shift in weather systems using a variety of methods and metrics. The rates of the expansion were found differently as they used different datasets. Diagnostic models are commonly used to examine Hadley cell expansion (Hu & Fu, 2007; Lau & Kim, 2015; Lu et al., 2007), widening of the tropical belt (Davis & Rosenlof, 2012; Seidel et al., 2008; Seidel & Randel, 2007; You et al., 2015) and subtropical and tropospheric jet position (Fu & Lin, 2011; Manney et al., 2017). The shift is believed to result from tropospheric warming from greenhouse gases, stratospheric ozone depletion in the Southern Hemisphere and anthropogenic/natural aerosols. Following studies are examples of the work.

Hudson et al. (2006) present an investigation of total ozone variability from the TOMS instruments. The trend of the zonal mean of total ozone concentration occupied the tropical area in the Northern Hemisphere had expanded at a rate of 1° latitude per

decade or approximately  $2.5^\circ$  latitude over the period 1979-2003. And then in the same time period, Fu et al. (2006) employed satellite temperature observations from 1979-2005 and guessed at the tropic a widening approximately  $2^\circ$  latitude across both hemispheres.

In the year after, there have been a publication of Hu and Fu (2007) showing that the Hadley circulation has a significant widening of about 2 to  $4.5^\circ$  in latitude from three meteorological reanalysis and outgoing long-wave radiation (OLR) datasets. The widening of the Hadley circulation implies a poleward expansion of the tropical dry zone.

Over the same year, a study by Seidel and Randel (2007) used long-term tropopause height to examine expansion of tropical belt. The data over the period 1979-2005 indicate that the tropical expansion of about  $5^\circ$ - $8^\circ$  latitude.

Lu et al. (2007) investigated the influence of the Hadley cell on global warming using the 21<sup>st</sup> century increasing greenhouse gas scenarios from the Fourth Assessment Report (AR4) of the Intergovernmental Panel on Climate Change (IPCC). The data used in this study were monthly precipitation, evaporation, surface air temperature, surface wind, temperature, meridional wind speed and 500 hPa vertical wind velocity. The zonal mean mass flux stream function was calculated from the vertical meridional wind to indicate the edges of the Hadley cell. Also the edge of the subtropical dry zone was indicated by using the difference between the zonal mean precipitation and evaporation. The results show that the poleward shift is about  $1^\circ$  in each hemisphere.

Seidel et al. (2008) noted that the tropical expansion could result in shifts in rainfall pattern and this will influence on ecosystems, agricultural and water resources. They also summarized pictures of the changes in the tropical width based on several parameters such as ozone depletion, outgoing longwave radiation and tropopause height (Figure 2.10). The results show the rate of the expansion between  $2.0 - 4.8^\circ$  latitude per 25 years.

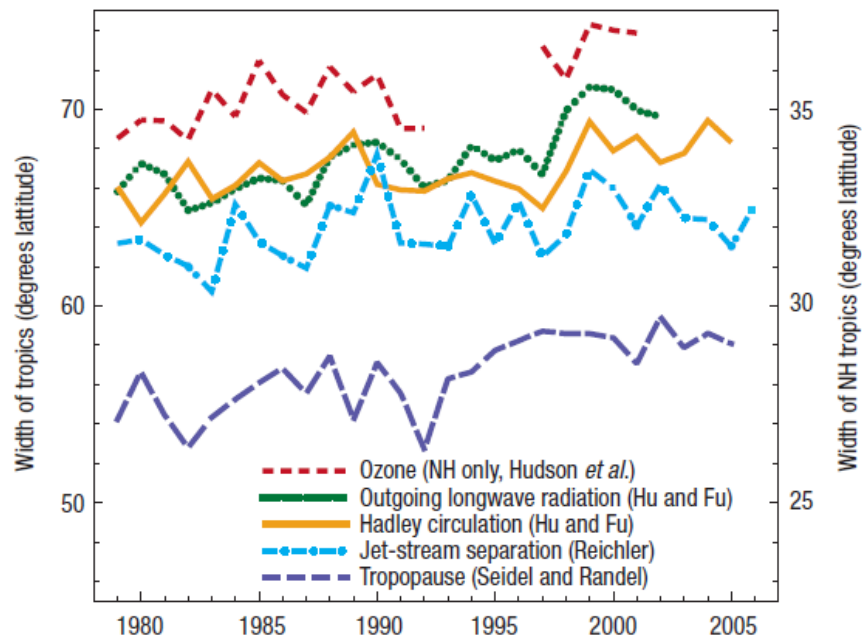


Figure 2.10 Changes of the width of the tropical belt since 1979, based on outgoing longwave radiation, horizontal wind stream function, tropopause level and column ozone level (Seidel et al., 2008).

Johanson and Fu (2009) compared the results of the tropical expansion from the various datasets. They used outgoing longwave radiation from three sources that are the datasets from the High Resolution Infrared Radiation Sounder (HIRS) pathfinder dataset, the International Satellite Cloud Climatology Project (ISCCP) dataset and the Global Energy and Water Cycle Experiment (GEWEX) Radiative Flux Assessment (RFA) dataset. The data periods used in this work are from 1979 - 2002 for HIRS and from 1983 - 2004 for the ISCCP and GEWEX. The reanalysis data was also used, which are from the 40-year European Centre for Medium-Range Weather Forecasts Reanalysis (ERA-40), the National Centers for Environmental Prediction-National Center for Atmospheric Research (NCEP-NCAR) and the National Centers for Environmental Prediction-Department of Energy (NCEP-DOE). The data of ERA-40 during 1979 - 2001 and the data of NCEP-NCAR and NCEP-DOE during 1979 - 2005 were used. The observation results were compared with those from global climate model (GCM). The results present that the widening in GCM models ( $1.5^{\circ}$ ) which include greenhouse gas

forcing and stratospheric ozone depletion is smaller than that from the observations (about  $3^\circ$ ) in the last 25 years.

Quan et al. (2014) attempted to investigate the rate of boreal winter expansion and to explore physical mechanisms. In this work, the zonal mean precipitation, evaporation and zonal mean meridional stream function were used as indicators of the tropical expansion. From the results, the expansion rate was up to  $1^\circ$  latitude per decade. The expansion has been greater in the southern hemisphere than in the northern hemisphere. This may result from Antarctic stratospheric ozone depletion. By using climate model, they found that the tropical widening caused by the warming oceans.

You et al. (2015) used upper tropospheric water vapour (UTWV) brightness temperatures during 1979-2013 from intersatellite-calibrated high-resolution infrared radiation sounder (HIRS) to define the width of the tropical belt. The width can be calculated from the latitude at which maximum brightness temperature are recorded in both hemispheres. In this work, they focused in different regional areas: East Pacific, West pacific, Atlantic, Indian, Africa, South America and Globe. From this study, the poleward expansion is occurred in the west pacific at about  $1.57^\circ$  per decade.

Grise and Polvani (2014) used three metrics to define the Hadley circulation edge that are latitude of the maximum zonal mean of wind field at 850 hPa, latitude where precipitation minus evaporation is equal to zero, and latitude where the 500 hPa mean mass stream function is zero. The edges of the Hadley cell were showed as  $43^\circ\text{N}$ ,  $40^\circ\text{N}$  and  $33^\circ\text{N}$  using the three metrics, respectively. This work also found that the expansion of the Hadley cell occurs during winter but contraction occurs during summer. This may result from the weak summer branch of the Hadley cell.

Lucas and Nguyen (2015) characterized the tropical expansion over three regions in the northern hemisphere including North America, Europe and Asia, using the radiosonde data from IGRA. They also compared the result with that in the southern hemisphere and found that the largest expansion rate occurred over Asia and Australia and New Zealand. Furthermore, the expansion rate showed no significant over North America. The southern hemisphere showed slightly larger expansion rate than the northern hemisphere.



Tselioudis et al. (2016) investigated the relationship between high cloud cover and two indices of the atmospheric circulation (the latitudinal positions of the Hadley cell edge and the midlatitude jet) in three regions: North Atlantic (280°E-360°E), North Pacific (120°E-240°E) and entire Southern Ocean. They used the center of mass of the zonal mean westerlies around 850 hPa maximum and poleward of 20° latitude from ERA-Interim to indicate the mid latitude jet, and mean meridional mass stream function at 500 hPa and also precipitation minus evaporation to indicate the latitude of the Hadley cell edge. From the results, there are poleward shift of high clouds and Hadley cell edge (0.3-0.5° per decade) for all seasons for the Southern Ocean but only for summer season for the Northern hemisphere regions.

Hu et al. (2018) reviewed the studies in trends of width and strength of the Hadley circulation. They showed the seasonal variation of the Hadley circulation in both hemispheres by using reanalysis data. The widening trends in summer and autumn seasons are larger than that in winter and spring seasons. These variations seem to be associated radiative forcing from black carbon, tropospheric and stratospheric ozone and greenhouse gases. They also concluded that the widening trends derived from simulation (CMIP5) are much higher than from reanalysis data. For the strengthening, Hadley circulation is generally stronger/narrower for El Niño and weaker/wider for La Niña.

Staten et al. (2018) reviewed studies on tropical expansion which can impact both land and sea. They reviewed that there are many metrics to indicate the tropical expansion including stream function at 500 hPa, surface wind, sea level pressure, precipitation minus evaporation, outgoing longwave radiation. Apart from these metrics, there are some upper tropospheric indices such as column ozone, subtropical jet stream and tropical tropopause height. However, these metrics have several drawbacks. They show a wide range of expansion rates and a weak correlation from year to year. Therefore, in this work, they focused on the tropospheric metrics; stream function, wind speed and precipitation minus evaporation. They concluded that the causes of the expansion can be increasing GHG, depletion of stratospheric ozone, volcanic forcing, increasing pollutions and changing SST.

There are also researches attempted to understand the mechanism of the Hadley circulation moving poleward and its impact. In the study of Seager et al. (2010), they concluded that P-E change with wet areas getting wetter and dry areas getting drier and with poleward expansion of the subtropical dry zone. Lau and Kim (2015) investigated changes in Hadley circulation and their relationship between the increasing of global dryness and CO<sub>2</sub> warming using climate models called CMIP5. The results showed that the Hadley circulation has been strengthening or there has been deepening and narrowing of the convection zone. They also noted that as global temperature rises, increased dryness is found in many regions around the world. Thus, to investigate relation between the strengthen of the Hadley circulation and global dryness, they calculated global dryness index (GDI) to indicate the extreme dry month where the monthly rainfall is less than 0.1 mm/day at any grid point and use EOF analysis to investigate the GDI.

Allen and Kovilakam (2017) showed that the tropical expansion has been related to ENSO/PDO as the Hadley circulation decreases during the warm phase of ENSO/PDO and increases during the cold phase. This is also mentioned in the work of Grise et al. (2019) who found that tropics expand during La Nina and contract during El Nino.

Schmidt and Grise (2017) used monthly mean meridional wind to estimate the Hadley circulation and it impacts on the sea level pressure from ERA-interim data and precipitation from GPCP/CMAP during 1979-2015. They did the regression of sea level pressure and the precipitation onto the monthly time series of Hadley circulation edge. Note that they have removed the trends and seasonal cycles from all fields prior to the regression analysis. The regression results of precipitation are much noisier than the sea level pressure which may results from thermodynamics factors.

Recently, Xia et al. (2020) concluded that the tropical expansion in Northern hemisphere is mainly forced by greenhouse gases and is little impacted by stratospheric

ozone and anthropogenic aerosols. While in Southern hemisphere, greenhouse gases and stratospheric are the main forced.

From the literature review, it is noticed that most study were focused on the investigation of the tropical expansion in the global scale and the investigation of the expansion in the regional scale is very limited. Therefor this present study concentrates in the investigation of the expansion in the GMS region. The details of the study are presented in the next chapters.



## Chapter 3

### **The Greater Mekong Subregion (GMS) and Tropical Expansion: A Regional Study of Convection and Precipitation<sup>1</sup>**

This chapter presents high cloud cover, brightness temperature and precipitation minus evaporation as the tropical expansion indices. The area of the study is focused on the GMS. The relation of the expansion and climate indices are also discussed. The details of this study are as follows.

#### **3.1. Introduction**

This study aims at examining recent precipitation and convection trends in the Greater Mekong Subregion (GMS) within the context of tropical expansion. The catchment area of the Mekong River (Figure 3.1) is approximately 2.6 million km<sup>2</sup> and includes Cambodia, Vietnam, Laos, Myanmar, Thailand, and the Yunnan and Guangxi provinces of southern China. It provides for 320 million people, 70% of whom rely on agricultural and water-related activities for their livelihood. These may be at risk from climate change and/or water degradation (Commission, 2018; Hirsch et al., 2008; Oldeman & Frere, 1982).

The above activities rely on consistent and predictable rain-bearing systems from the southwest (SW) monsoon. From May to October, they sweep across the region, originating in India (Climatological Group, 2015; Janjai et al., 2015). The Intertropical Convergence Zone (ITCZ) moves northward in tandem with the SW movement, setting in southern China around June to July, then moving southward toward northern Thailand in August and southern Thailand in September/October. The East Asian monsoon brings cool dry air from China throughout the winter months, which extend from mid-October to mid-February, though southern Thailand

---

<sup>1</sup> This chapter has been published in the Journal of Advances in Space Research 69 (2022) 2443–2459.

experiences mild weather and rainy periods. The northern area of the GMS is influenced by both southwest and East Asian monsoons.

It is necessary to examine how resilient the GMS monsoon system is in the context of tropical expansion, which is an important feature of global warming. Tropical expansion is a poleward displacement of the “edge of the tropics” and it is commonly associated with the downward branch of the Hadley circulation (Lucas et al., 2014; Reichler, 2009; Seidel & Randel, 2007). This is a global feature, which is related to changing precipitation and drought patterns. A variety of methods and metrics are used in studies that document a poleward shift in weather systems (Grise et al., 2019). Diagnostic models are commonly used to examine Hadley cell expansion (Hu & Fu, 2007; Hu et al., 2011; Lu et al., 2007), tropical belt widening (Davis & Rosenlof, 2012; Seidel et al., 2008; Seidel & Randel, 2007; You et al., 2015), and subtropical and tropospheric jet position (Fu & Lin, 2011; Manney & Hegglin, 2018). The estimated rates for the northern hemisphere range from near zero to  $0.3^\circ$  per decade using a variety of methods (Staten et al., 2018).

Anthropogenic/natural aerosols, greenhouse gases, and stratospheric ozone are believed to be important agents in the northern hemisphere expansion process (Allen & Ajoku, 2016; Lau & Kim, 2015; Staten et al., 2018; Waugh et al., 2018). In studies of convection and precipitation in the Indian subcontinent and Southeast Asia, aerosols are frequently mentioned. Sulfate-based aerosols will cool the earth’s surface by increasing the scattering of radiation to space, leading to a decrease in precipitation (Cowan & Cai, 2011; Kim et al., 2007). Anthropogenic aerosols, which are mostly carbon-based, produce more equivocal results. The so-called elevated heat pump effect has been documented in several studies as a convection enhancement at the ITCZ as a result of increased absorption by black carbon (BC) aerosols, leading to increased precipitation and a narrowing of the tropical belt (Byrne & Schneider, 2016; Kovilakam & Mahajan, 2016; Lau et al., 2006; Lau & Kim, 2015; Zhou et al., 2019). In contrast, Meehl et al. (2008) discovered that adding BC into their model enhanced precipitation and convection in the pre-monsoon months (March to May), but the values obtained during the actual monsoon (June to August) were relatively low. Cowan and Cai (2011)

and Ganguly et al. (2012) also reported that aerosols, both natural and anthropogenic, reduce monsoon convection and precipitation.

This study concentrates on observational convection and precipitation records in the GMS to determine their long-term changes and their potential response to the forcing agents discussed in the above literature. During boreal winter, potential changes include not only convection and precipitation but also the position of the Hadley cell edge, which is characterized by maximum subsidence. The position of maximum convection and its long-term changes are of relevance during the boreal summer, which is dominated by the SW monsoon.

Many studies focus on the Indian monsoon system, which has little impact on the GMS in some cases. For example, GMS precipitation/convection may be sensitive to a north-westward shift in the east Asia rain belt as a result of an anomalous low over Tibet, as indicated by Lau et al. (2006). Convection records are essential since they cause precipitation in the tropics and are linked to many of the above mentioned modeling/sensitivity studies.

The majority of tropical expansion studies are conducted on a global scale, with little work done at the regional level. This study examines tropical expansion effects on climate change in the GMS region. It is important to examine possible changes in hydrology, as well as their relationship to other climate variables and possible causes of the expansion. To accomplish this task, a collection of data sets has been obtained for processing and analysis.

We used brightness temperature (TB) from a high-resolution infrared radiation sounder measuring upper tropospheric water vapor (HIRS-UTWV) as a convection index (Shi et al., 2013). Deep convective cloud (CV) data have been acquired from the International Satellite Cloud Climatology Project (ISCCP) (Schiffer & Rossow, 1983). Monthly precipitation (P), evaporation (E), and high cloud cover (CH) data from ERA-Interim reanalysis were used (Berrisford et al., 2011).

This chapter is arranged as follows: Section 3.2 provides more details on used data sets and methods, Section 3.3 provides the main results, Section 3.4 discusses the

results within a wider tropical expansion context, and Section 3.5 presents the conclusions.

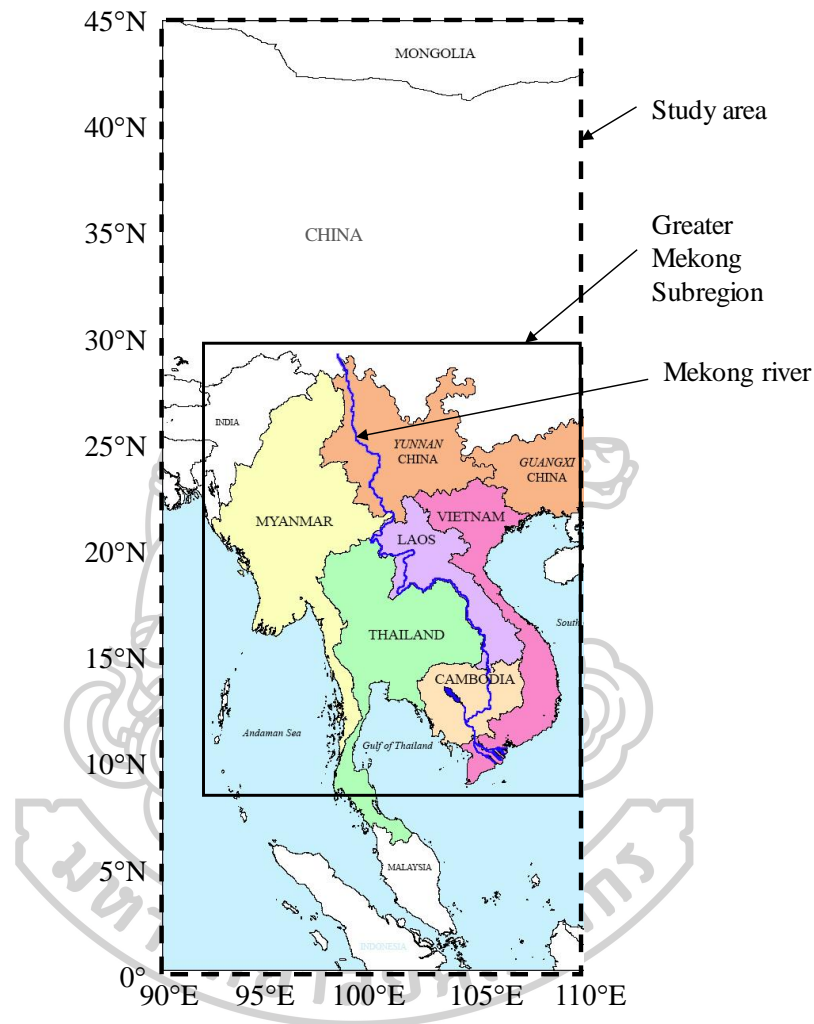


Figure 3.1 Area of the Greater Mekong Sub-region. This analysis covered a rectangular area bounded by 0°N-45°N; 90°E-110°E and encompassing this region.

### 3.2 Data and methodology

The area of the GMS is covered by this study, which encompasses latitudes of 0°N to 45°N and longitudes of 90°E to 110°E (Figure 3.1). Table 3.1 presents the data acquired for the region.

Table 3.1 Data sets used for this study.

Data	Spatial resolutions	Temporal resolution	Time period
T <sub>B</sub> from HIRS-UTWV	2.5° × 2.5°	monthly	1979–2017
P from ERA-Interim	1.0° × 1.0°	monthly	1979–2018
E from ERA-Interim	1.0° × 1.0°	monthly	1979–2018
C <sub>H</sub> from ERA-Interim	1.0° × 1.0°	monthly	1979–2018
C <sub>V</sub> from ISCCP	1.0° × 1.0°	monthly	1983–2016
P from TRMM	0.25° × 0.25°	monthly	1998–2015
U wind from ERA-Interim	1.0° × 1.0°	monthly	1983–2017
U wind from MERRA	0.5° × 0.625°	monthly	1983–2017

P = monthly precipitation (mm per month)

E = monthly evaporation (mm per month)

C<sub>H</sub> = fraction of the sky covered by high clouds (-)

C<sub>V</sub> = deep convective cloud (%)

U = eastward wind speed (m/s)

### 3.2.1 Data

#### 3.2.1.1 HIRS-UTWV

The high-resolution infrared radiation sounder is a 20-channel instrument that has been carried onboard various NOAA polar-orbiting satellites for decades. Channel 12, with a central response function of 6.5 μm has been used to detect water vapor (Shi et al., 2013). Data from the various satellites were compared and calibrated to provide a homogeneous and continuous data set suitable for climate analysis (Bates et al., 1996; Shi & Bates, 2011). The current version of the data set includes a correction that uses brightness temperature from the window channel at 11 μm to reduce the influence from upper tropospheric clouds (Nguyen et al., 2013). This feature eliminates the need to remove cloud-contaminated pixels, which causes data gaps and biases records toward low tropospheric humidity (Lanzante & Gahrs, 2000; Soden & Lanzante, 1996). The



data are consistent with the 183.31 GHz microwave sounder channel, which is also used for water vapor. It also has a good correlation with climate indices, such as the Pacific Decadal Oscillation (PDO) and the El Niño 3.4 index (Shi & Bates, 2011). In terms of detecting the descending branch of the Hadley cell, HIRS data are preferred over cloud observations since they can detect column moisture differences in cloudless pixels (Shi et al., 2013; You et al., 2015).

From 1979 to 2017, monthly average  $T_B$  for the entire globe was downloaded from [www.ncei.noaa.gov](http://www.ncei.noaa.gov). The data were provided as an average of a  $2.5^\circ\text{N} \times 2.5^\circ\text{E}$  pixel that covers the entire globe. Afterward, they were sectorized for this study region, which includes the GMS. The data were reduced to 19 pixels (N/S)  $\times$  39 pixels (E/W) for each month for a total of 468 months after sectorization (1979–2017).

#### 3.2.1.2 ISCCP

To further examine convection processes in the study area, the authors used  $C_V$  data from ISCCP (<https://www.ncdc.noaa.gov/isccp>). Several studies have documented the role of deep convective cloud in bringing heavy precipitation, particularly in the tropics (Albright et al., 1985; Casella et al., 2012; Worku et al., 2019). Many international programs and studies have validated the ISCCP data set (Hahn et al., 2001; Halladay et al., 2012; Schiffer & Rossow, 1983).

The HGH/HGM Basic variable data set comprises a series of global cloud products with a resolution of  $1.0^\circ\text{N} \times 1.0^\circ\text{E}$ . The data set includes information from deep convective ice clouds, which were chosen for this study. Cloud top pressures of 10–440 mb, cloud optical depths of 22.63 to 450, and cloud top temperatures of less than 253 K are all met. Raw data are provided at 3 h intervals, subsequently averaged over a day, and further averaged over a month. Monthly data for this study region were acquired and converted to zonal averages from 1983 to 2016.

#### 3.2.1.3 ERA-Interim

The ERA-Interim reanalysis data are widely recognized and used in a range of climate and trend analysis studies (Bengtsson et al., 2004; Dee et al., 2011; Rienecker

et al., 2008; Simmons, 2006). The most recent version of this data uses a 4D variable assimilation to minimize errors and provide a better representation of stratospheric circulation (Berrisford et al., 2011). A more realistic formulation of ice sedimentation, cloud entrainment, and subsidence, as well as the inclusion of a moist boundary layer, has been included in the hydrologic cycle. These changes are expected to result in more realistic low-level cloud amounts (cumulus and stratocumulus) and boundary layer convection (Dee et al., 2011).

The authors have downloaded  $C_H$ , P, and E from forecast files at <https://www.ecmwf.int/en/forecasts/datasets/reanalysis-datasets/era-interim>. These files provide P and E data at 0:00 and 12:00 UTC daily. The data also provides a cumulative precipitation forecast for the 3, 6, 9, and 12 h at each of these two-time steps. To obtain a daily total P and E, we selected the accumulated forecast at 0:00 UTC + 12 h and 12:00 UTC + 12 h. We combined these forecasts to obtain a daily total, which we then converted into a monthly total P and E. The monthly data for  $C_H$  is provided.  $C_H$  from ERA-Interim were selected to detect ITCZ features. All ERA-Interim data were selected at a resolution of  $1.0^\circ\text{N} \times 1.0^\circ\text{E}$ . According to studies, all ERA-Interim data performed satisfactorily when compared to observational data (Free et al., 2016; Staten et al., 2018).

The quantity of P–E has been used widely in tropical expansion studies (Solomon et al., 2016; Staten et al., 2018; Waugh et al., 2018). Temporal changes in the latitude, where P–E first goes to zero in a poleward direction, have been found to correlate well with other expansion metrics (Waugh et al., 2018).

In addition to the above data, the authors used the ERA-Interim data set (<https://apps.ecmwf.int/datasets/data/interim-full-mode/levtype=pl/>) and MERRA V5.2.0 (<https://giovanni.gsfc.nasa.gov/giovanni>) to provide monthly eastward U wind speeds at 850 mb for the study region. ERA-Interim and MERRA V5.2.0 data are available at resolutions of  $1.0^\circ\text{N} \times 1.0^\circ\text{E}$  and  $0.5^\circ\text{N} \times 0.625^\circ\text{E}$ , respectively. Both data sets were used to examine yearly regional winds for the study area.

### 3.2.2 Methodology

#### 3.2.2.1 Comparison of the ERA-Interim and TRMM precipitation data

The study also aimed at testing the degree of agreement between ERA-Interim precipitation data and an independent data set. In some parts of this study area, rain gauge data is insufficient, making comprehensive validation difficult. The satellite-derived Tropical Mapping Mission (TRMM) data, which were downloaded from [https://disc2.gesdisc.eosdis.nasa.gov/opensdap/TRMM\\_L3/TRMM\\_3B43.7/](https://disc2.gesdisc.eosdis.nasa.gov/.opendap/TRMM_L3/TRMM_3B43.7/), provided a suitable alternative. The TRMM satellite containing both multispectral passive sensors, as well as an active radar sensor (Z. Liu et al., 2012), has been widely tested against other data sets, including rain gauges and rainfall radar (Adeyewa & Nakamura, 2003; Prasetia et al., 2013; Wolff et al., 2005). This version (7\_3B43) is updated monthly and has a spatial resolution of  $0.25^{\circ}\text{N} \times 0.25^{\circ}\text{E}$ .

TRMM data were only available from 1998 to 2015, which is only a portion of the period considered by this study. Therefore, we averaged all TRMM data over time, then over longitudes in this study area at  $1^{\circ}$  latitude intervals. We compared the results with concurrent ERA-Interim data from this study (Figure 3.2). The overall coefficient of determination for the study was 0.92, with a root mean square error of 287 mm per year. Therefore, we conclude that the two data sets adequately capture the trend in precipitation as a function of latitude.

Although zonal average precipitation from ERA-Interim with the spatial resolution of  $1.0^{\circ}\text{N} \times 1.0^{\circ}\text{E}$  correlated well with zonal average precipitation from TRMM in the study area, the application of precipitation from ERA-Interim with different spatial resolutions must be tested again. This could be a limitation of using the ERA-Interim precipitation data.

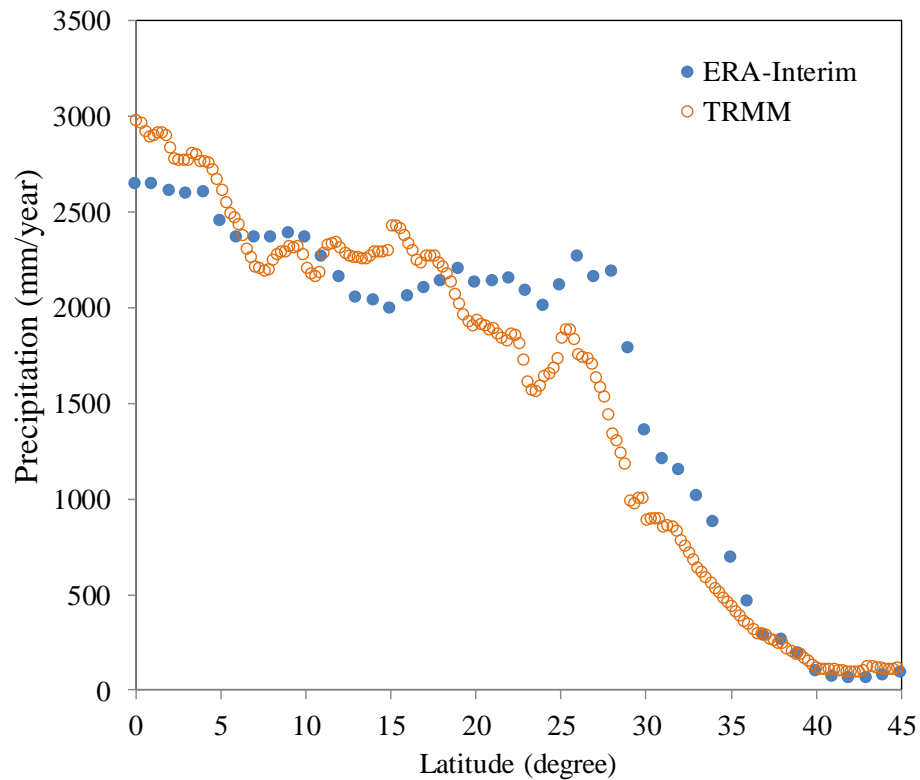


Figure 3.2 Comparison of zonal averages precipitation from ERA-Interim and TRMM during the period of 1998-2015.

#### 3.2.2.2 Data processing and display

To observe trends and shifts in latitude over time, we used zonal means of each parameter in this study area. This procedure enabled the authors to observe latitudinal variations. Using zonal means for each parameter also made it easy to compare this study with other global expansion works, which also employed latitudinal changes. Additionally, averaging over longitudinal bands can potentially minimize localized errors in the data. The study estimates trends as a function of latitude for all 12 months. In addition, latitudinal shifts during the summer monsoon (June to August, JJA) and winter monsoon (December to February, DJF) periods were estimated.

### 3.2.2.3 Metrics used for expansion indices

The metrics that we used for regional expansion are based on Hadley cells characteristics for this region. These are linked to the hydrology of the region, and they do not involve dynamical wind-related atmospheric processes. Davis and Birner (2017) and Waugh et al. (2018) argue that Hadley cell characteristics, such as Hadley cell edge latitude, maximum downwelling, and zonal wind movement, all correspond well in models and reanalyses. In contrast, the latitude of the subtropical jet and tropopause breaks correspond weakly.

In this study,  $T_B$  from the satellite data,  $P-E$ , and  $C_H$  from ERA-Interim were used as metrics to investigate tropical expansion over the GMS area. We zonally averaged these parameters.

Table 3.2 shows the indices of the tropical expansion used in this analysis. DJF and JJA are the two seasons on the table. Each row includes a symbol, its description, and the processes detected. For every year, the zonal  $T_B$  averages for DJF will provide a column of values ranging from 0 to 45°N (Figure 3.3A). In each column, a  $T_B$  maximum is visible, indicating that it corresponds to the dry zones of the subtropical high-pressure regions (Soden & Bretherton, 1993) and regions associated with the descending branch of the Hadley cells (You et al., 2015). The latitude of these maxima was determined by the analysis. However, during JJA, no such maxima were evident, and the study selected latitudes where  $T_B$  was just below 242 K as an index of strong cloud convection during this season. Although the threshold may appear arbitrary, data analysis showed that 242 K frequently represents a boundary between temperatures close to the equator with little change and rapidly increasing temperatures at relatively high latitudes.

In this study, usage of the  $P-E$  index is based on the literature, but with some modification to account for the local characteristics of our monsoon-prone region. (Solomon et al., 2016) defined the index as the latitude at which  $P-E$  crosses the zero boundaries as it moves poleward from the  $P-E$  minimum. Davis and Birner (2017) defined the dry subtropics as the zone where  $P-E < 0$ . During DJF and JJA, we selected the latitude where  $P-E$  initially crosses the zero axis in a poleward direction. Following

the P–E minimum addressed in this measurement (Fig. 3.3B), the study also recorded the second crossing in DJF.

Table 3.2 Indices of expansion that were used.

Index	DJF	Process detected
$T_B$	Latitude of maximum $T_B$	Minimum cloud cover corresponding to zone of maximum downwelling.
P-E	Latitude when P-E first crosses 0 polewards	Zone marked by boundary of wet tropical region.
P-E	Latitude of second zero crossing of P-E crosses 0 polewards	Zone marking the boundary where mid-latitude systems start being noticeable.
$C_H$	Latitude where $C_H = 50\%$ near the equator.	An index of expansion for strong convective clouds near the equator.
Index	JJA	Process detected
$T_B$	Latitude of $T_B$ just under 242 K	An index of expansion for strong convective clouds near the equator.
P-E	Latitude when P-E first crosses 0 polewards.	Zone marked by boundary of wet tropical region.
$C_H$	Latitude of maximum $C_H$	An index of expansion for strong convective clouds near the equator.

P-E = monthly precipitation – monthly evaporation (mm per month)

$C_H$  = fraction of the sky covered by high clouds (-)

$T_B$  = brightness temperature (K)

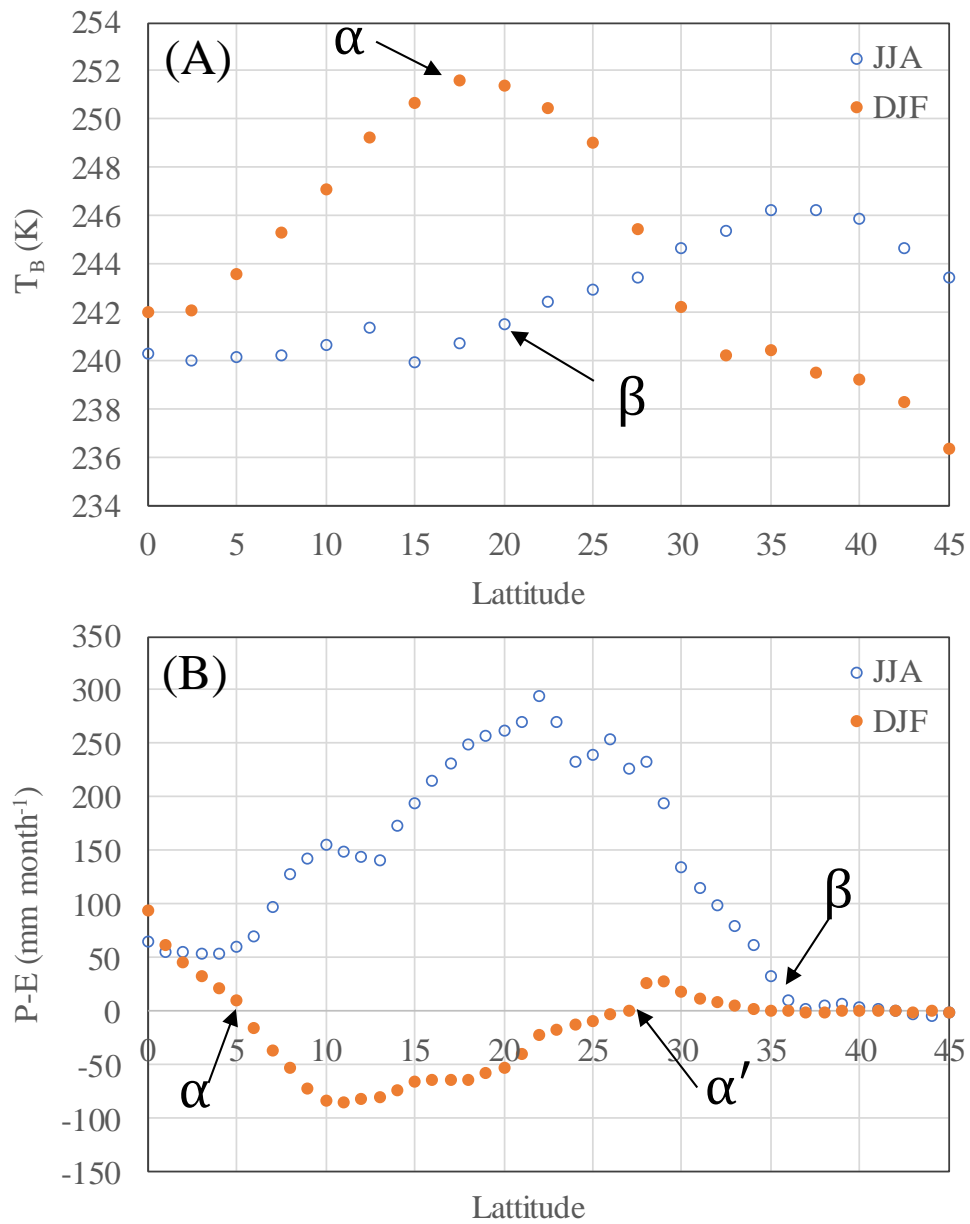


Fig. 3.3 (A) Index of expansion for  $T_B$ ,  $\alpha$  is the latitude of maximum  $T_B$  (DJF) and  $\beta$  is the latitude where  $T_B$  is just under 242 K. (B) Index of expansion for P-E,  $\alpha$  is the latitude where P-E first crosses to zero going poleward (DJF),  $\alpha'$  is the latitude where P-E second crosses to zero going poleward (DJF) and  $\beta$  is the latitude where P-E first crosses to zero (JJA). All data are long-term latitudinal averages for the entire study period (1979-2018).

The last index,  $C_H$ , for the winter (DJF) and summer (JJA) months differs. For the winter (DJF), we selected the latitude where 50%  $C_H$  coverage was reached. This value correlated with the  $C_H$  maximum, which is usually located at the equator. In summer (JJA), we selected the latitude of the maximum  $C_H$  since it correlated with the SW monsoon intensity.

Selection of the relevant latitude for any index and any year is done as follows. The study scanned data, starting at the equator and recording the first latitude before the change in sign or before the threshold. We repeated the process for all years. Afterward, a linear regression between threshold latitude and the year was developed. Regression statistics were obtained using the Theil-Sen robust linear regression approach (Granato, 2006; Helsel & Hirsch, 2002). The technique reduces outlier effects by estimating slope and intercepts based on median statistics. Part of the analysis involves estimating the regression slope and Kendall's Tau correlation at the 95% confidence level.

### 3.3 Results

#### 3.3.1 Precipitation (P)

Figure 3.4A shows the seasonal climatology of precipitation in mm per month averaged throughout the longitude range  $90^\circ\text{E}$ – $110^\circ\text{E}$ . Each month consists of a 46-element vector of  $1^\circ$  latitude and 40-year averages of monthly precipitation (1979–2018). The study clearly shows the seasonal SW monsoon effect, with a maximum isoline of 250 mm per month reaching as far as  $29^\circ\text{N}$ . This isoline shows a very similar pattern to the 245 K  $T_B$  isoline in July/August (Figure 3.4G). During the winter months of January/February, 50 mm per month or less ranging from latitudes  $10^\circ\text{N}$  to  $28^\circ\text{N}$  was recorded. Monthly precipitation at the southern end of the study area ( $0^\circ$ – $5^\circ\text{N}$ ) ranges from 150 mm to 250 mm per month, with no seasonal extremes as those featured in the central region. Precipitation trends are shown in Fig. 3.4B. Statistically significant positive trends occur south of latitude  $5^\circ\text{N}$  between November and January, with increases ranging from 10 to 30 mm per decade. The summer season of May to September is marked by significant decreases in the trend, approximately  $7^\circ\text{N}$  to  $20^\circ\text{N}$ ,



followed by significant increases from 20°N to 29°N. A minor change occurs poleward of 29°N.

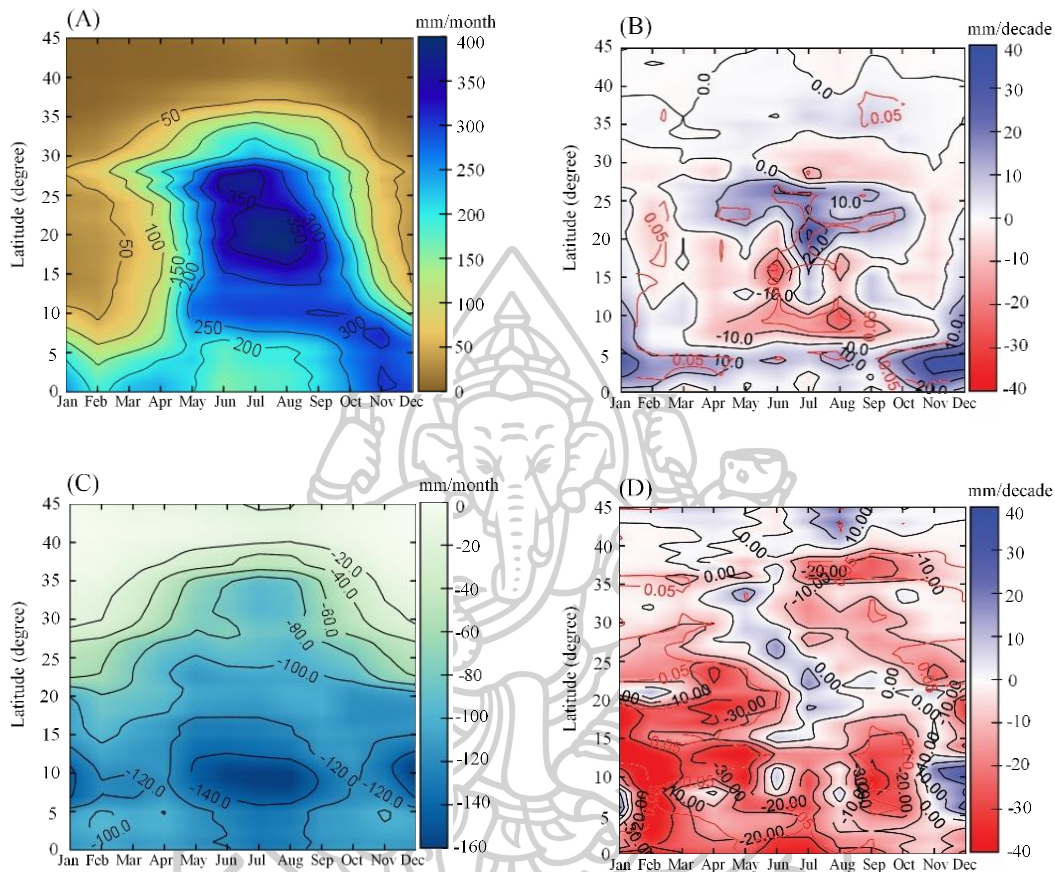


Figure 3.4 (A) Climatology of precipitation (mm per month). Data have been averaged for 40 years, 1979-2018 for every pixel representing latitude (y axis) and month (x axis), (B) as in Figure 3.4A but containing trends in mm per decade. Also shown is the  $p=0.05$  defining the 95% confidence limit, (C) as in Figure 3.4A but showing the E long-term averages in mm per month. (D) as in Figure 3.4B but showing trends in E in mm per decade. (E) as in Figure 3.4A but showing the P-E long-term averages in mm per month. (F) as in Figure 3.4B but showing trends in P-E in mm per decade. (G) as in Figure 3.4A but showing the HIRS-UTWV brightness temperature (Data has been averaged for 39 years, 1979-2017), (H) as in Figure 3.4A but showing trends in  $T_B$  in K per decade, (I) as in Figure 3.4A but showing the high cloud cover long-term averages, and (J) as in Figure 3.4B but showing trends in high cloud cover in [-] per decade.

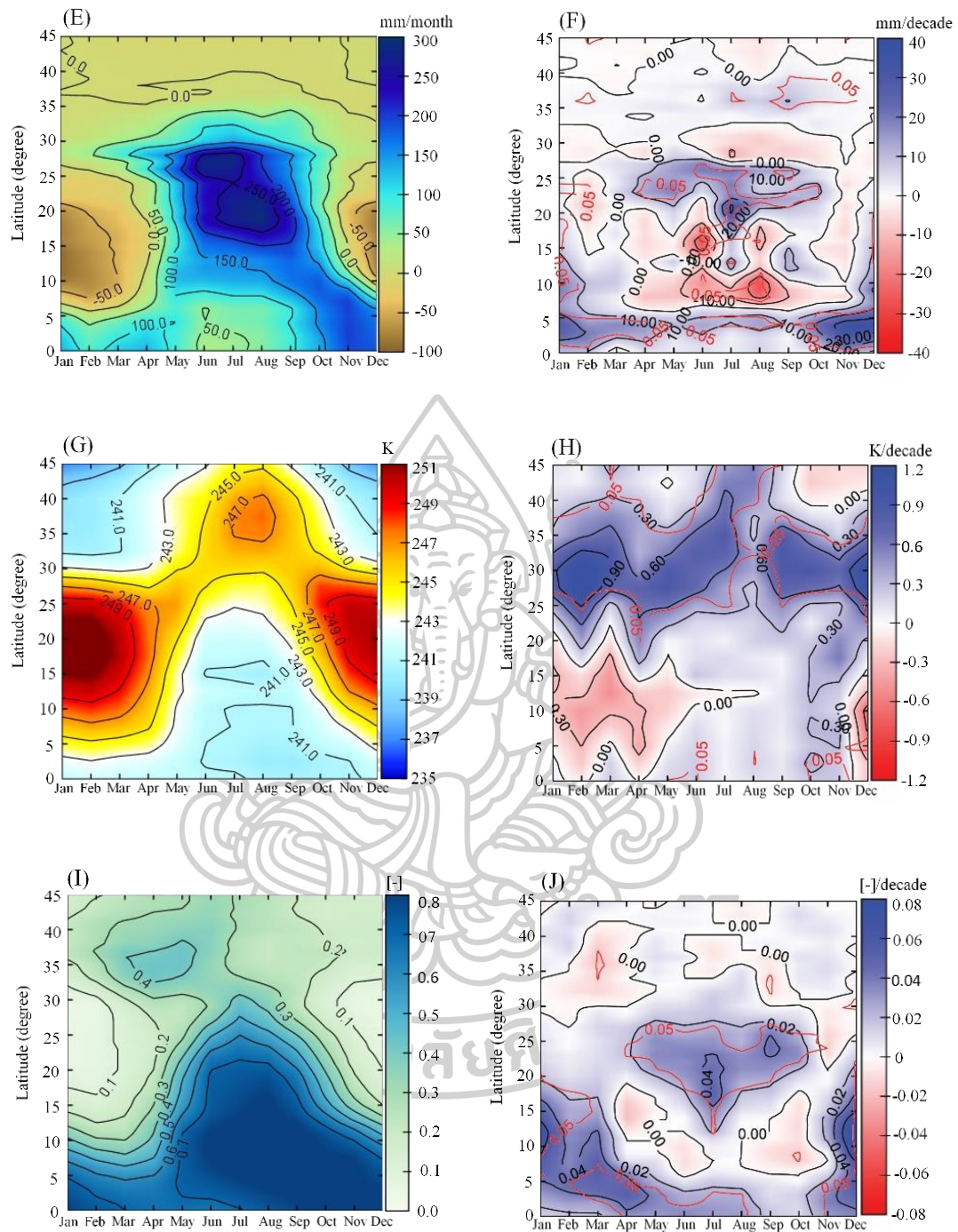


Figure 3.4 (continued). (Caption is shown on previous page.)

### 3.3.2 Precipitation minus evaporation (P-E)

The P-E climatology pattern (Figure. 3.4E) is similar to that of P (Fig. 3.4A). E (Figure 3.4C) exhibits seasonal changes, but they are less pronounced than those seen in P. Maximum P-E zones match the P maximum of the SW monsoon (Figure 3.4A).

P–E at latitudes  $15^{\circ}\text{N}$  is negative and reaches values less than  $-50$  mm per month in January, February, and December. During the summer months, the zero isolines can be found near the upper boundary of this study region, around  $40^{\circ}\text{N}$  at high latitudes. However, during the winter months, two zero contours occur: one at approximately  $6^{\circ}\text{N}$  and the other at around  $27^{\circ}\text{N}$ . As previously noted, this last zero boundary has been labeled as the edge of the subtropical dry zones (Lu et al., 2007; Waugh et al., 2018). P–E trends (Figure 3.4F) closely follow the P trend, indicating the strong control of P in the trend and the lack of significant changes in E (Figure 3.4D) over the study period.

### 3.3.3 Brightness temperature ( $T_B$ )

Figure 3.4G shows the seasonal development of tropospheric water vapor, which is broken down by latitude and month of the year. The SW monsoon from May to September is characterized by a high moisture intrusion. This intrusion can be observed by the poleward movement of the  $T_B = 245$  K isotherm. In contrast, the subtropical high is firmly established in December to February, and is characterized by  $T_B > 245$  K.  $T_B$  trends (Figure 3.4H) are dominated by increased  $T_B$  (lower moisture trend) in a latitudinal band extending from approximately  $25^{\circ}\text{N}$  to  $40^{\circ}\text{N}$ , with values of  $0.2$ – $0.6$  K per decade. The trend is also significant at the 95% confidence limit and strongest during the winter months at latitude  $30^{\circ}\text{N}$ . From the equator to approximately  $18^{\circ}\text{N}$ , there is a small tendency of increasing upper tropospheric moisture (decreasing  $T_B$ ), but it is not statistically significant. However, there is one exception, which occurs in a zone near the equator ( $0$ – $5^{\circ}\text{N}$ ) from October to December (Figure 3.4H), where statistically significant trends as high as  $-2$  K per decade are recorded.

### 3.3.4 High cloud cover ( $C_H$ )

The highest  $C_H$  values are attained from June to August, with 40% coverage reaching as far north as  $32^{\circ}\text{N}$  (Figure 3.4I). There is a zone of maximum cloud cover of over 80% that starts to develop in June and lasts for the rest of the year although it moves equatorward (Figure 3.4I). As expected, minimum values of 10% or less for  $C_H$  occur in December to February at latitudes  $25^{\circ}\text{N}$  to  $30^{\circ}\text{N}$ . Trends in Figure 3.4J show

a significant increase of around 0.02 per decade from May to October in the 15°N to 27°N latitudinal band. There are no significant trends northwards from latitude 27°N. During December to February significant increases of 0.04% per decade to 0.06% per decade also occur at 0°N to 20°N.

### 3.3.5 Summary of trends

The study combined features common to all three indices ( $P-E$ ,  $T_B$ , and  $C_H$ ) to determine the agreement degree, as shown in Figure 3.5. Figures 3.5A and 3.5B summarize the approximate boundaries of the significant processes in winter and summer, respectively. A region of increasing dryness, as observed by HIRS-UTWV from latitudes 25°N to 40°N, is common to all months. In winter, all three data sets show increased convection close to the equator, with slightly varying latitudinal and monthly spans. In summer, a region between 20°N and 25°N, where both  $P-E$  and  $C_H$  give increasing convection. In contrast,  $P-E$  decreases between latitudes 7°N to 20°N from June to August. Although no other data set other than the HIRS-UTWV set shows significant drying trends between latitudes 25°N to 40°N, both  $C_H$  and  $P-E$  show no trend or non-significant decreasing trends.



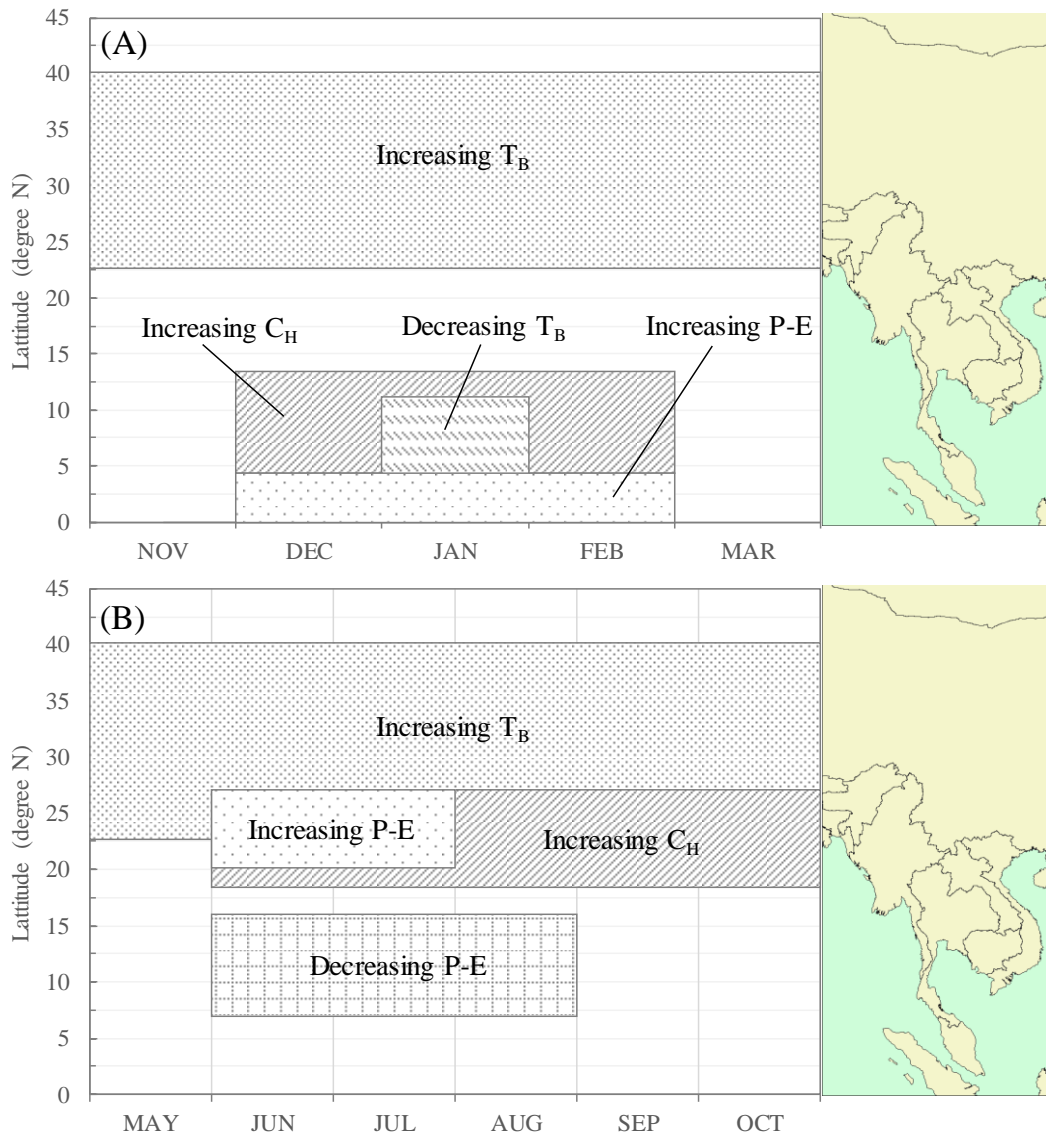


Figure 3.5 Summary of trends acting in the study area as a function of latitude and month for (A) Winter and (B) Summer.

### 3.3.6 Latitudinal movement of three indices of expansion

Table 3.3 summarizes my observations of latitudinal movement. All three indices migrate toward the pole to various degrees during the winter DJF season, and the migration rates were all significant at the 95% confidence level. The location of maximum  $T_B$ , which is associated with the dry anticyclonic center, migrates at a rate of  $1.327^\circ$  per decade. Typically, it shifts closer to the middle of the study region at around

15°N to 20°N (Figure 3.3A). In contrast, the latitude of the first zero crossing of P–E occurred close to the equator (Figure 3.3B), tracking poleward at 0.450° per decade, at a rate less than half of the migration rate of  $T_B$ . The latitude at which  $C_H$  reaches 50% migrates poleward at a rate of 0.889° per decade.

Table 3.3 Latitudinal movement of the three indices of expansion. Asterisks (\*) denote a 95% level of confidence.

Index	DJF (deg decade <sup>-1</sup> )	JJA (deg decade <sup>-1</sup> )
Latitude of maximum $T_B$	1.327 ± 0.030*	
Latitude of first zero crossing P-E	0.450 ± 0.021*	
Latitude of $C_H$ equal to 50%	0.889 ± 0.025*	
Latitude of $T_B$ below 242 K		0.399 ± 0.058
Latitude of first zero crossing P-E		0.223 ± 0.030
Latitude of maximum $C_H$		0.004 ± 0.025

In contrast to the DJF data, no significant trend was obtained with any of the indices during the JJA season. As a result, we focused on the winter DJF for the rest of the study. During DJF, we specifically examine the relationship between expansion and convection, wind flow, and climate indices.

### 3.3.7 Convection characteristics in the tropical zone during DJF

During the winter months, my three metrics show that the equator has the most convection, with convection decreasing poleward. However, there are specific details in the data that require closer examination as they provide further insight into the expansion process. These features are best shown using P–E and  $C_H$ , therefore the discussion of this study would be restricted to these two data sets. We start by visualizing the equatorial region as exhibiting a maximum P–E and  $C_H$  and decreasing monotonically at relatively high latitudes. Relevant parameters for P–E are the

maximum at the equator, the latitude of first zero crossing, the latitude of second zero crossing, and the latitude of the minimum. For  $C_H$ , we consider the maximum at the equator and the rate at which various cloud fractions (0.8, 0.7, ..., 0.10, 0.07, 0.05) travel poleward. Each of these variables is regressed against time.

Table 3.4 presents the coefficients of each regression and the significance of the slopes. The slopes are statistically significant at the 95% confidence level. Using these regressions, it is possible to calculate the main features of the latitudinal profiles of both P–E and  $C_H$  for any year. As shown in Figure 3.6A, the two endpoints (1979 and 2018) are used to observe time evolution.  $C_H$  increases at the equator and migrates northward with latitude changes of over  $5^\circ$ . Low  $C_H$  has a higher latitude change, although the overall change is limited to around  $29^\circ$  latitude. Figure 3.6B plots the change in minimum  $C_H$  over time. What appears as a regular  $C_H$  shift to higher latitudes stops at  $29^\circ$  with no further increase.

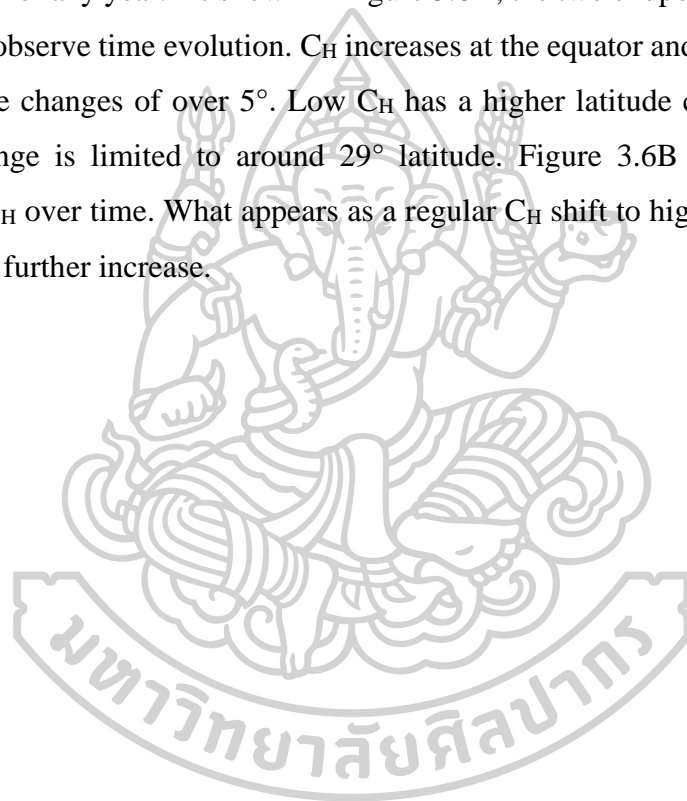


Table 3.4 Poleward travel of region of maximum convection at the equator during DJF.

Indices	Parameters related to the indices	Units	Intercept	Slope (mm yr <sup>-1</sup> )	R <sup>2</sup>	Tstat of slope	P value of slope
P-E	Max (P-E) increase at equator	mm yr <sup>-1</sup>	-2317	1.231 ± 0.449	0.169	2.74	0.009
	Lat of min (P-E)	deg yr <sup>-1</sup>	-180.20	0.097 ± 0.036	0.164	2.70	0.010
	Lat of first zero crossing	deg yr <sup>-1</sup>	-82.37	0.045 ± 0.021	0.114	2.18	0.036
	Lat of second zero crossing	deg yr <sup>-1</sup>	-16.99	0.022 ± 0.018	0.037	Not significant	Not significant
C <sub>H</sub>	Max C <sub>H</sub> increase at equator	% yr <sup>-1</sup>	-3.798	0.0023 ± 0.0009	0.141	2.46	0.019
	Lat of C <sub>H</sub> =0.7	deg yr <sup>-1</sup>	-250.44	0.128 ± 0.033	0.324	3.92	0.0004
	Lat of C <sub>H</sub> =0.6	deg yr <sup>-1</sup>	-222.47	0.115 ± 0.028	0.319	4.16	0.0002
	Lat of C <sub>H</sub> =0.5	deg yr <sup>-1</sup>	-168.76	0.089 ± 0.025	0.254	3.55	0.001
	Lat of C <sub>H</sub> =0.4	deg yr <sup>-1</sup>	-177.49	0.094 ± 0.023	0.315	4.13	0.0002
	Lat of C <sub>H</sub> =0.3	deg yr <sup>-1</sup>	-182.26	0.097 ± 0.022	0.351	4.47	7.1E-05
	Lat of C <sub>H</sub> =0.2	deg yr <sup>-1</sup>	-221.83	0.118 ± 0.022	0.447	5.47	3.3E-06
	Lat of C <sub>H</sub> =0.1	deg yr <sup>-1</sup>	-405.60	0.212 ± 0.036	0.482	5.86	9.6E-07
	Lat of C <sub>H</sub> =0.07	deg yr <sup>-1</sup>	-385.17	0.203 ± 0.056	0.269	3.64	0.0008
	Lat of C <sub>H</sub> =0.05	deg yr <sup>-1</sup>	-230.78	0.127 ± 0.067	0.102	Not significant	Not significant

Various values of parameters related to the indices in the Table were plotted against time to obtain several time series graphs and for each graph, a linear line was used to fit the graph. Consequently, intercept and slope were obtained. For each graph, R<sup>2</sup> indicates the coefficient of determination between the quantities plotted in the graph. Tstat of the slope indicates the statistical significance of the slope and P value of slope indicates the degree of the significance.



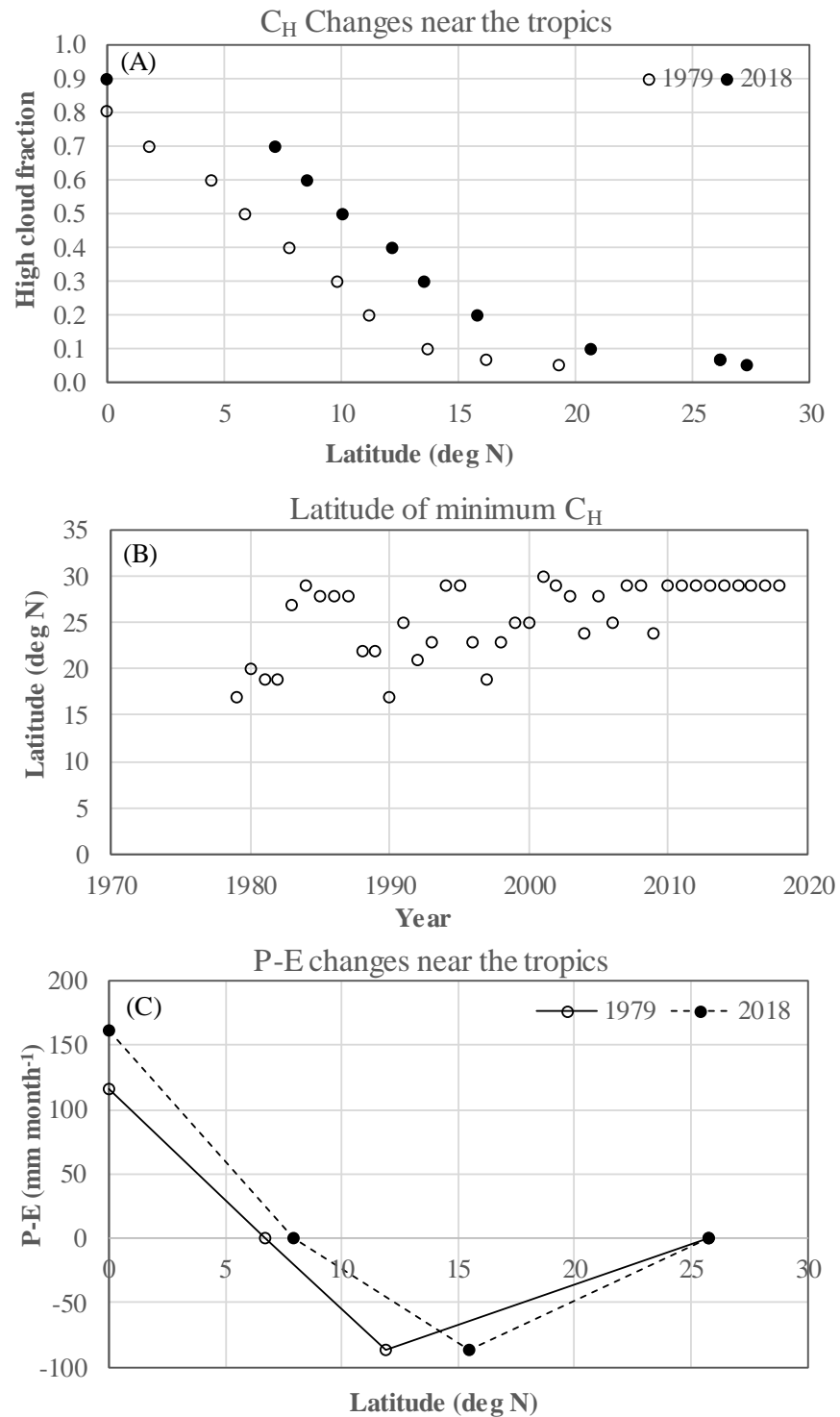


Figure 3.6 (A) Latitudinal displacement of  $C_H$  over the tropical region for DJF from 1979 to 2018. (B) Latitudinal changes in the minimum  $C_H$  for DJF over the period of record. (C) Displacement of P-E near the tropical region for DJF from 1979 to 2018. Points have been joined by a straight line for display purposes.

Figure 3.6C shows changes in P–E, which support the main characteristics of the northward migration of  $C_H$ . For display purposes, we combined the data points using straight lines. The first zero crossing, from 6.4°N to 7.9°N, coincides with a substantial increase in P–E, from 116.3 mm to 160.9 mm per month at the equator. The minimum P–E latitude also increased from 12.0°N to 15.5°N. The study takes the average for the entire record, which is –87.3 mm per month since the change in P–E minimum has little statistical significance. Finally, the latitude of the second crossing is also constant for both time periods at 25.8°N. Therefore, these records indicate an increased equatorial intensity and expansion, but they are limited to latitudes 29°N and 25.8°N for  $C_H$  and P–E, respectively.

Next, we examined the relationship between  $C_V$  and precipitation estimates from ERA-Interim since  $C_V$  relates to precipitation in the tropics. During DJF, the zonal averages of both P and  $C_V$  were obtained at 1° intervals for the entire study area. Grouping was done for the entire record period (1983 to 2016). At latitudes poleward of 20°N, it became evident that the relationship between these two variables had broken down. Although  $C_V$  might be common in mid-latitudes, many rain-bearing systems are probably unrelated to  $C_V$ . As a result, we have restricted the data sets to 0°N to 20°N, resulting in two 680 element vectors for  $C_V$  and P (20° latitude × 34 years). The results are presented in Figure 3.7.

The two data sets are highly correlated, with the following logarithmic relationship best describing them:

$$P = 72.918 + 50.138 \ln C_V + 11.225 (\ln C_V)^2 \quad (3.1)$$

$$R^2 = 0.87; \text{ std. error} = 29.4 \text{ mm month}^{-1}; n = 680$$

The logarithmic shape shows that  $C_V$  becomes less efficient as P increases, suggesting that the satellite signal becomes saturated and information is lost. However, the non-linearity in Eq. (3.1) provides good discrimination within the GMS and during the winter season. These results prove that  $C_V$  can be used as an independent variable

related to precipitation and can be derived from satellite measurements. As a result, we examine a possible northward migration in  $C_V$ .

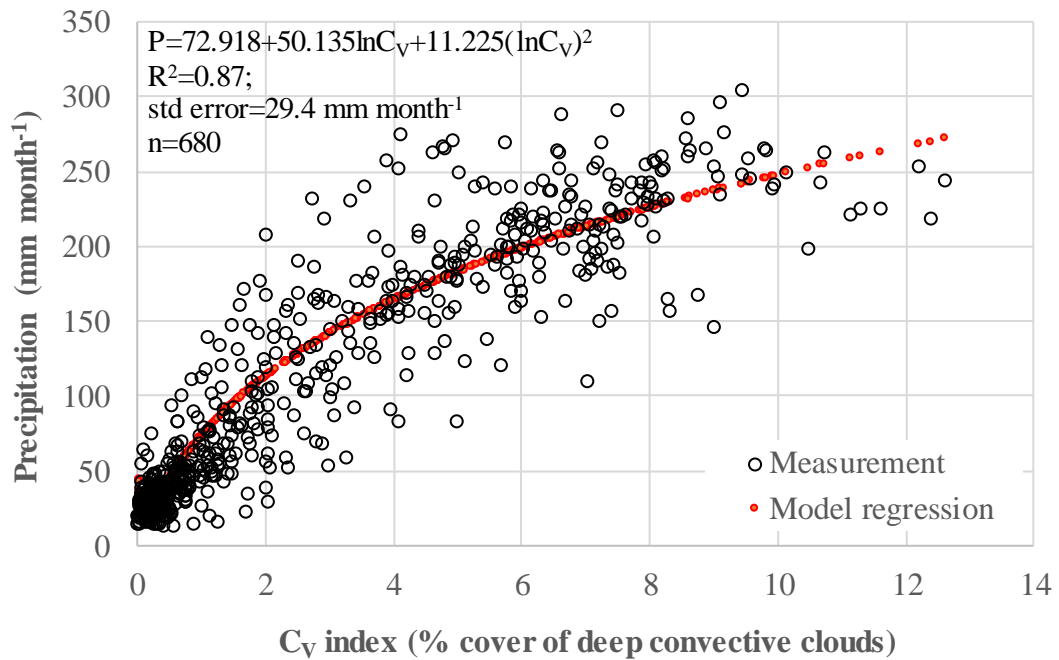


Figure 3.7 Plot of  $C_V$  for DJF vs  $P$  for the period 1983 to 2016. Each data pair represents an average of  $P$  and  $C_V$  over  $1^\circ$  of latitude. Only latitudes equatorward of  $20^\circ\text{N}$  have been recorded. There are 680 data pairs representing 34 years of data. Red dots represent a regression fit to the data.

We selected the latitude where  $C_V$  reaches a fixed value compared to its nominal maximum value at the equator, as we did for  $C_H$ . The data revealed a nonlinear decrease in  $C_V$  with latitude, which prompted us to establish an expansion index ( $\text{lat}_i$ ) as the latitude where  $C_V$  reached 80% of its equator value. Using winter (DJF) averages of  $C_V$ ,  $\text{lat}_i$  was estimated between 1983 and 2016. A linear regression analysis confirmed a poleward migration in  $\text{lat}_i$  at the 95% confidence level:

$$\text{lat}_i = 0.0852 \text{ yr}_i - 165.561 \quad (4.2)$$

$$R^2 = 0.153; T \text{ stat} = 2.4$$

where  $yr_i$  represents year at time  $i$ . A migration rate of  $0.0852 \pm 0.035^\circ$  per year or  $0.852^\circ$  per decade correlates well with migration rates of  $0.097 \pm 0.036^\circ$  per year and  $0.089 \pm 0.023^\circ$  per year for P–E and  $C_H$ , respectively. Here  $C_H$  is being defined as the latitude where  $C_H$  is 50% of the equatorial value.

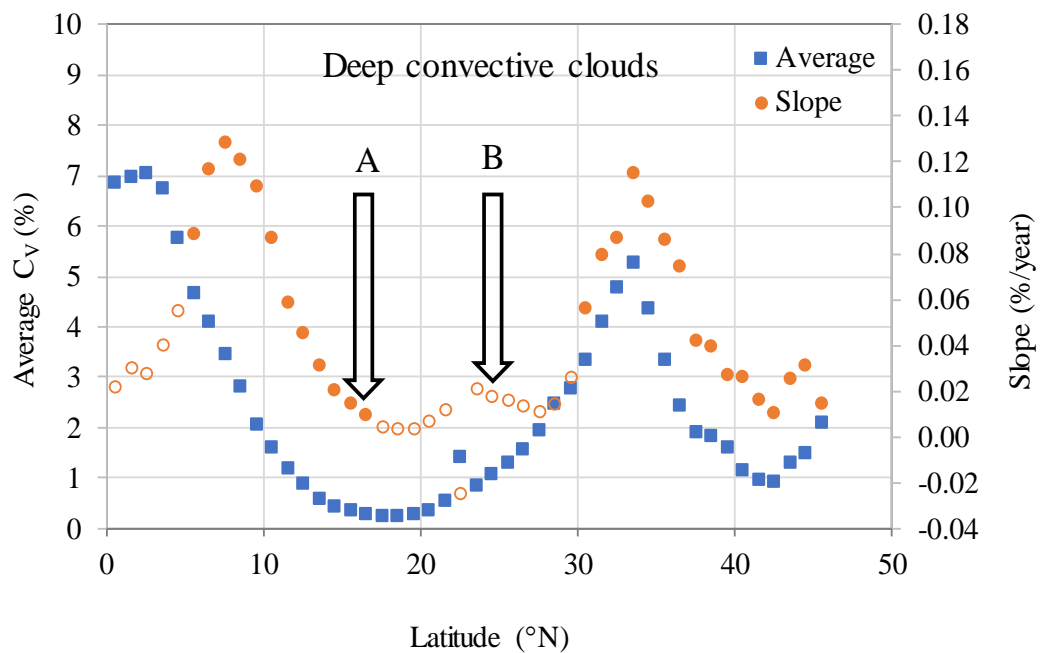


Figure 3.8 Change in deep convective cloud for the study area. Data have been averaged across latitude bands bounded by  $90^\circ\text{E}$  to  $110^\circ\text{E}$ . Full circles denote a statistically significant slope at the 95% confidence level. Open circles denote no statistical significance. A denotes the mean latitude, where high clouds  $C_H$  reached a low value of 0.1 (Figure 3.6) and B denotes the mean latitude of the second zero crossing P-E, with increasing P-E poleward (Figure 3.6).

Figure 3.8 shows the zonal averages and changes in  $C_V$ . The average pattern clearly describes the maxima corresponding to tropical and westerly weather systems. This study obtained a maximum value of approximately 7% near the equator, with

slightly lower values of around 5.2% in the westerly dominated systems. Yearly percent changes to  $C_V$  also show two peaks, with the tropical peak displaced slightly north to  $7.5^\circ\text{N}$ . There is also some connection between the latitude where  $C_H$  and  $C_V$  reach low values (Arrow A in Figure 3.8) and the start of convection by westerly systems (Arrow B in Figure 3.8). An intriguing feature is the persistence and increasing trends in  $C_V$  northward of latitude  $23^\circ\text{N}$  despite no evidence of increasing P–E and evidence of increasing  $T_B$  (Figure 3.6).

We calculated temporal changes in  $C_V$  by averaging  $C_V$  across northern ( $25^\circ\text{N}$ – $45^\circ\text{N}$ ;  $90^\circ\text{E}$ – $110^\circ\text{E}$ ) and southern ( $0^\circ\text{N}$ – $25^\circ\text{N}$ ;  $90^\circ\text{E}$ – $110^\circ\text{E}$ ) regions and then averaging it over the three winter months to get a yearly  $C_V$ . Figure 3.9 shows trends in  $C_V$  for both regions. The two slopes are increasing and are statistically significant at the 95% confidence level.

Despite increasing  $C_V$  over time in the northern region, there is no evidence that  $C_V$  is related to monthly precipitation in this region, which is dominated by westerlies and other rain-bearing systems. Furthermore, Figure 3.4B shows no significant change in precipitation northward of  $25^\circ\text{N}$ . As a result, we focused on the southern region for the rest of the study, which examines regional wind flow and climate indices.



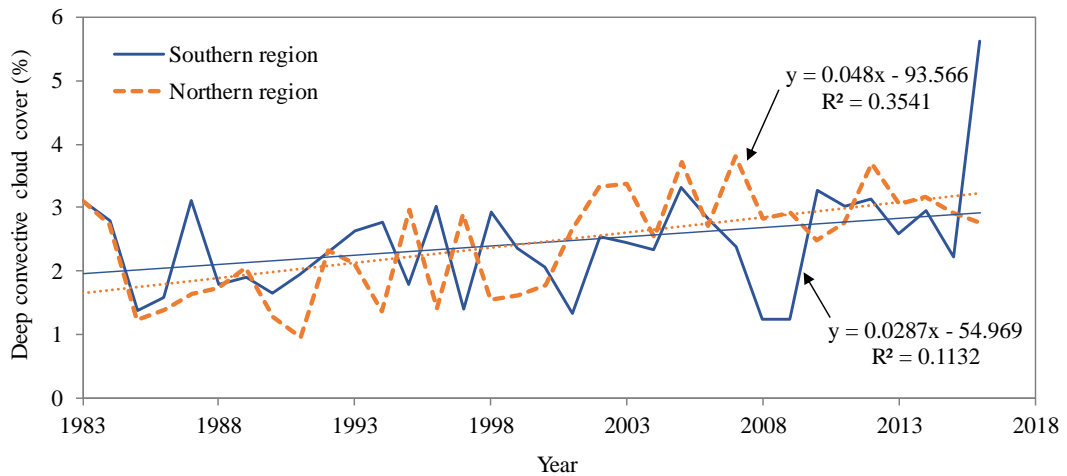


Figure 3.9 Yearly average deep convective cloud cover in the study area for two regions: the northern region (25°N-45°N; 90°E-110°E) marked in dash line and the southern region (0°N-25°N; 90°E-110°E) marked in thick line. Both trends are significant at the 95% confidence level.

### 3.3.8 Regional wind flow

Three metrics are used to illustrate noteworthy features of the winter expansion close to the equator. However, distinguishing what is a locally driven expansion from what is a signal representing a widespread global trend is difficult. We examined regional wind flow to aid in the analysis, as described below.

We used eastward wind speed (U) at 850 hPa as an index of wind flow. Data were sourced from MERRA (MAIMNPANA V.5) and ERA-Interim as discussed in Section 3.2.2.2. These data were provided monthly and were downloaded for the study area yearly for the DJF period. Wind speed for each latitude was then averaged across all longitudes and then averaged across all years, as shown in Figures. 3.10A and 10B. Westerly winds from 0°N to 5°N, easterly winds from 6°N to 20°N, weak westerlies from 20°N to 28°N, weak easterlies from 28°N to 35°N, and westerlies northward from 29°N are the most prominent features.

One outstanding feature is a region of strong easterly wind speeds centered at 10°N, which is close to the zone of maximum convection in Figure 3.8. Maximum

HIRS-UTWV brightness temperature occurs at around 20°N in winter (Figure 3.4G) and these low U values are likely to relate to the downwelling part of the Hadley cell. No latitudinal band exhibited significant changes in U with time over the study period, as shown in Figures. 3.10A and 3.10B.

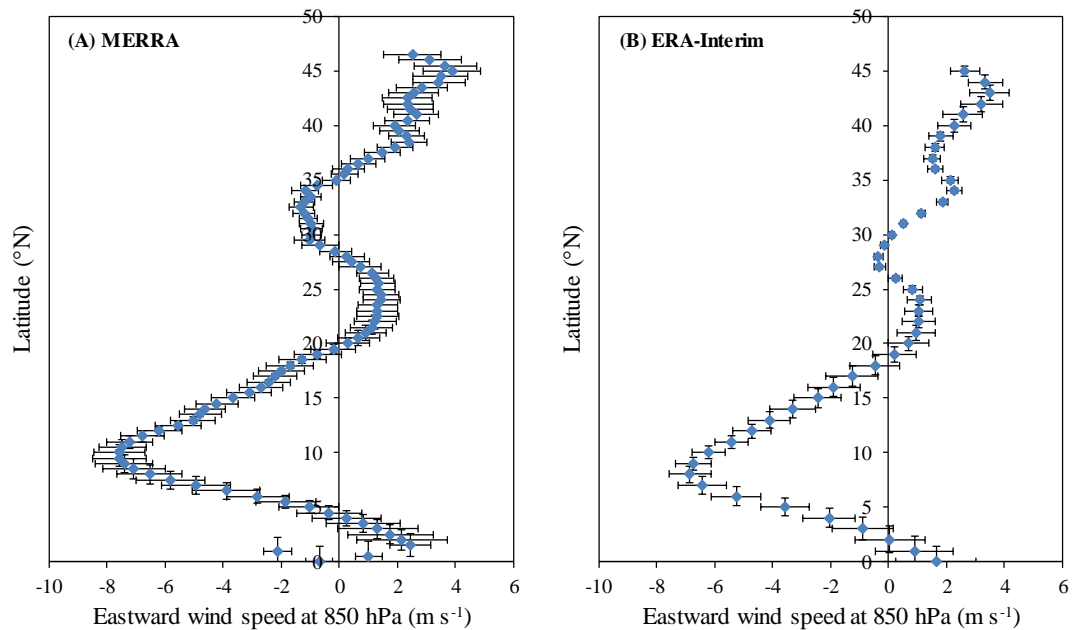


Figure 3.10 Plots of (A) MERRA and (B) ERA-Interim eastward wind speed vs. latitude for the study area during DJF. Wind speed was averaged across longitudinal bands 90°E-110°E and further averaged over the study period. Standard deviations are given as error bars for each latitude.

### 3.3.9 Relationships with climate indices

For analysis, we selected five indices that could influence expansion in the southern region. They include the Southern Oscillation Index (SOI), Sea Surface Temperature (SST) averaged over the warm pool in the southwest Pacific (Hoerling et al., 2010), the PDO, Aerosol Optical Depth (AOD) from MERRA, and the East Australia Winter Monsoon Index (EAWMI) (Wang & Chen, 2014). The SOI was downloaded from [www.esrl.noaa.gov/psd/gcos\\_wgsp/Timeseries/SOI/](http://www.esrl.noaa.gov/psd/gcos_wgsp/Timeseries/SOI/), and it comprised monthly normalized data (1979–2018) calculated using the method of

Ropelewski and Jones (1987). A PDO index (Mantua et al., 1997) of monthly SST was downloaded from the same site. AOD data from Modern-Era Retrospective Analysis for Research and Application Aerosol Reanalysis (MERRA) was obtained from the NASA website ([www.gmao.gsfc.nasa.gov/reanalysis/merra/MERRAero/data](http://www.gmao.gsfc.nasa.gov/reanalysis/merra/MERRAero/data)). We obtained AOD monthly from 1980 to 2018, with a resolution  $0.5^{\circ}\text{N} \times 0.625^{\circ}\text{E}$  and a range of  $5^{\circ}\text{N}$  to  $30^{\circ}\text{N}$  and  $90^{\circ}\text{E}$  to  $110^{\circ}\text{E}$ . The study then spatially averaged these monthly data to determine a monthly AOD. The EAWMI was obtained using monthly average sea level pressures from ERA-Interim. These results were compared with our three metrics of expansion and  $C_V$ .

Next, we examined the southern region, which encompasses most of the GMS and is subject to tropical influences. The only indices that have a significant correlation with the metrics  $C_H$  and  $C_V$  are SOI and SST (Table 3.5). When both SOI and SST are used as  $C_V$  predictors, the coefficient for SOI is negative, while that of SST is positive. The SOI coefficient has one star next to it, indicating that SOI and  $C_V$  are offset by one year, with SOI estimated a year earlier during DJF. Two stars denote both variables are taken during the same time interval in DJF. Individual correlations in Table 3.5 show that SST is a stronger predictor. These results suggest that SST is modulated by a strong interannual response due to SOI, resulting in an increased  $C_V$ .

### 3.4 Discussion

A significant poleward expansion occurred during the winter season (DJF) with all three indices used (Table 3.3),  $T_B$  ( $1.327^{\circ}$  per decade),  $C_H$  ( $0.889^{\circ}$  per decade), and P–E ( $0.450^{\circ}$  per decade). It is worth noting that expansion due to P–E first zero crossing using ERA-Interim in DJF for the entire northern hemisphere was examined over the same period as this study. A trend of  $0.442^{\circ}$  per decade was obtained, which was very close to the GMS regional value. Based on the three indices, results of this work show that the tropical expansion in GMS is most visible in the winter, whereas other studies (Allen et al., 2012; Hu et al., 2018; J. Liu et al., 2012) suggest that the expansion is more significant on a global scale in the summer. One possible explanation is that the monsoon circulation in the GMS region, which is based mainly on land/sea temperature



differences in summer (Yang & Lau, 1998), obscures the tropical expansion, making the expansion in winter more prominent.

My results, based on three indices, are consistent with other data. Global estimates based on reanalysis data and various indices over the last few decades range from  $-0.5^\circ$  to  $3.1^\circ$  per decade (Davis & Birner, 2017; Hu & Fu, 2007; Lucas et al., 2014), with the majority around  $0.5^\circ$  per decade (Davis & Birner, 2017). Other observation studies employ microwave-sounding data, radiosonde networks, and HIRS-UTWV to get estimates ranging from  $0.42^\circ$  to  $1.57^\circ$  (Fu et al., 2006; Lucas & Nguyen, 2015; You et al., 2015).

Although there were no published regional analyses for our area, there have been published studies at or close to the Asian region. Using radiosondes, Lucas and Nguyen (2015) reported rates ranging from  $0.47^\circ$  to  $0.79^\circ$  per decade for Asia. Using HIRS-UTWV, You et al. (2015) calculated  $1.52^\circ$  per decade for the western Pacific. These estimates are within a reasonable range of our values. For a comprehensive overview of documented expansion and the published literature, the reader is referred to the reviews by Staten et al. (2018) and Lucas et al. (2014).

Temporal changes occur in both DJF and JJA seasons. As shown in Figure 3.4B, tropical regions experience an increase in moisture during DJF. This scenario is consistent with studies that report increased precipitation in tropical regions resulting from atmospheric aerosols (Byrne & Schneider, 2016; Kovilakam & Mahajan, 2016; Lau et al., 2006; Lau & Kim, 2015; Zhou et al., 2019).

A large region of increasing  $T_B$ , encompassing  $25^\circ\text{N}$  to  $40^\circ\text{N}$  and significant at the 95% confidence level, is visible in both seasons. You et al. (2016) reported increasing  $T_B$  and a drying trend from HIRS-UTWV in a region over the Tibetan Plateau, with values of around 0.6 K per decade on an annual basis. The trends are similar to ours although their study region in the Tibetan Plateau is displaced slightly to the west of the northern boundary of this study. There is some disagreement between the region of increasing  $T_B$ , suggesting a drying trend centered at  $30^\circ\text{N}$  and the region of maximum  $C_V$  increases, centered at  $35^\circ\text{N}$  (Figure 3.4H and Figure 3.7). These small latitudinal differences could be due to uncertainties in satellite data processing since the increase in  $C_V$  is related to mid-latitude processes, as previously discussed.

Out of the three metrics of expansion used for the entire study area, only  $C_H$  was significantly related to two climate indices, SOI and SST (Table 3.5). These two indices also relate significantly to  $C_V$ . However, the sign and magnitude of the coefficients reveal some intriguing expansion features in the region. A negative SOI tends to decrease the  $C_H$  (contraction, Table 3.5) while increasing  $C_V$  (enhancement, Table 3.5). This inverse relationship between  $C_V$  and  $C_H$  is not as strong as the  $R^2$  terms in Table 5, which are significant but not high. Nevertheless, they aid the “elevated heat pump theory” formulated by some authors (Byrne & Schneider, 2016; Kovilakam & Mahajan, 2016; Zhou et al., 2019).

Table 3.5 Statistics of regression between  $C_H$ ,  $C_V$  and two climate indices. Regression coefficients significant at the 95% level of confidence are in BOLD.  $C_H$  is calculated as the latitude where  $C_H=0.5$  and  $C_V$  is averaged over latitude bands of the study area (0°N- 25°N). T statistic for each coefficient are shown in brackets.

	<b>SOI</b>	<b>SST</b>	<b>Const.</b>	<b>R<sup>2</sup></b>
$C_V$	<b>-0.392*</b> (-3.4)	<b>1.491</b> (2.4)	2.269 (16.6)	0.302
$C_V$	-0.326* (-2.4)	-	2.394 (17.2)	0.159
$C_V$	-	1.027 (1.5)	2.340 (15.0)	0.060
$C_H$	<b>1.225**</b> (5.5)	<b>2.507</b> (2.2)	8.925 (32.3)	0.488
$C_H$	1.175** (5.0)	-	9.056 (35.1)	0.418
$C_H$	-	1.849 (1.2)	8.776 (25.8)	0.038

\* SOI calculated in DJF of the previous year as  $C_V$ .

\*\* SOI calculated in DJF of the same year as  $C_V$ .

### 3.5 Conclusion

In this study, a series of data sets has been used to estimate the poleward expansion of various climate indices in the GMS region. They consisted of  $T_B$  from HIRS-UTWV, ERA-Interim P-E and  $C_H$ , TRMM LB3 precipitation data, and percent coverage of deep convective cloud from ISCCP. All data were analyzed monthly and

then zonally averaged. The three indices were subjected to types of analysis: temporal trends from 1979 to 2018 inclusive and latitudinal movement. Latitudinal movements of the indices were estimated for the summer (JJA) and the winter (DJF) seasons, with changes made over 12 months. The investigation of this work detected a pronounced expansion during the boreal winter. No evidence of expansion was obtained during the summer monsoon.

Winters near the tropics are distinguished by increasing convection and precipitation, whereas higher latitudes (25°N–39°N) experience a drying tendency. During the summer monsoon, we obtained increasing moisture from 5°N–19°N and a broadly drying trend from 20°N–40°N. During DJF, there is a significant poleward movement of the three indices ranging from 0.450° to 1.327° per decade. The analyses of this work show that in winter, the tropical zone expands at the expense of the dry zone where  $P-E < 0$ . There was no evidence of poleward movement during the summer monsoon period.

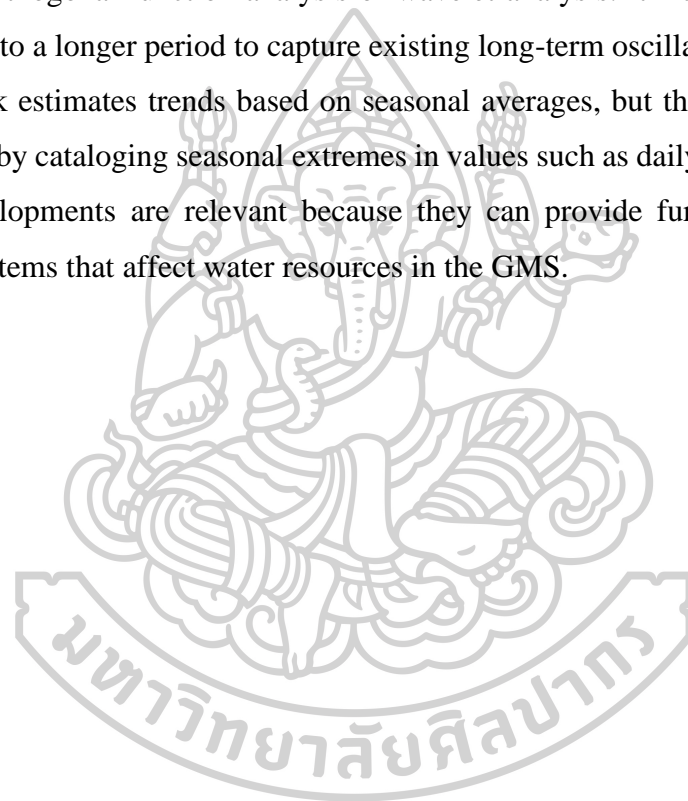
There are decadal increases in  $C_V$  in the southern study area which are related to increasing SST, but it was modulated by a strong SOI. Similarly, the  $C_H$  moves northward when long-term SST increases, although it may retreat (advance) with a negative (positive) SOI phase.

While the latitudinal winter expansion matches global estimates, there is no movement in the summer expansion, which is not consistent with global figures. We conclude that this study results are dominated by regional processes.

The results of this study show that precipitation increases northward of 17°N during the summer monsoon, but decreases southward. Many northern catchments of the Mekong River are located north 17°N, where rice production using monsoon rainfall as a natural irrigation source is common (Bestari et al., 2006; Oldeman & Frere, 1982; Titapiwatanakun, 2012). Increasing precipitation is beneficial because of the present high demand for water in the region (Commission, 2018). A drying trend south of 17°N will harm farming activities that rely on summer monsoon rainfall. These include southern Vietnam and southern Thailand, where rice, vegetables, and corn are produced using rain-fed irrigation (Chainuvati & Athipanan, 2001).

Dry season crops and rain-fed irrigation is being practiced in southern Thailand, southern Vietnam, and Cambodia. Typical crops, such as rice, mixed fruit, corn, and peanuts, are produced (FAO, 2011). These activities will benefit from a climate with increased precipitation and a northward migration of the convective systems discussed earlier.

More studies are being planned for the future. Spatial and temporal expansion processes during the winter could be examined in more detail using techniques such as empirical orthogonal function analysis or wavelet analysis. It may involve extending the data set to a longer period to capture existing long-term oscillations. The technique of this work estimates trends based on seasonal averages, but these records could be augmented by cataloging seasonal extremes in values such as daily precipitation or  $C_v$ . These developments are relevant because they can provide further information on weather systems that affect water resources in the GMS.



## Chapter 4

### **An investigation of poleward expansion of the Hadley circulation using high cloud cover<sup>2</sup>**

In chapter 3, the indices were used to investigate the tropical expansion. This chapter we use high cloud cover to indicate the poleward expansion of the tropical zone. The details of the work are as follows.

#### **4.1 Introduction**

The Hadley circulation generally refers to closed cells of the atmospheric circulation between the equator and the subtropics, both in the northern and southern hemispheres. The air rises up near the equator to a height of about 15 km, and then flows toward the north and south poles and sinks in the subtropics. Afterwards the air flows back toward equator along the surface of the Earth. The impacts of this phenomenon can cause more moist air, cloud and rain in the equator region, while subtropical regions are very dry as shown in Figure 4.1. Thus, the Hadley cells can dominate tropical and subtropical climates. Various studies of the Hadley cell suggested that the tropical zones are poleward expanded since 1979 (Hu & Fu, 2007; Mantsis et al., 2017; Nguyen et al., 2013). However, they measured the magnitude of the expansion differently (Lucas et al., 2014) which may be due to the difference of datasets and the length of period. The effects of the tropical expansion may increase drought in subtropical zones and increase floods in the tropical zone. Accordingly, it is interesting to study this expansion.

---

<sup>2</sup> This chapter has been published in Journal of Physics: Conference Series (Vol. 1380, No. 1, p. 012007).

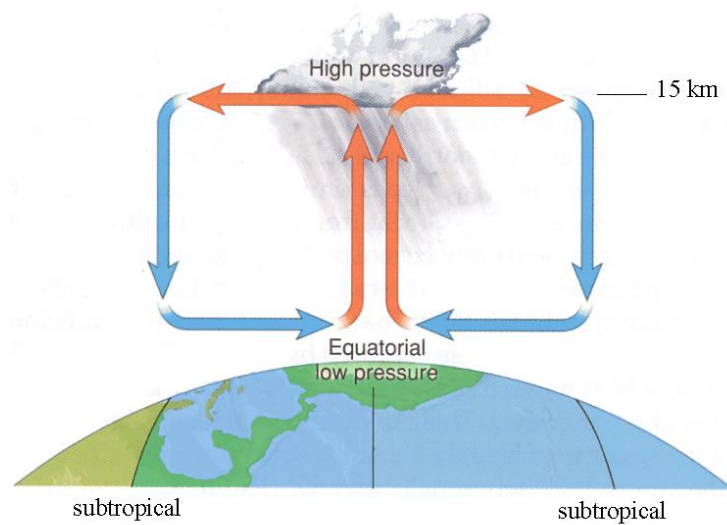


Figure 4.1 Hadley circulation.

Therefore, the objective of this study is to investigate the expansion of the Hadley cell in both hemispheres by using high cloud cover to indicate the edge of the Hadley cell. As from the feature of the circulation, in the tropical zones, there are a lot of clouds. In contrast, in the subtropical zones, there is less cloud. Thus, in this work, the variation of cloud cover was used as an indicator of the expansion of the Hadley cells.

#### 4.2 Data

To analyse the expansion of the Hadley circulation, we collected high cloud cover from the European Centre for Medium-Range Weather Forecasts (ECMWF), denoted by ERA-Interim reanalysis (Dee et al., 2011). The monthly cloud cover data over the globe were used from January 1979 to December 2017 (39 years). The resolution of these data is  $0.25^\circ$  latitude  $\times$   $0.25^\circ$  longitude. An example of high cloud cover from ERA-Interim is shown in Figure 4.2. The zonal-mean high cloud covers were computed by averaging the values of the cloud cover along the latitudinal lines of each month and year, as shown in Figure 4.3.

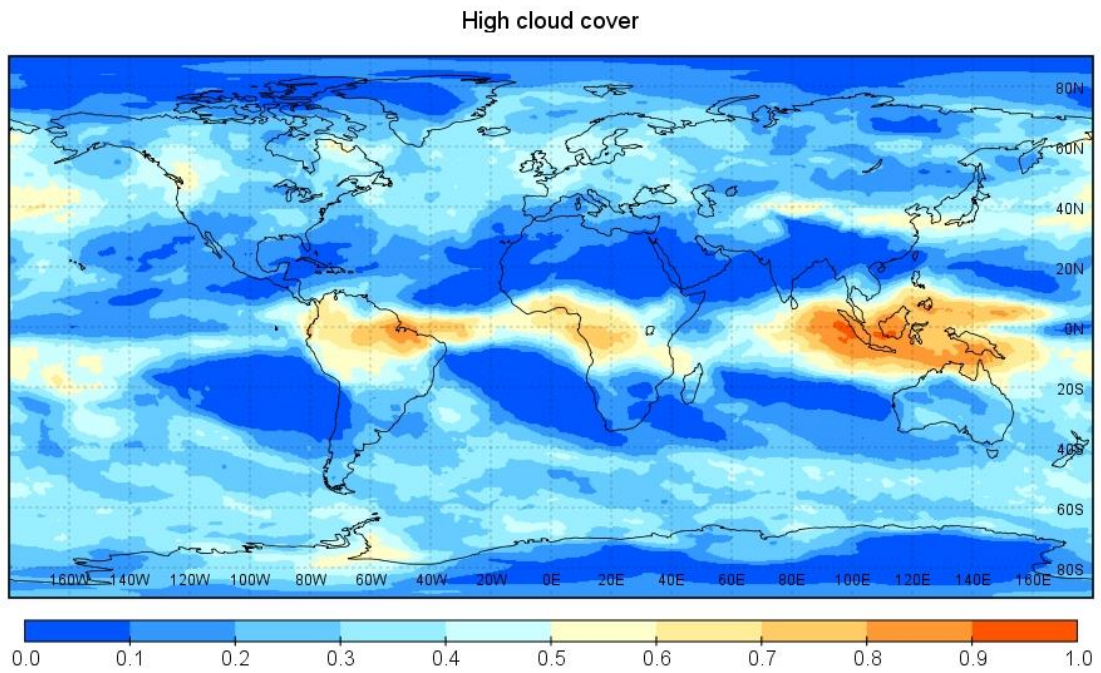


Figure 4.2 High cloud cover over the global region from ERA-Interim.

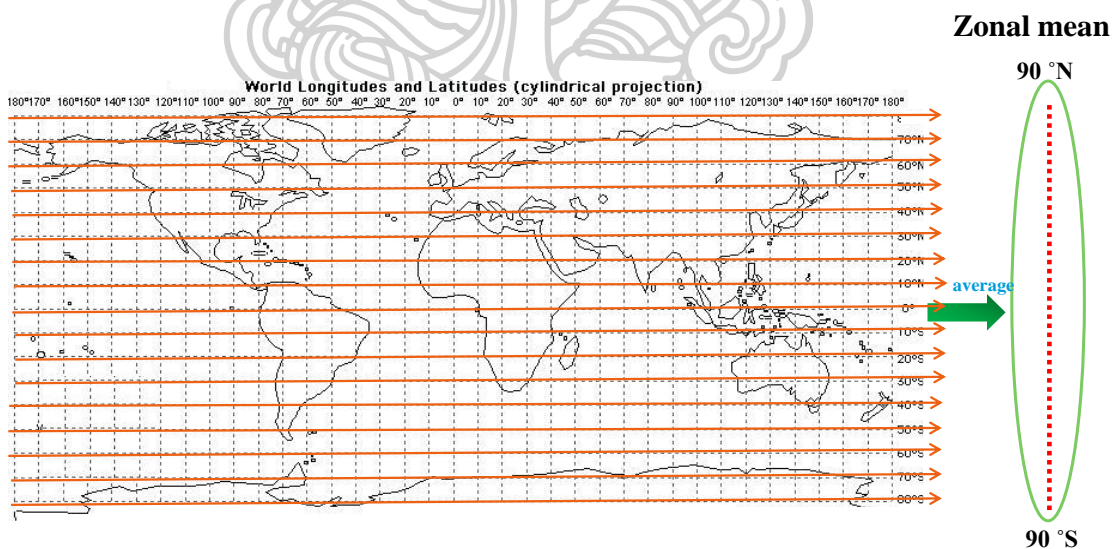


Figure 4.3 The process of zonal mean high cloud cover

The zonal-mean values of high cloud cover of each month and year were plotted against the latitude as shown in Figure 4.4.

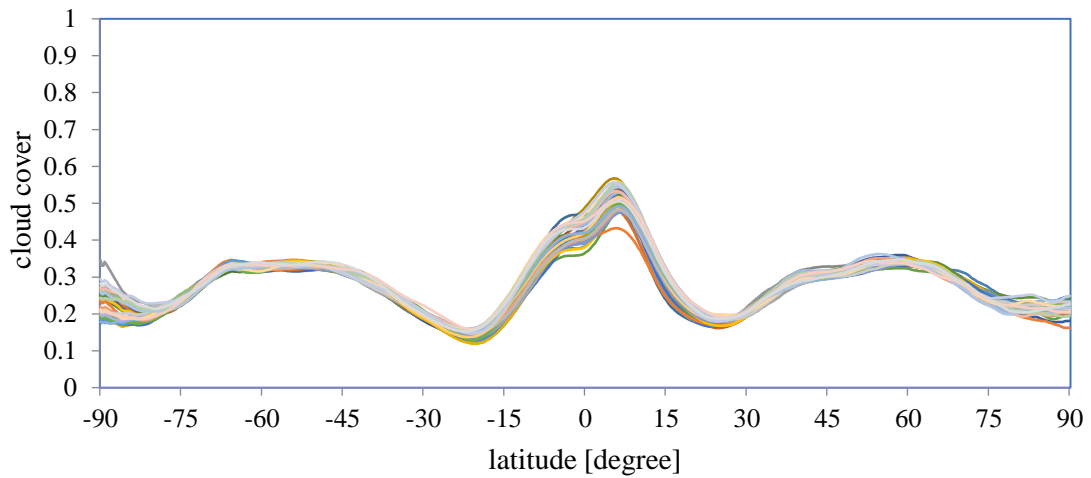


Figure 4.4 Variations of zonal mean high cloud cover in month from 1979 to 2017 (each colour represents each month)

For the analysis, we defined the edge of the Hadley cell by the position which cloud cover is minimum in the subtropical zone of both hemispheres. To observe the expansion, time series of ten-year running average (Liu et al., 2012) of the edges of the Hadley cells for both hemispheres were demonstrated. The expansions of each hemisphere for each season were also investigated. For the northern hemisphere, winter is in the period of December-February (DJF), spring is in the period of March-May (MAM), summer is in in the period of June-August (JJA) and autumn is in in the period of September-November (SON). For the southern hemisphere, summer is in in the period of December-February, autumn is in in the period of March-May, winter is in in the period of June-August and spring is in in the period of September-November.

### 4.3 Results

Figure 4.5 shows time series of the edge of the Hadley cells. Figure 4.5a is for the northern hemisphere and Figure 4.5b is for the southern hemisphere.



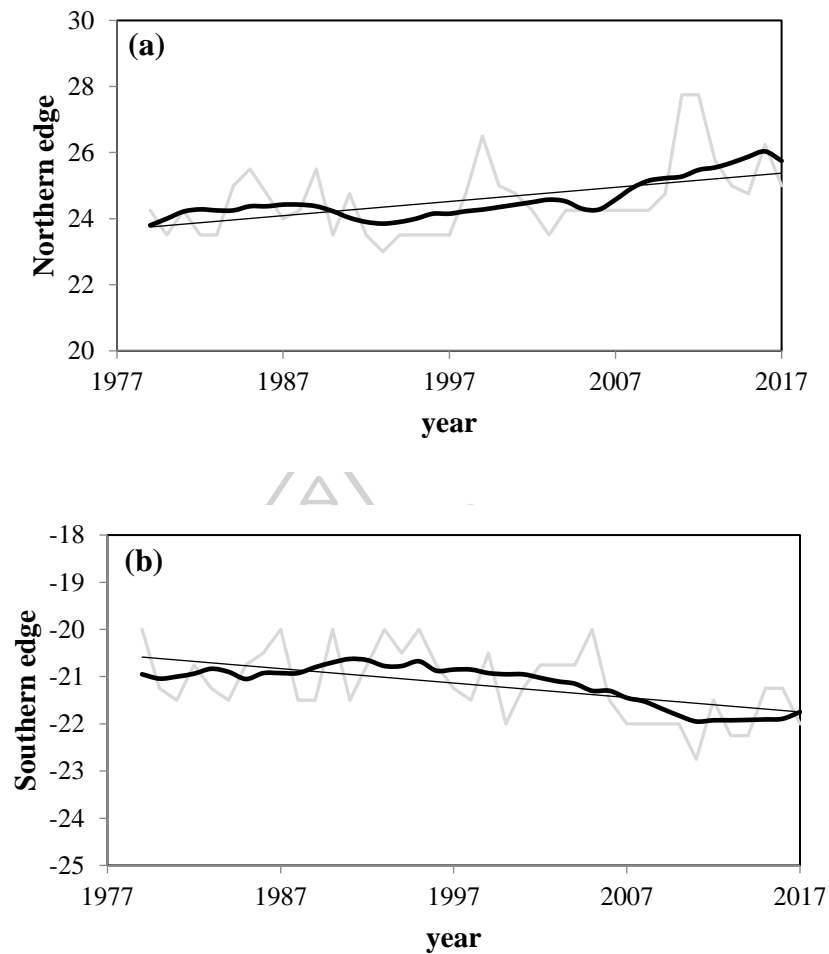


Figure 4.5 Time series of the annual-mean (grey line) and 10-year running mean (black line) edge of the Hadley Circulation for 1979-2017: (a) the poleward shift of the edge for the northern hemisphere and (b) the poleward shift of the edge for the southern hemisphere.

From Figure 4.5a, in the northern hemisphere, the Hadley cell edge is continue to increase from 1979 to 2017 showing that it is poleward expanded during this period ( $1.6^\circ$  in the latitude per 39 years). The Mann-Kendall test confirmed that the poleward expansion is statistically significant at the 95% confidence level. In case of the southern hemisphere, Figure 4.5b also shows poleward shift of the Hadley cell as similar as that shown in Figure 4.5a. Trend of the shift from 1979-2017 indicated that the Hadley cell has poleward shift ( $1.2^\circ$  in the latitude per 39 years, it is also significant at the 95%) which is smaller than that for the northern hemisphere.

In addition, the results of poleward shift of the edge of the Hadley cells for each season in both hemispheres are summarized in Figure 4.6. In the northern hemisphere, poleward shift occurs in all four seasons. The statistical significance of the poleward shifts over the period 1979-2017 are  $2.4^\circ$ ,  $2.2^\circ$ ,  $1.8^\circ$  and  $2.2^\circ$  latitude per 39 years for the winter, spring, summer and autumn, respectively. In the southern hemisphere, there are significant poleward shifts of the Hadley cell in all seasons except in summer, which is equatorward shift of about  $0.4^\circ$  latitude per 39 years, and it is not statistically significant at the 95% confidence level. The poleward shifts of the poleward edge in southern hemisphere since 1979 are about  $1.4^\circ$ ,  $1.2^\circ$  and  $1.2^\circ$  latitude per 39 years for the autumn, winter and spring, respectively. Therefore, it can be concluded that the Hadley cell was expanded from 1979 to 2017, exception in DJF where the expansion can see only in the northern hemisphere.

The results obtained in this work is consistent with those of Hu and Fu (2007) who investigated the expansion of Hadley cell using mass stream function and long wave radiation. These implies that the high cloud cover can be use as index to indicate the tropical expansion.

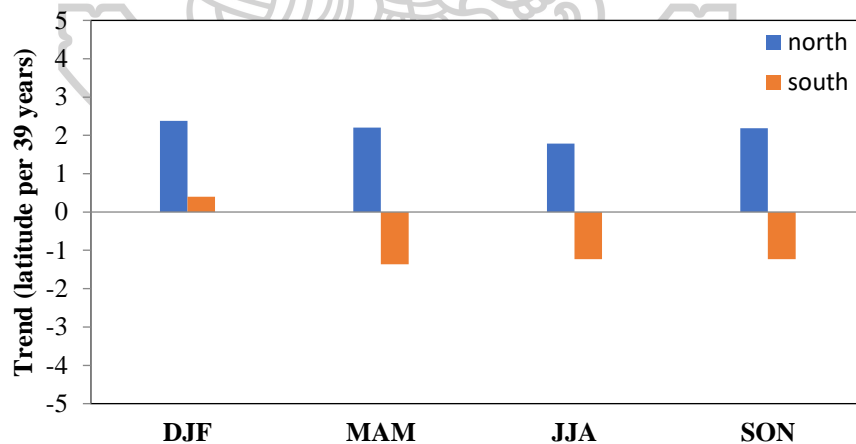


Figure 4.6 Poleward shift of the latitude edge of the Hadley cell in northern hemisphere (blue) and in southern hemisphere (red). Positive values indicate northward shift and negative values indicate southward shift.

#### 4.4 Conclusion

In this work, the poleward shift of the Hadley cell was investigated using cloud cover from ERA-Interim reanalysis data. Results from trends of high cloud cover data during the period 1979-2017 indicated that the Hadley circulation was poleward expanded in both hemispheres. However, the magnitudes of poleward shift are slightly different from other previous studies. This result is interesting and raises the questions how the expansion can be measured and what are the causes of the expansion. Also the effects of the expansion on the global climate change need to be investigated.



## Chapter 5

### Effects of tropical expansion on climate in Thailand

Tropical expansion may have influences on the climate. As Thailand has various agricultural activities and conditions, so we focused our study on flood and drought which could be indicated by the Standardized Precipitation Index (SPI). The details of the study are as follows.

#### 5.1 Flood and drought

Flood and drought are extremely events that play an important role in human life, natural environment, agriculture and ecosystem. They can be caused by variability of climate and hydrological cycle. The details of flood and drought can be described as follows.

##### 5.1.1 Flood

Flood is defined as high flow, overflow or inundation by water that causes or threatens damage. The main factors causing flood are heavy rain or prolonged precipitation, snowmelt, thunderstorms and storm surges from hurricanes. Human activities can also be a cause of flood, for example, land used/land cover, and water management. Floods may be divided into three types that are riverine floods (monsoon floods), coastal floods and urban floods. The riverine flood happens when the main rivers overflow and water is above danger level. Coastal floods occur in the coastal area as strong onshore wind drives water from the ocean to the land. This may result from storm surge, cyclone and tidal wave. For urban floods, it takes place in urban area that lack of proper drainage facilities.

There are many factors that can contribute flood. Rainfall is the most important factor. Variability of rainfall is influenced by many factors such as ENSO (Emerton et al., 2017). Moreover, the characteristic of water catchment such as its size and shape, and land use are also important.

### 5.1.2 Drought

Drought can represent the balance of water supply and water demand. It is a disaster resulting from the lower level of precipitations than normal situation. Usually, drought indices are based on rainfall, soil moisture and temperature. There are variety of drought types such as hydrological drought (deficiency in surface and subsurface water supplies), agricultural drought (deficiency in water availability for crop or plant grown), physiological drought, meteorological drought and socioeconomic drought (failure of water resource systems to meet water demands) (Crocetti et al., 2020). There are various indices that can represent drought event in an area, depending on the aspects.

For this study, the drought index is presented as Standardized Precipitation Index (SPI). The details of SPI can be describing in section 5.2.

### 5.2 Standardized Precipitation Index (SPI)

The Standardized Precipitation Index (SPI) is the most commonly used as an indicator worldwide for detecting and characterizing meteorological droughts. The SPI indicator, which was developed by McKee et al. (1993), and described in detail by Edwards and McKee (1997), measures precipitation anomalies at a given location, based on a comparison of observed total precipitation amounts for an accumulation period of interest (e.g. 1, 3, 12, 48 months), with the long-term historic rainfall record for that period. Note that the name of the indicator is usually modified to include the accumulation period. Thus, SPI-3 and SPI-12, for example, refer to accumulation periods of three and twelve months, respectively.

Since SPI can be calculated over different precipitation accumulation periods (typically ranging from 1 to 48 months), the resulting different SPI indicators allow for estimating different potential impacts of a meteorological drought:

- SPI-1 to SPI-3: When SPI is computed for shorter accumulation periods (e.g., 1 to 3 months), it can be used as an indicator for immediate impacts such as reduced soil moisture, snowpack, and flow in smaller creeks.

- SPI-3 to SPI-12 When SPI is computed for medium accumulation periods (e.g., 3 to 12 months), it can be used as an indicator for reduced stream flow and reservoir storage.
- SPI-12 to SPI-48: When SPI is computed for longer accumulation periods (e.g., 12 to 48 months), it can be used as an indicator for reduced reservoir and groundwater recharge.

Table 5.1 Classification of Standardized Precipitation Index (SPI)  
(McKee et al., 1993).

SPI index values	Categories
2.0 or more	extremely wet
1.5 to 1.99	very wet
1.0 to 1.49	moderately wet
-0.99 to 0.99	near normal
-1.0 to -1.49	moderately dry
-1.5 to -1.99	severely dry
-2.0 and less	extremely dry

The SPI calculation for any location is based on the long-term precipitation record for a desired period. This long-term record is fitted to a probability distribution, which is then transformed into a normal distribution so that the mean SPI for the location and desired period is zero (Edwards & McKee, 1997). Positive SPI values indicate greater than median precipitation and negative values indicate less than median precipitation. Because the SPI is normalized, wetter and drier climates can be represented in the same way; thus, wet periods can also be monitored using the SPI. McKee et al. (1993) used the classification system shown in the SPI value table below (Table 5.1) to define drought intensities resulting from the SPI. They also defined the criteria for a drought event for any of the timescales. A drought event occurs any time

that the SPI is continuously negative and reaches an intensity of -1.0 or less. The event ends when the SPI becomes positive. Each drought event, therefore, has a duration defined by its beginning and end, and an intensity for each month that the event continues. The positive sum of the SPI for all the months within a drought event can be termed the drought's "magnitude".

### 5.3 Calculation of SPI

As SPI is calculating from precipitation, monthly precipitation from each station over Thailand were used to calculate SPI.

In this work, SPI12 was selected as drought index and flood index because it is easily calculated and suitable for study in an annual period. Moreover, some studies also found that the SPI12 index was far more interesting than the longer time scales (SPI24 and SPI48) which showed unreliable results (Dau et al., 2017).

In this study, the 12- month SPI (SPI12) which is a comparison of the precipitation over a specific 12-month period with the long-term precipitation from the same 12-month period was used. The SPI12 index was calculated from the long-term time series of 38 years of CHIRPS rainfall from 1981 to 2018. For calculation, the SPI was determined by dividing the difference between the normalized seasonal rainfall and its long-term seasonal mean for a desired timescale by the standard deviation as shown in Equation 5.1 (McKee et al., 1993).

$$SPI12 = \frac{P_{ij} - P_{im}}{\sigma} \quad (5.1)$$

where SPI12 = Standardized Precipitation Index over a specific 12-month period

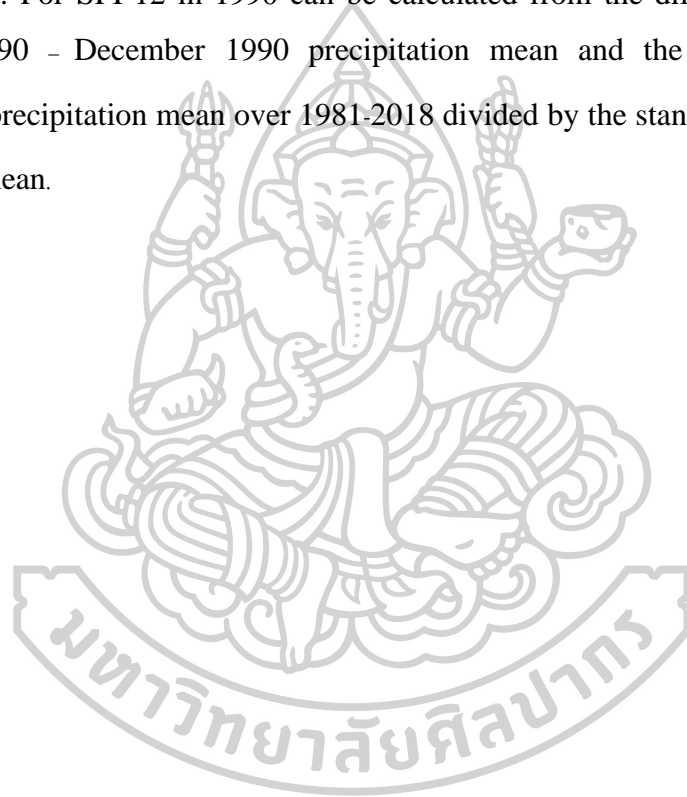
$P_{ij}$  = precipitation mean at station  $i$  over a specific 12-month period for  $j^{\text{th}}$  month

$P_{im}$  = long-term precipitation mean at station  $i$  for a specific 12-month.

$\sigma$  = the standard deviation.

The 12-month SPI provides a comparison of the precipitation over a specific 12-month period with the precipitation totals from the same 12-month period for all the years included in the historical record. In other words, a 12-month SPI at the end of December compares the January–December precipitation total in that particular year with the January–December precipitation totals of all the years on record for that location.

For example, the SPI-12 of 1990 and 2018 as shown in Figures 5.1 and 5.2, respectively. For SPI-12 in 1990 can be calculated from the difference between the January 1990 - December 1990 precipitation mean and the long-term January–December precipitation mean over 1981-2018 divided by the standard deviation of the long-term mean.





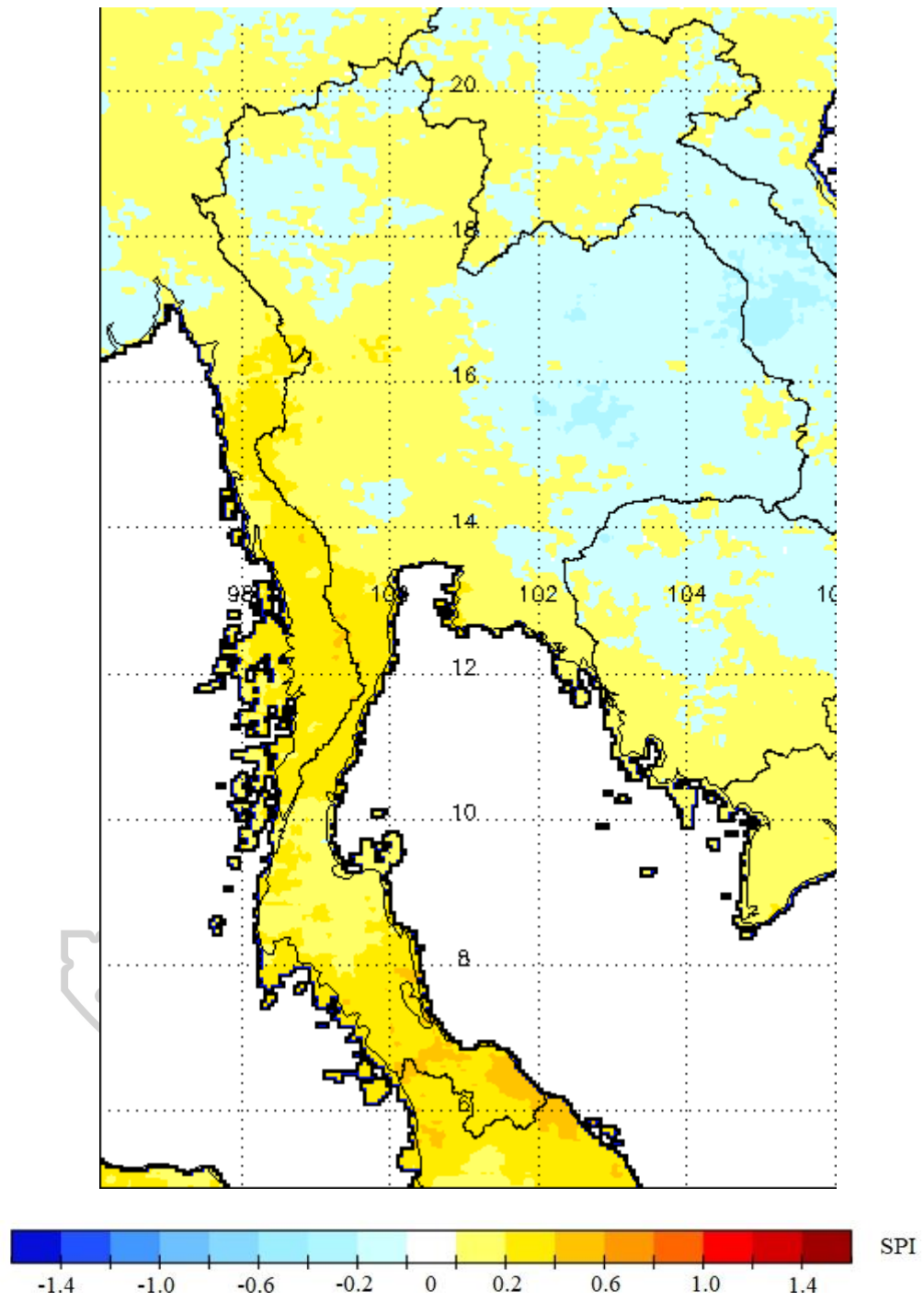


Figure 5.1 SPI over Thailand in 1990.

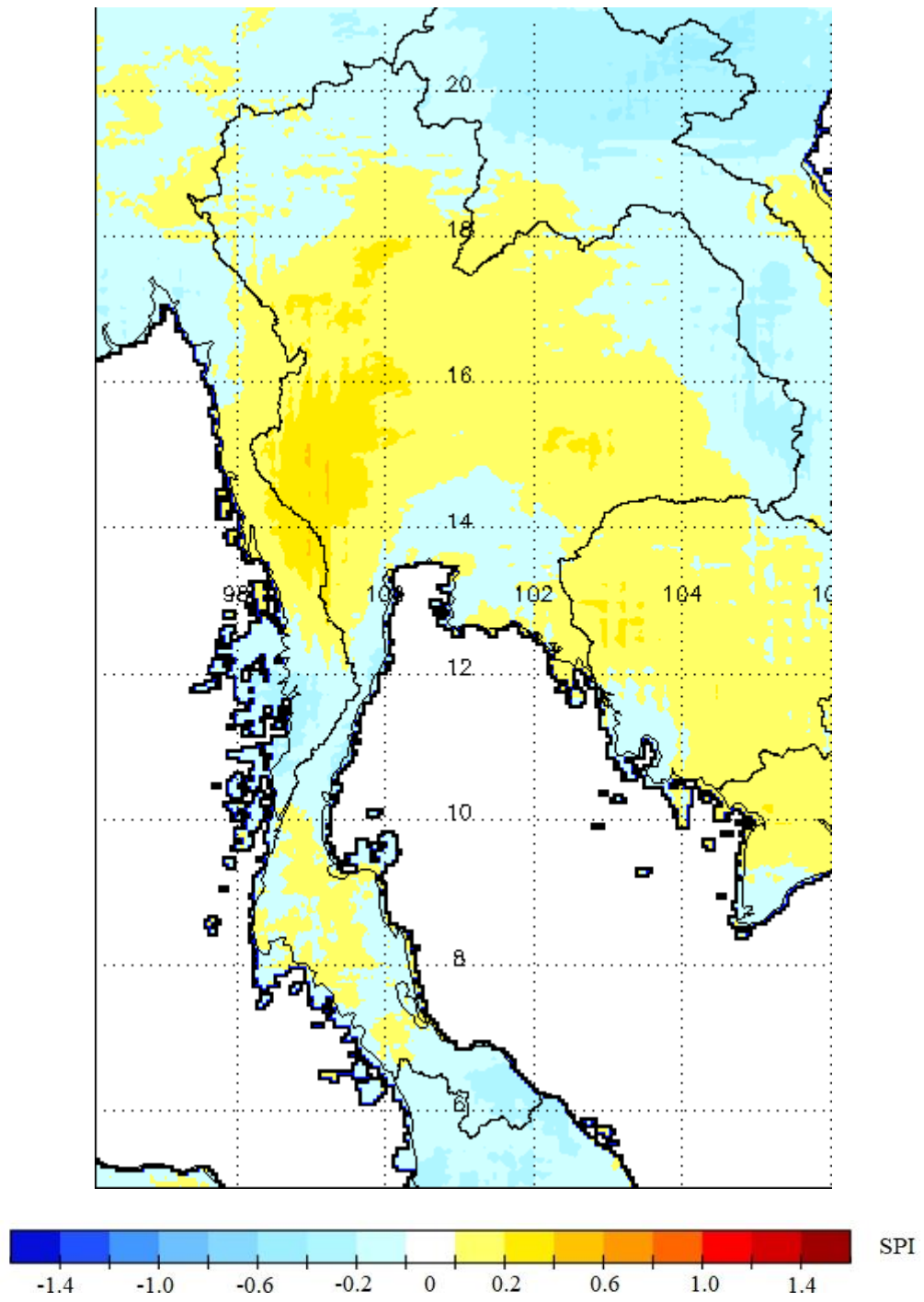


Figure 5.2 SPI over Thailand in 2018.

## 5.4 The indices of the expansion

The index of the expansion in the GMS used in this study is the minimum of high cloud cover, implying the edge of the Hadley cell. The index of the climate in Thailand employed in this investigation is the SPI.

## 5.5 Method

To investigate the effect of the expansion on the climate in Thailand, the time series of the expansion index and the time series of the SPI of each main region of Thailand and the whole country were plotted in the same graphs.

## 5.6 Results and Discussion

The time series graphs for each region are shown in Figures 5.3-5.6 and the graph for the whole country is shown in Figure 5.7.

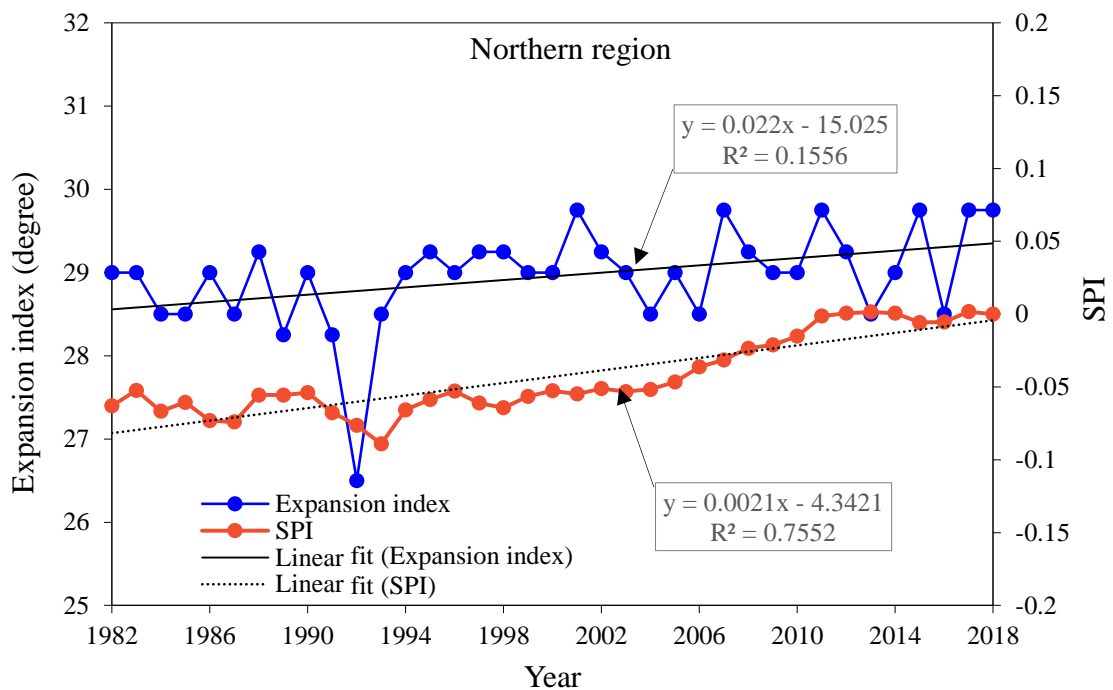


Figure 5.3 Time series of the expansion index and time series of the SPI together with the linear fits of both time series for the northern region.

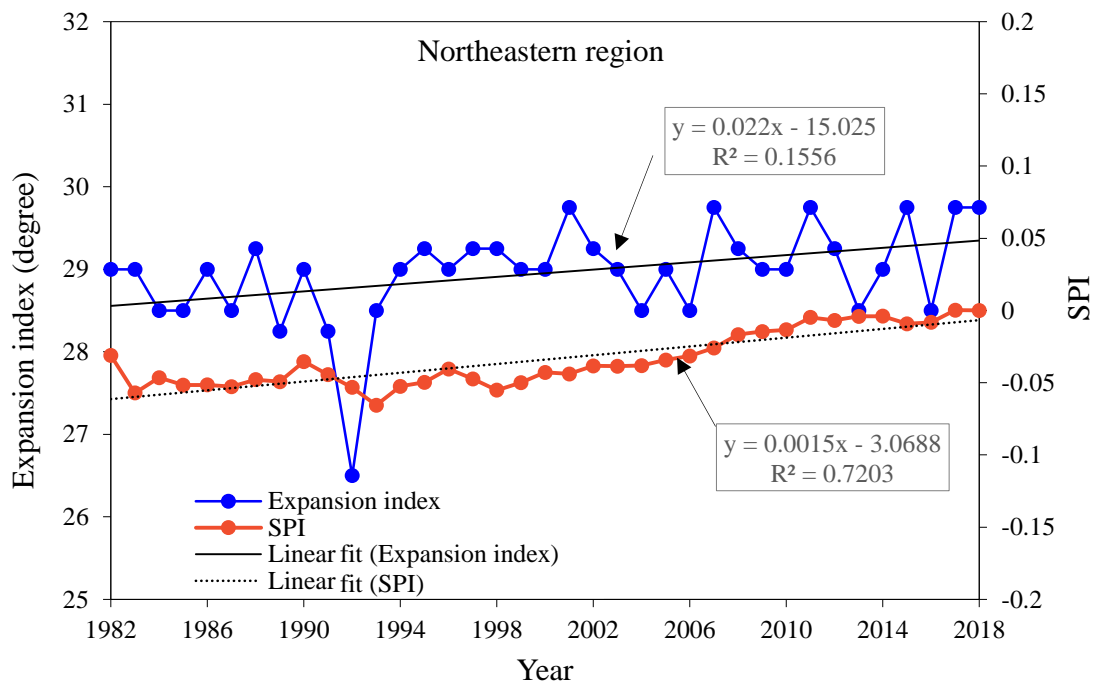


Figure 5.4 Time series of the expansion index and time series of the SPI together with the linear fits of both time series for the northeastern region.

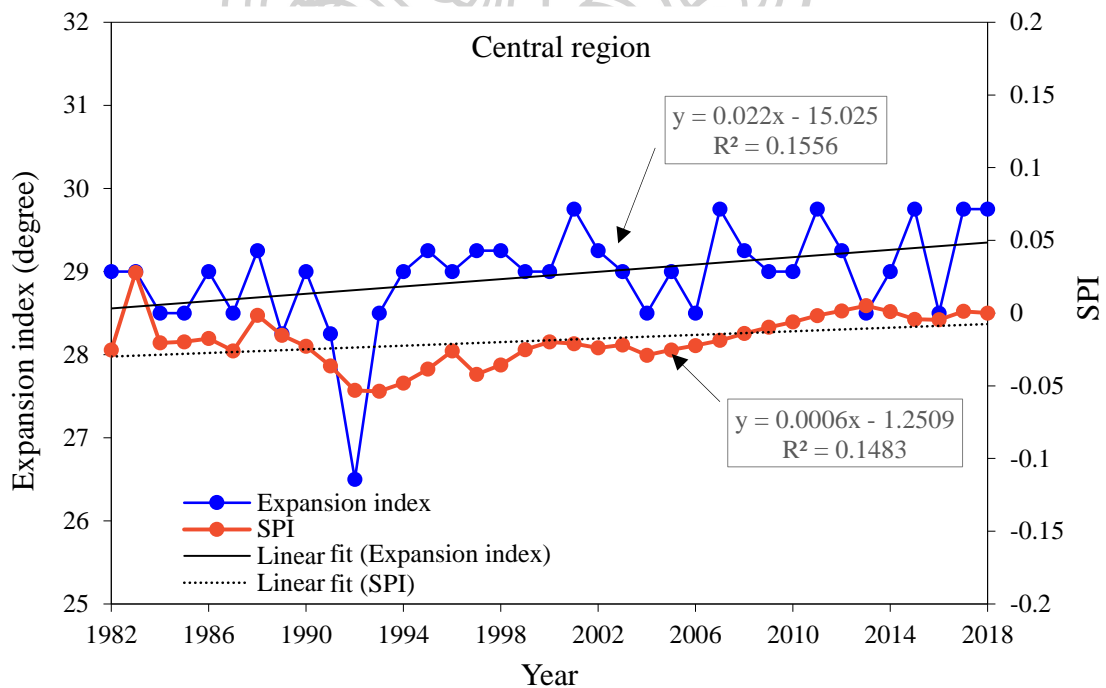


Figure 5.5 Time series of the expansion index and time series of the SPI together with the linear fits of both time series for the central region.

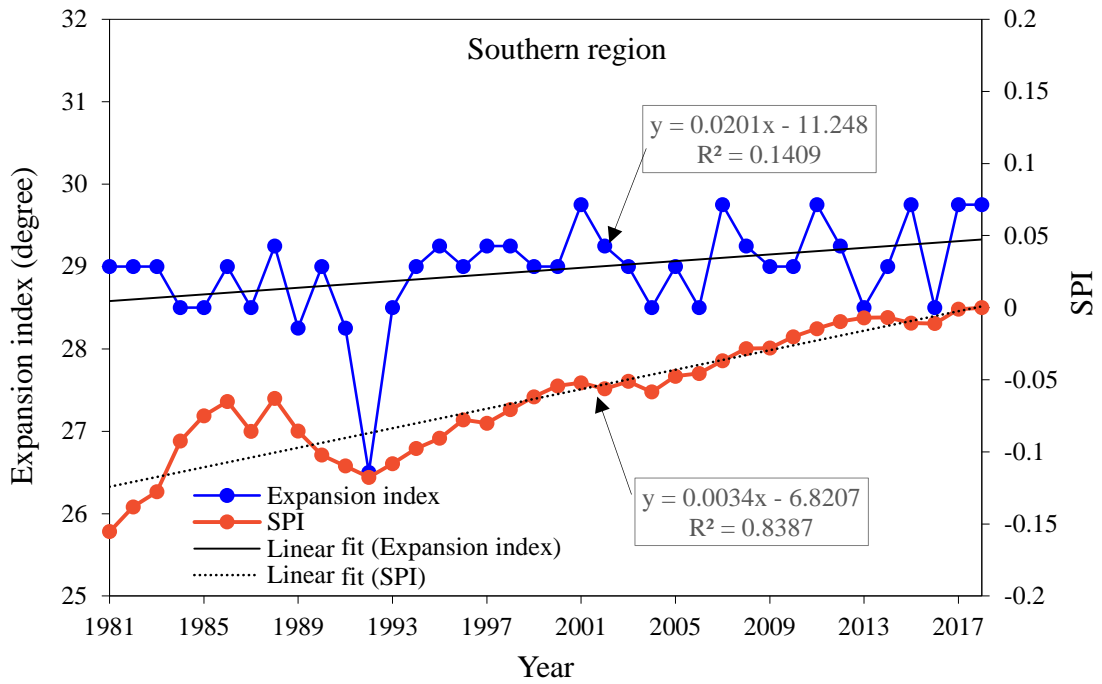


Figure 5.6 Time series of the expansion index and time series of the SPI together with the linear fits of both time series for the southern region.

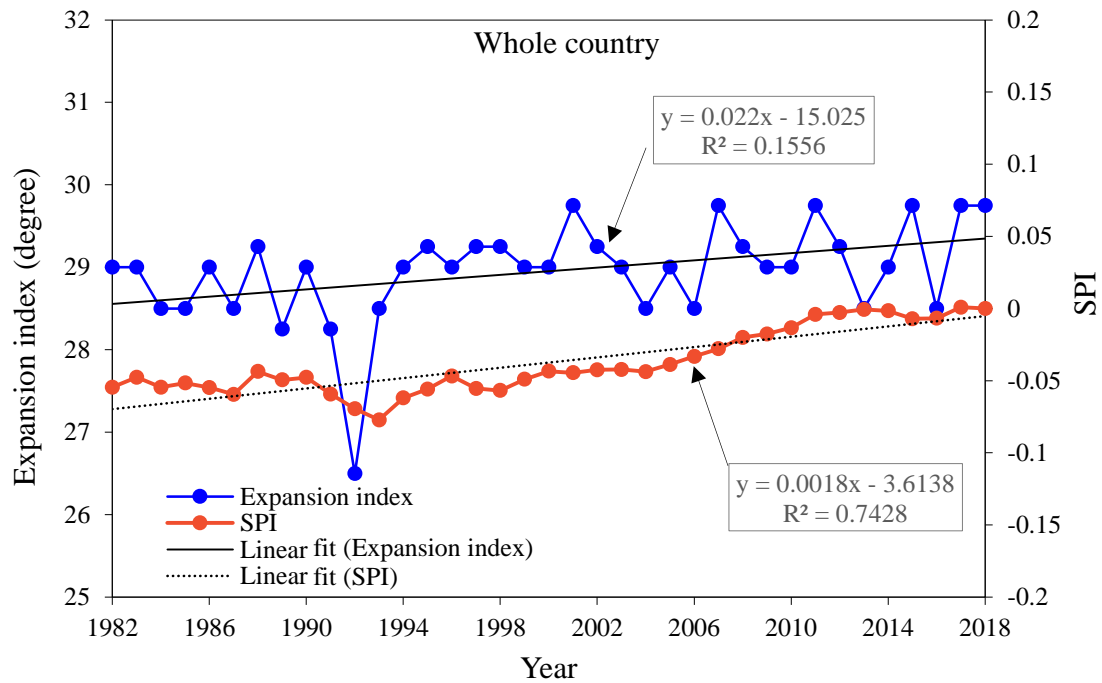


Figure 5.7 Time series of the expansion index and time series of the SPI together with the linear fits of both time series for the whole country

The correlation coefficients between the index of the expansion and SPI, and related statistics are shown in Table 5.2.

Table 5.2 Correlation between the index of the expansion and SPI.

Region	Correlation coefficient (r)	t-statistic	p-value
Whole Thailand	0.44	<b>2.96</b>	<b>0.0054</b>
Northern region	0.41	<b>2.67</b>	<b>0.0114</b>
Northeastern region	0.38	<b>2.49</b>	<b>0.0176</b>
Central region	0.33	<b>2.11</b>	<b>0.0421</b>
Southern region	0.43	<b>2.86</b>	<b>0.0071</b>

\* The significant at  $p < 0.05$  are highlighted in bold.

From Figure 5.3-5.7, it is found that for each region the expansion index increases with the increase of SPI and the result for the whole country is similar to that of each region. From Table 5.2, there exists the correlation between the expansion index and SPI for each region and for the whole country. This may be explained as follows:

The expansion creates more convection in the equatorial zone (Chanalert et al., 2022). This convection may cause more rain. From the analysis results, it is clearly seen that more rain is visible in the southern region as this region is situated near the equator. Thailand's Department of Meteorology reported that the annual average precipitation in the country had increasing trend during 1981-2007 (Marks, 2011). In addition, for the entire country, the rain tend to increase as the expansion increases.

## 5.7 Conclusion

In this work, the drought and flood indices are presented as SPI. The SPI over Thailand is calculated from the precipitation data set over the period of 1981-2018. We used the minimum  $C_H$  to indicate the tropical expansion in the GMS region. Then we

estimated the correlation between SPI average and tropical expansion index in Thailand. In addition, we also estimated the correlation for each region of Thailand. The results show that the tropical expansion increases with the increase of SPI in all regions of Thailand. This may be explained that the expansion creates more convection in the equatorial zone which may cause more rain in all main regions of Thailand.



## Chapter 6

### Conclusion

This study investigates the tropical expansion by exploring the variability of the Hadley cell mainly on regional basis. This study comprises three parts, namely 1) The Greater Mekong Subregion (GMS) and Tropical Expansion: A Regional Study of Convection and Precipitation 2) An investigation of poleward expansion of the Hadley circulation using high cloud cover 3) Effects of tropical expansion on climate in Thailand. This can be summarized as follows:

1) The poleward expansion in the GMS region is estimated by the zonal average of  $T_B$  from HIRS-UTWV and ERA-Interim. The three indices revealed the latitude movement, which detected the expansion during the boreal winter. There is a significant poleward movement of the three indices in the range of  $0.450^\circ - 1.327^\circ$  per decade. There is no evidence of poleward movement during the summer monsoon period.

2) This study investigated the poleward shift of the Hadley cell over the globe using high cloud cover from ERA-Interim reanalysis. The result shows that the Hadley circulation is poleward expanded in both hemispheres. In addition, we found that the poleward shift of the edge of the Hadley cells occurs in all four seasons in the northern hemisphere. In the southern hemisphere, we found that there are poleward shifts of the Hadley cell in all seasons except in summer.

3) In this work, the effect of the tropical expansion on climate in Thailand was investigated. The SPI has indicated the feature of the climate (flood or drought) of the regions. We estimated the correlation between the tropical edge index and SPI average for each main region of Thailand and the whole country. The result shows that the expansion increase as SPI is increased in all regions of the country. This may be due to the fact that the expansion induces more convection in the equatorial zone which causes more rain in Thailand region.



## Appendix 1

### Mapping solar irradiation from ground- and satellite-based data over Thailand using a simple semi-empirical model<sup>3</sup>

Solar irradiation may increase the surface temperature, high cloud and moist air, and these may influence the Hadley circulation. Therefore, this part of the study aims to present a new method to calculate solar irradiation over a broad area. The details of this approach are presented as follows.

#### 1 Introduction

The geographical distribution of global solar irradiation is essential for solar energy applications (Duffie & Beckman, 2013). Specifically, solar irradiation is a source of solar energy systems. Solar irradiation is also important for atmospheric research (Salby, 1996) because solar radiation supplies energy to the atmospheric system. A classical approach to obtain such information on solar irradiation is to establish a dense network of pyranometers in an area of interest and continuously measure incident solar irradiation for several years. Then, the average irradiation obtained from the network is presented on a geographical map of the area, and the contour lines of solar irradiation are traced on that map to show the geographical distribution of the solar irradiation of that area (Suwantragul, 1984). Although, networks of pyranometers have been established in many areas of the world, the density of pyranometers in most areas, especially in developing countries, is still low (Janjai, 2007, 2009). The use of the measurement approach is generally simple but its performance depends strongly on the density of the pyranometer network. As meteorological satellites can detect clouds over large areas and clouds are a main factor affecting surface solar irradiation, a number of researchers have proposed methods for deriving surface solar irradiation from the imagery data of meteorological satellites

---

<sup>3</sup> This work has been accepted for publication in Science, Engineering and Health Studies.

(Cano et al., 1986; Exell, 2017; Huang et al., 2019; Möser & Raschke, 1984; Pinker & Laszlo, 1992; Polo, 2015; Polo et al., 2011; Wyser et al., 2002). The satellite approach consists of several techniques. These techniques can be broadly categorized as techniques using physical models and techniques employing statistical or empirical models. The physical model has an advantage in terms of generality, but it is relatively complicated and requires input data, which are not always available. The empirical model is generally simple, but it usually lacks generality. For the case of Thailand, the mapping of surface solar irradiation has been performed using various techniques (Exell, 2017; Janjai et al., 2005; Janjai et al., 2013; Sorapipatana et al., 1988; Suwantragul, 1984). These techniques include those based on measurements and those that use physical models. Each technique has advantages and disadvantages as mentioned above. In this work, we propose to map solar irradiation with ground- and satellite-based data over Thailand by using a simple semi-empirical model.

## 2 Materials and Methods

### 2.1 Materials

The materials used in this work are satellite and ground-based data. The details of these data are described as follows.

#### 2.1.1 Satellite data

The satellite data used in this approach were hourly imagery visible data from the MTSAT-1R satellite encompassing the period of 1 January, 2006–31 December, 2015. For each day, the hourly satellite data from 8:30 to 16:30 local time were used. The data were processed using the same method as that in our previous work (Janjai et al., 2013). The information in each satellite pixel is the earth-atmospheric reflectivity ( $\rho_{EA}$ ). Then this information is converted into cloud index ( $n$ ) using a relation given by Cano et al. (1986) as

$$n = \frac{\rho_{EA} - \rho_G}{\rho_c - \rho_G} \quad (1)$$

where  $\rho_G$  and  $\rho_c$  are the surface reflectivity and maximum cloud reflectivity, respectively.

As ozone absorbs solar irradiation and the amount of ozone from ground-based measurement is rarely available, the information on the amount of ozone obtained from the OMI/AURA satellite for the period of 2006 - 2015 was also acquired (<http://avdc.gsfc.nasa.gov/pub/data/satellite/Aura/OMI/V03/L2OVP/>) for this work.

### 2.1.2 Ground-based data

Data on global solar irradiation data are essential for the formulation of the proposed semi-empirical model proposed here. In this work, the global solar irradiation measured at the following solar monitoring stations were collected: Chiang Mai station (18.78° N, 98.98° E) located in the northern region of Thailand, Ubon Ratchathani station (15.25° N, 104.87° E) situated in the Thai northeastern region, Nakhon Pathom station (13.82° N, 100.04° E) located in the Thai central region and Songkhla station (7.20° N, 100.06° E) situated in the southern region of the country (see Figure 1). The data from these stations covering the 10-year period (2006-2015) were used to formulate the semi-empirical model. The globe solar irradiation measured at 36 stations of the Department of Alternative Energy Development and Efficiency (DEDE) of Thailand for a period of 1-5 years was also collected to validate the model. The positions of these DEDE stations are also shown in Figure 1.

Water vapor absorbs a considerable amount of solar radiation (Iqbal, 1983; Kämpfer, 2013). In this study, precipitable water ( $w$ ) was used to quantify water vapor, and  $w$  was estimated from ambient air temperature ( $T_a$ ) and ambient relative humidity ( $rh_a$ ) using the following formula proposed by Janjai et al. (2005):

$$w = 0.8933 \exp \left( 0.1715 \frac{rh_a p_s}{T_a} \right) \quad (2)$$

where  $w$  is the precipitable water (cm),  $T_a$  is the temperature of ambient air (K),  $rh_a$  is the relative humidity of ambient air (decimal), and  $p_s$  is the saturated water vapor (mbar). The data of  $T_a$  and  $rh_a$  measured at 80 meteorological stations were collected to

estimate  $w$ . The gaps between stations were filled out using the interpolation approach (Press et al., 1992).

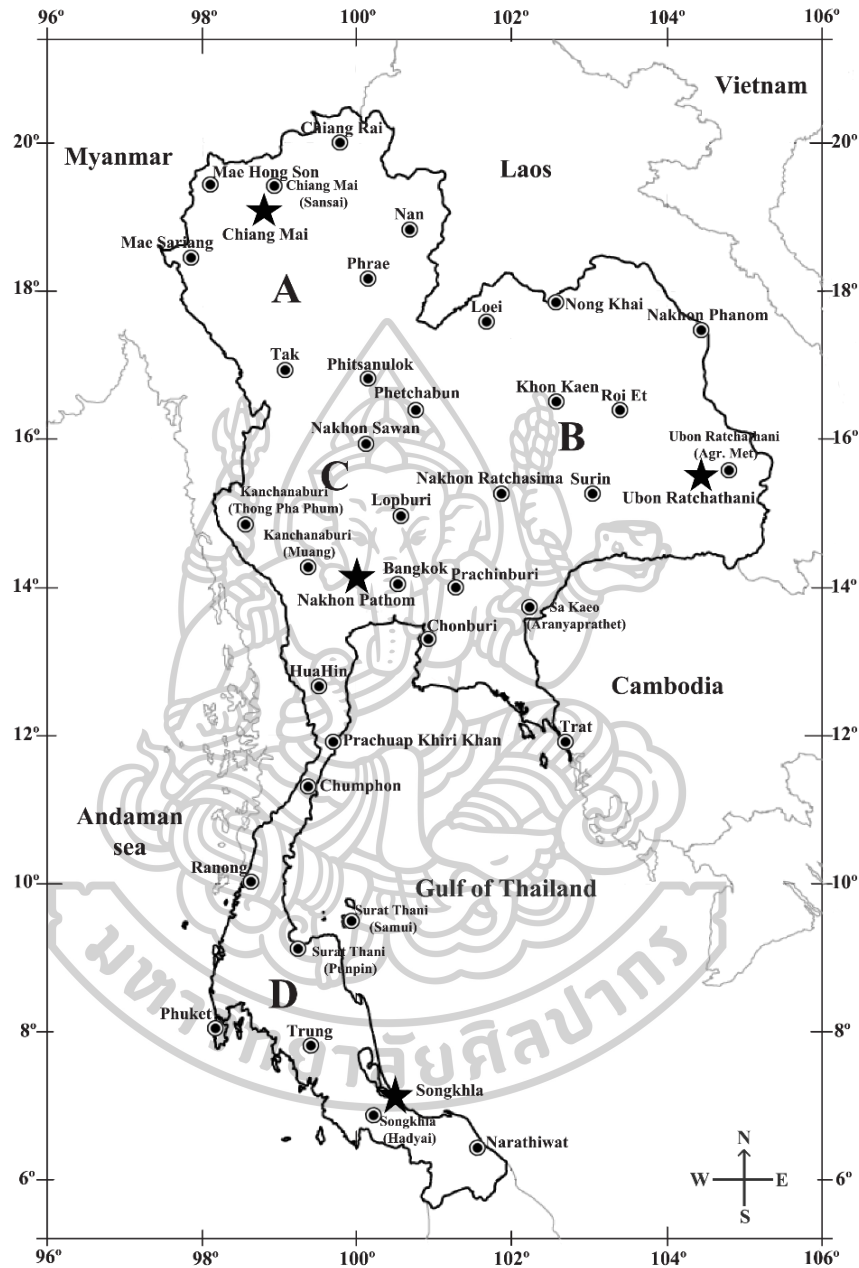


Figure 1 Map of Thailand showing the position of the solar monitoring stations (★) whose data were used to determine the model coefficients and the position of the DEDE stations (⊙) whose data were employed for model validation. (A, B, C and D indicate the northern, northeastern, central, and the southern regions, respectively)

In this study, the influence of atmospheric aerosols was quantified using the visibility data measured at 80 stations in Thailand, and the interpolation approach (Press et al., 1992) was employed to fill out gaps in the measurement.

## 2.2 Methods

The procedures for developing the method are as follows.

### 2.2.1 Modeling

Instead of developing a physical model or an empirical model, a semi-empirical model was proposed for calculating solar irradiation. In general, solar irradiation depends on cloud, water vapor, ozone, and aerosol (Iqbal, 1983). To investigate this dependence, this study plotted the normalized monthly average daily values of cloud index ( $\frac{\bar{n}}{\bar{n}_{\max}}$ ), precipitable water ( $\frac{\bar{W}}{\bar{W}_{\max}}$ ), total ozone column ( $\frac{\bar{O}_3}{\bar{O}_{3\max}}$ ), and visibility ( $\frac{\bar{VIS}}{\bar{VIS}_{\max}}$ ) from the four stations for the period of 2006–2015 against the normalized monthly average of daily solar irradiation ( $\frac{\bar{H}}{\bar{H}_0}$ ).  $\bar{H}$  is the monthly average of daily global solar irradiation,  $\bar{H}_0$  is the monthly average of daily extraterrestrial solar irradiation,  $\bar{VIS}$  is the monthly average of daily visibility,  $\bar{VIS}_{\max}$  is the maximum monthly average of daily visibility,  $\bar{W}$  is the monthly average of daily precipitable water,  $\bar{W}_{\max}$  is the maximum monthly average of daily precipitable water,  $\bar{O}_3$  is the monthly average of daily total ozone column,  $\bar{O}_{3\max}$  is the maximum monthly average of daily total ozone column,  $\bar{n}$  is the monthly average of daily cloud index, and  $\bar{n}_{\max}$  is the maximum monthly average of daily cloud index. Figure 2 reveals the results.

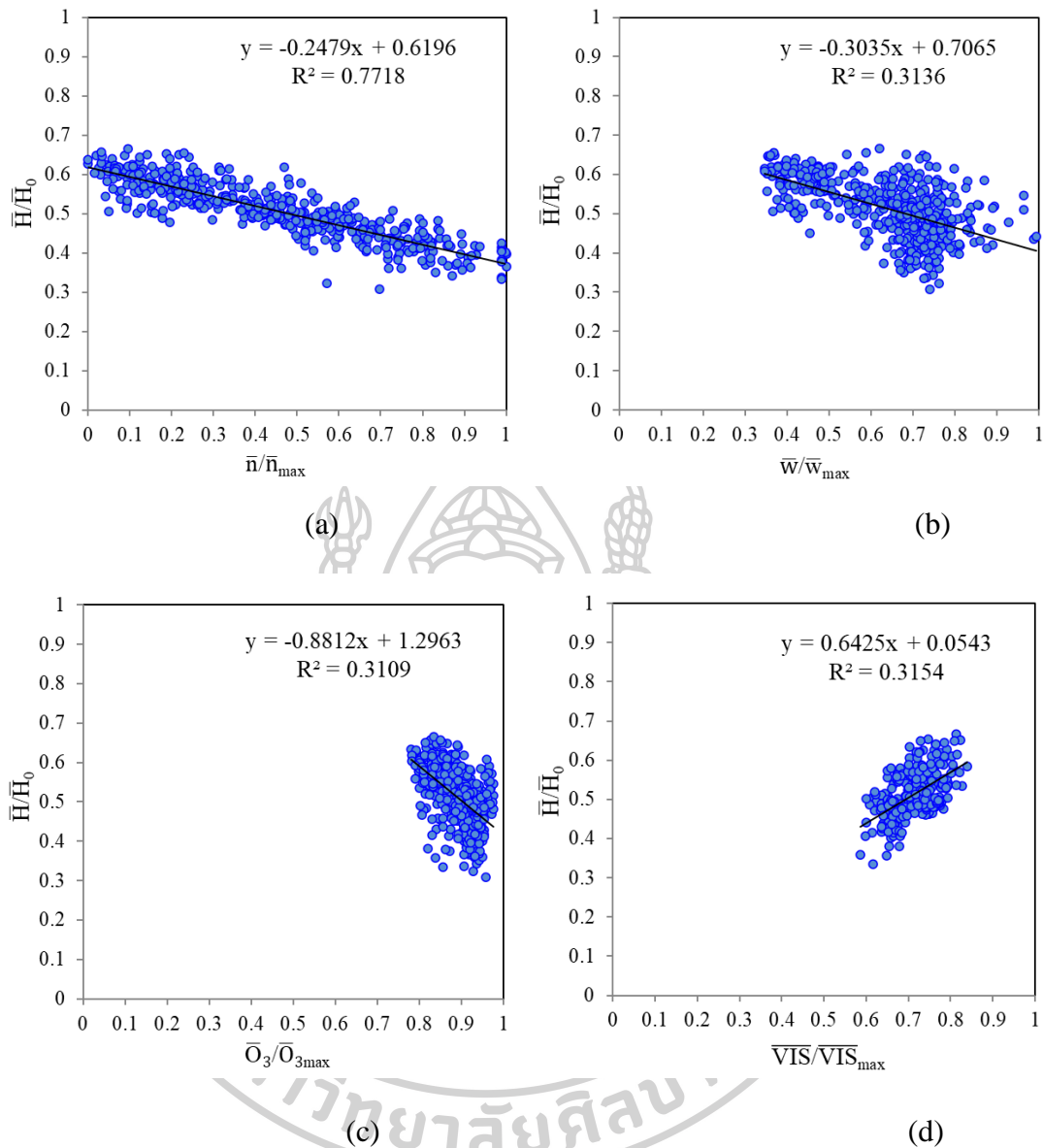


Figure 2 Dependence of normalized monthly average of daily global solar irradiation ( $\frac{\bar{H}}{\bar{H}_0}$ ) on the amount of various atmospheric constituents: a) normalized cloud index ( $\frac{\bar{n}}{\bar{n}_{\max}}$ ), b) normalized precipitable water ( $\frac{\bar{W}}{\bar{W}_{\max}}$ ), c) normalized visibility ( $\frac{\bar{VIS}}{\bar{VIS}_{\max}}$ ), and d) normalized total ozone column ( $\frac{\bar{O}_3}{\bar{O}_{3\max}}$ ).

$R$  is the correlation coefficient. It indicates the degree of correlation between the variable in the vertical axis and the variable in the horizontal axis. Ideally,  $R$  should be 1 or -1. From Figure 2, the values of  $R$  in many cases are relatively low. Take for

example the case of ozone: the parameters in the correlation between the dependent variable  $\frac{\bar{H}}{\bar{H}_0}$  and  $\frac{\bar{O}_3}{\bar{O}_{3\max}}$ , exert certain influences, additionally there are influences from other dependent variables in the graph, thus making the correlation coefficient low. In addition, we cannot isolate these influences for the all-sky condition because the information on the solar spectrum under the all-sky conditions is not available.

From Figure 2, we also notice that the normalized values of the cloud index, precipitable water, total ozone column, and visibility linearly affect the normalized value of the monthly average of daily solar irradiation. Therefore, we proposed the following model:

$$\frac{\bar{H}}{\bar{H}_0} = a_0 + a_1 \frac{\bar{VIS}}{\bar{VIS}_{\max}} + a_2 \frac{\bar{W}}{\bar{W}_{\max}} + a_3 \frac{\bar{O}_3}{\bar{O}_{3\max}} + a_4 \frac{\bar{n}}{\bar{n}_{\max}} \quad (3)$$

where  $\bar{H}$  is the monthly average of daily global solar irradiation,  $\bar{H}_0$  is the monthly average of daily extraterrestrial solar irradiation,  $\bar{VIS}$  is the monthly average of daily visibility,  $\bar{VIS}_{\max}$  is the maximum monthly average of daily visibility,  $\bar{W}$  is the monthly average of daily precipitable water,  $\bar{W}_{\max}$  is the maximum monthly average of daily precipitable water,  $\bar{O}_3$  is the monthly average of daily total ozone column,  $\bar{O}_{3\max}$  is the maximum monthly average of daily total ozone column,  $\bar{n}$  is the monthly average of daily cloud index, and  $\bar{n}_{\max}$  is the maximum monthly average of daily cloud index.  $a_0$ ,  $a_1$ ,  $a_2$ ,  $a_3$ , and  $a_4$  are the empirical coefficients of the model.

Equation (3) was fitted with solar irradiation and the related data at the four solar monitoring stations, encompassing a 10-year period (2006–2015) to obtain the

coefficients of the model.  $\bar{H}_0$  was calculated using a formula given by Iqbal (1983). The coefficients and statistical parameters obtained from the statistical analysis are presented in Table 1.

Table 1 Values of model coefficients and statistical parameters. (R is the correlation coefficient, and N is the total amount of data).

Coefficient	Value of coefficient	t-statistic	p-value	R <sup>2</sup>	N
$a_0$	0.7425	20.8147	<0.05	0.79	480
$a_1$	0.0511	2.4155	<0.05		
$a_2$	0.0681	3.9264	<0.05		
$a_3$	-0.2241	-5.1937	<0.05		
$a_4$	-0.2545	-29.9436	<0.05		

A p-value is a value of a probability to accept or reject the null-hypothesis. It has values of 0-1. Small p-values are taken as stronger evidence against the null-hypothesis. We setup the p-value for accepting or rejecting the hypothesis (Freedman et al., 2018).

The t-statistic can be used to demonstrate goodness of fit. It is usually determined from statistical tables or may be given as a standard output in a statistical program. For a two-tail distribution with a sample number of over 100, a t-statistic of 2.0 is related to a p-value of 0.05, which denotes a 5% probability that the relationship occurs by chance. A higher absolute value of a t-statistic with the same number of samples relates to a low probability that the relationship occurs by chance (Freedmann et al., 2018).



$R^2$  is commonly called the coefficient of determination. It is the proportion of variance in the dependence variable that can be explained by the independent variables (Dhakal, 2018).

Table 1 shows that the value of  $R^2$  is relatively high and the absolute values of the t-statistic associated with  $a_1$ ,  $a_2$ ,  $a_3$ , and  $a_4$  are greater than 2 with very low p-value, meaning that  $\frac{\bar{n}}{\bar{n}_{\max}}$ ,  $\frac{\bar{W}}{\bar{W}_{\max}}$ ,  $\frac{\bar{O}_3}{\bar{O}_{3\max}}$ , and  $\frac{\bar{VIS}}{\bar{VIS}_{\max}}$  are statistically significant predictors of  $\frac{\bar{H}}{\bar{H}_0}$ .

### 2.2.2 Evaluation of model performance

To evaluate the model performance, we employed the model in computing the solar irradiation at 36 solar monitoring stations of DEDE (Figure 1). The results are compared with those obtained from the measurement (Figure 3 and Table 2).

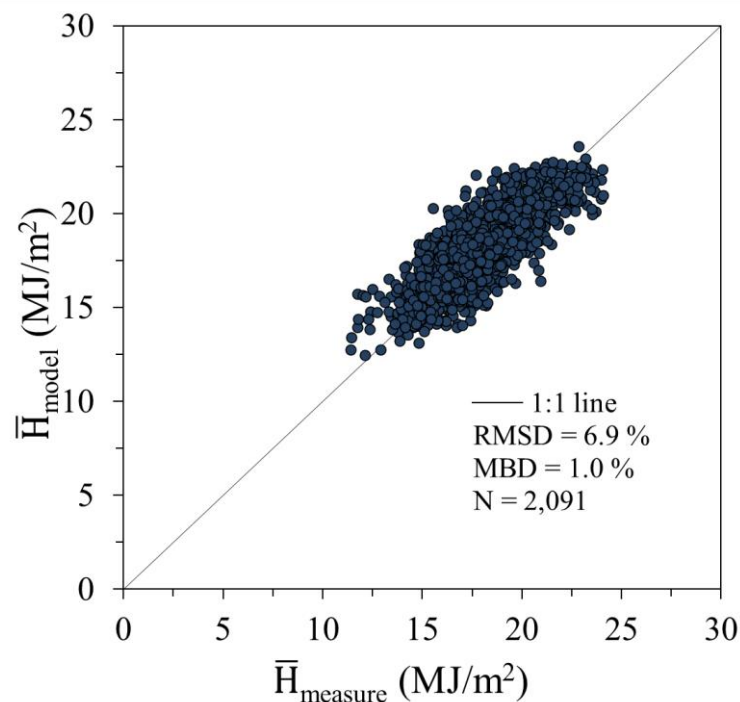


Figure 3 Comparison between monthly average of daily global solar irradiation calculated from the model ( $\bar{H}_{\text{model}}$ ) and that obtained from the measurements ( $\bar{H}_{\text{measure}}$ ).

The results from Figure 3 indicate that  $\bar{H}_{\text{model}}$  agrees well with  $\bar{H}_{\text{measure}}$ , with the discrepancy reflected the root mean square difference (RMSD) relative to the mean measured irradiation of 6.9% and the mean bias difference (MBD) relative to the mean measured irradiation of 1.0%. Janjai et al. (2013) used a physical model to calculate solar radiation. They found that the solar radiation calculated from the model and that obtained from the measurement had an RMSD of 5.3% and MBD of 0.3%. Bosch et al. (2010) used Heliosat-2 together with a digital terrain model to calculate the solar radiation over an area in Spain and found that the solar radiation calculated from the model and that from the measurement were in acceptable agreement, with the RMSD being 10% and the MBD being 2%. Polo et al. (2011) employed a satellite approach to estimate the solar radiation over India and found that the solar radiation calculated from the satellite and that from measurements are in reasonable agreement, with the RMSD being around 12% and the MBD being around of 5%. Polo (2015) used a satellite approach to derive solar irradiation over Spain and found that the comparison between satellite-derived global solar irradiation and that from the measurements had the RMSD of 11%. Therefore, the accuracy of the proposed model is comparable to that in published works.

### 2.2.3 Mapping

In mapping the monthly average of daily irradiation over Thailand, the values of all model parameters encompassing the whole areas of the country must be obtained. As precipitable water ( $w$ ) is calculated from the temperature ( $T_a$ ) and relative humidity ( $rh_a$ ) of the air, the values of  $T_a$  and  $rh_a$  measured at the 80 meteorological stations were interpolated to obtain their values at the position corresponding to the pixels of the MTSAT-1R. In addition, the interpolated values of  $T_a$  and  $rh_a$  were employed to calculate  $w$ . A similar approach was used to estimate visibility. Finally, the values of  $w$ , VIS,  $O_3$ , and  $n$  were used to calculate solar irradiation using the model (Equation (3)). The outcomes were displayed as solar irradiation maps (Figures 4 and 5).

Table 2 Names, latitudes, longitudes, altitudes of DEDE measurement stations whose data are used for validating the model. Also shown in this table are the data period and the values of root mean square different (RMSD) and mean bias different (MBD) obtained from the comparison between the model and measured monthly average daily irradiances.

No.	Station	Latitude (Degree)	Longitude (Degree)	Altitude (m)	Period of data	RMSD (%)	MBD (%)
1	Chiang Rai	20.08	99.88	495	Oct, 2012-Dec, 2015	8.8	5.0
2	Mae Hong Son	19.43	97.96	730	Jan, 2011-Dec, 2015	11.7	7.2
3	Nan	18.72	100.75	459	Jan, 2011-Dec, 2015	7.3	3.9
4	Chiang Mai (Sansai)	18.83	98.88	565	Jan, 2011-Dec, 2015	7.9	3.5
5	Mae Sa Rieng	18.17	97.93	698	Jan, 2011-Dec, 2015	8.0	5.0
6	Phrae	18.06	100.06	390	Jan, 2011-Dec, 2015	5.4	-1.0
7	Tak	16.80	98.90	562	Jan, 2011-Dec, 2015	7.9	-0.3
8	Loei	17.40	101.00	492	Jan, 2011-Dec, 2015	6.1	2.0
9	Nong Khai	17.87	102.72	177	Jan, 2011-Dec, 2015	5.0	-2.1
10	Khon Kaen	16.45	102.78	179	Jan, 2011-Dec, 2015	6.2	-1.7
11	Nakhon Panom	16.97	104.73	184	Jan, 2011-Dec, 2015	7.3	0.0
12	Surin	14.88	103.50	162	Jan, 2011-Dec, 2015	7.4	0.2
13	Ubon Ratchathani (Agr. Met)	15.28	105.14	160	Jan, 2011-Dec, 2015	5.3	0.2
14	Nakhon Ratchasima	14.97	102.08	218	Jan, 2011-Dec, 2015	6.3	2.3
15	Roi Et	16.07	103.00	153	Jan, 2011-Dec, 2015	5.2	-0.7
16	Phitsanulok	16.78	100.27	137	Jan, 2011-Dec, 2015	6.2	3.1
17	Phetchabun	16.43	101.15	250	Jan, 2011-Dec, 2015	4.8	2.2
18	Nakhon Sawan	15.67	100.12	50	Jan, 2011-Dec, 2015	4.5	2.5
19	Lop Buri	14.83	100.62	54	Jan, 2011-Dec, 2015	6.7	1.1
20	Bangkok	13.75	100.52	2	Jan, 2011-Dec, 2015	8.5	4.9
21	Kanchanaburi (Muang)	14.02	99.53	159	Jan, 2011-Dec, 2015	5.1	-0.9
22	Kanchanaburi (Thong Pha Phum)	14.73	98.63	345	Jan, 2011-Dec, 2015	7.5	2.4
23	Sa Kaeo (Aranyaprathet)	13.70	102.00	62	Jan, 2011-Dec, 2015	5.5	2.7
24	Trat	11.77	102.88	68	Jan, 2011-Dec, 2015	8.8	-3.0
25	Prachin Buri	13.97	101.70	46	Jan, 2011-Dec, 2015	5.0	1.3
26	Chon Buri	13.37	100.97	5	Jan, 2011-Dec, 2015	6.7	0.5
27	Prachuap Khiri Khan	11.83	99.83	1	Jan, 2011-Dec, 2015	6.3	-3.3
28	Hua Hin	12.59	99.73	107	Jan, 2015-Dec, 2015	3.2	0.8
29	Chumphon	10.40	99.18	8	Jan, 2011-Dec, 2015	7.4	2.4
30	Ranong	9.98	98.62	34	Jan, 2011-Dec, 2015	7.4	-0.2
31	Surat Thani (Samui)	9.47	100.05	1	Jan, 2011-Dec, 2015	7.7	-4.6
32	Surat Thani (Punpin)	9.13	99.15	10	Jan, 2011-Dec, 2015	6.5	1.5
33	Phuket	8.13	98.30	26	Jan, 2011-Dec, 2015	6.2	-3.8
34	Trang	7.52	99.62	55	Jan, 2011-Dec, 2015	8.4	0.6
35	Songkhla (Hadyai)	6.92	100.43	53	Jan, 2011-Dec, 2015	6.9	3.5
36	Narathiwat	6.40	101.82	8	Jan, 2011-Dec, 2015	6.7	1.7
	Combined data					6.9	1.0

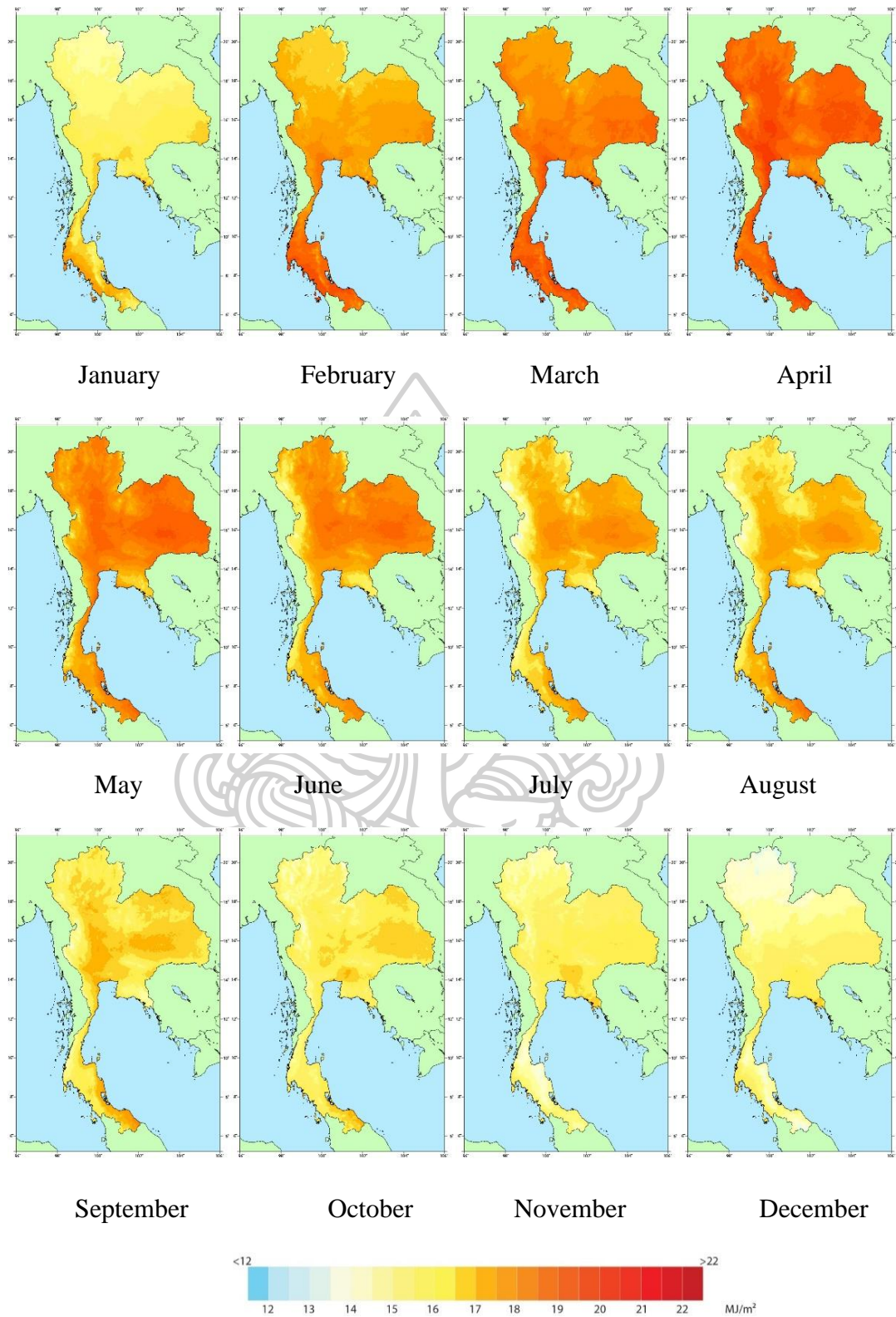
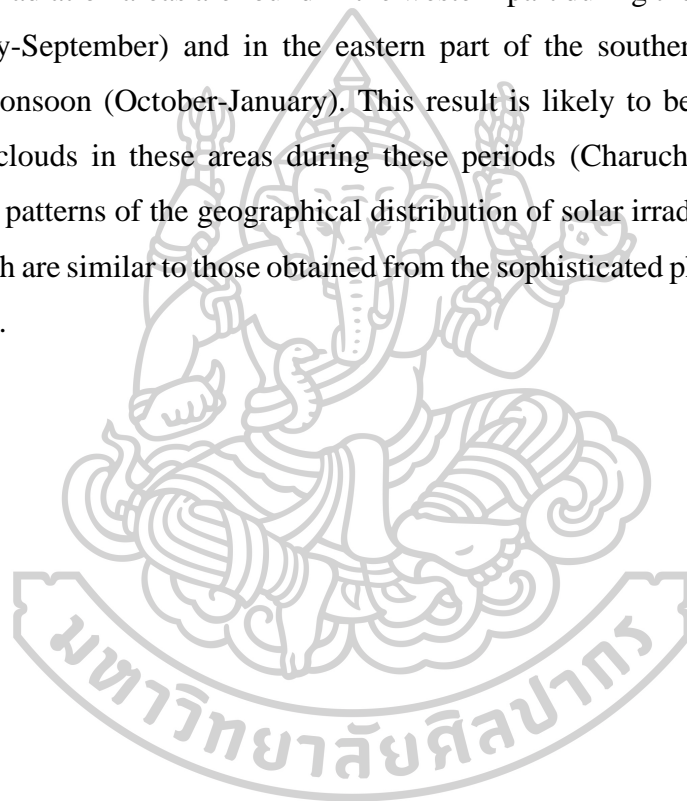


Figure 4 Monthly solar irradiation map of Thailand.

### 3 Results and Discussion

The monthly irradiation maps (Figure 4) show that the solar irradiation at most of the locations around the country gradually increases from January, peaks in April, and then gradually decreases toward the end of the year. In the yearly irradiation map (Figure 5), the areas with the highest irradiation are observed to be situated in the lower part of the northeastern region and some areas in the central region. Solar irradiation is relatively low in the mountain ranges in the north and in the western parts of Thailand. Low solar irradiation areas are found in the western part during the southwest monsoon period (May-September) and in the eastern part of the southern region during the northeast monsoon (October-January). This result is likely to be caused by the high amount of clouds in these areas during these periods (Charuchittipan et al., 2018). Overall, the patterns of the geographical distribution of solar irradiation obtained from this approach are similar to those obtained from the sophisticated physical model (Janjai et al., 2013).



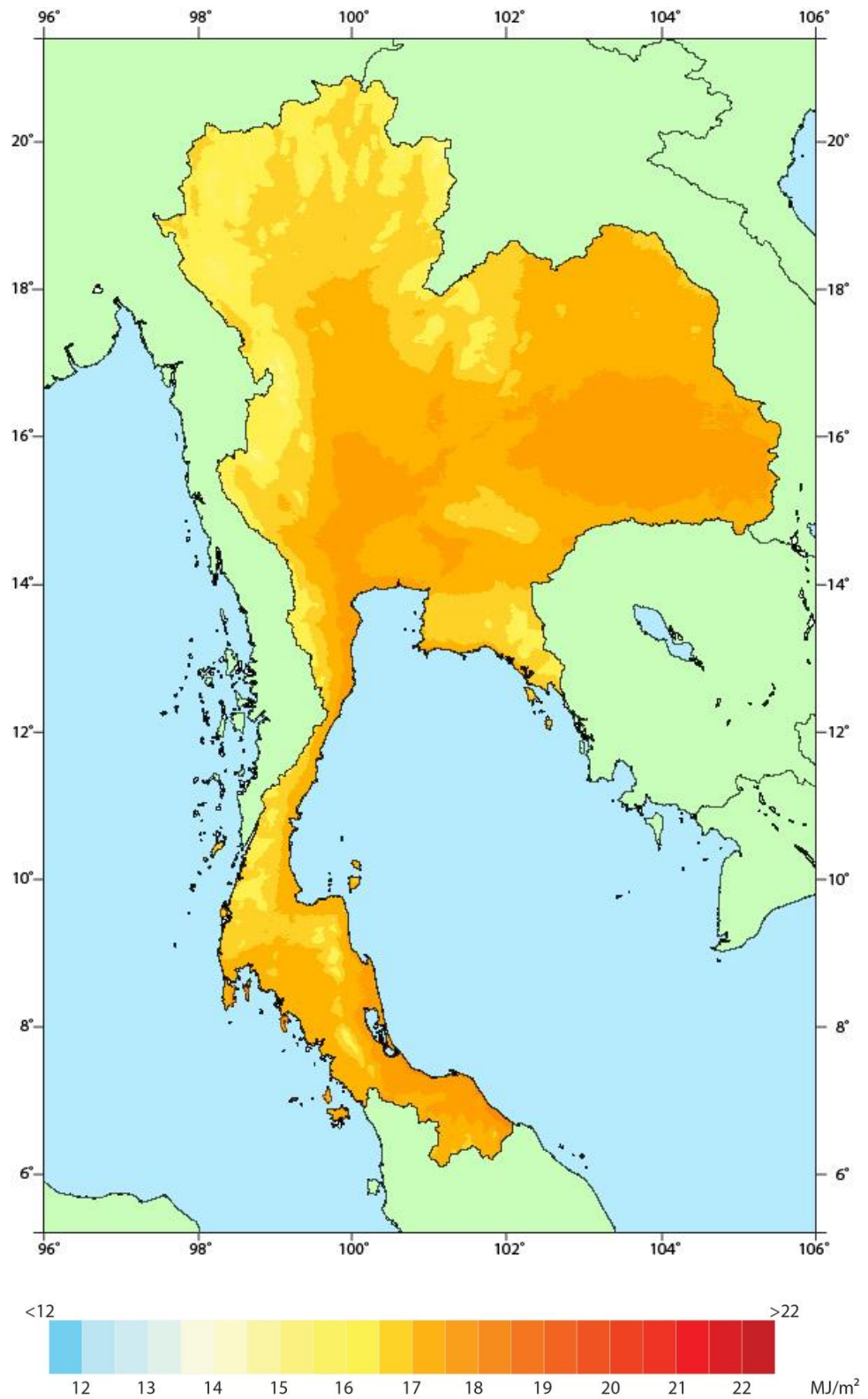
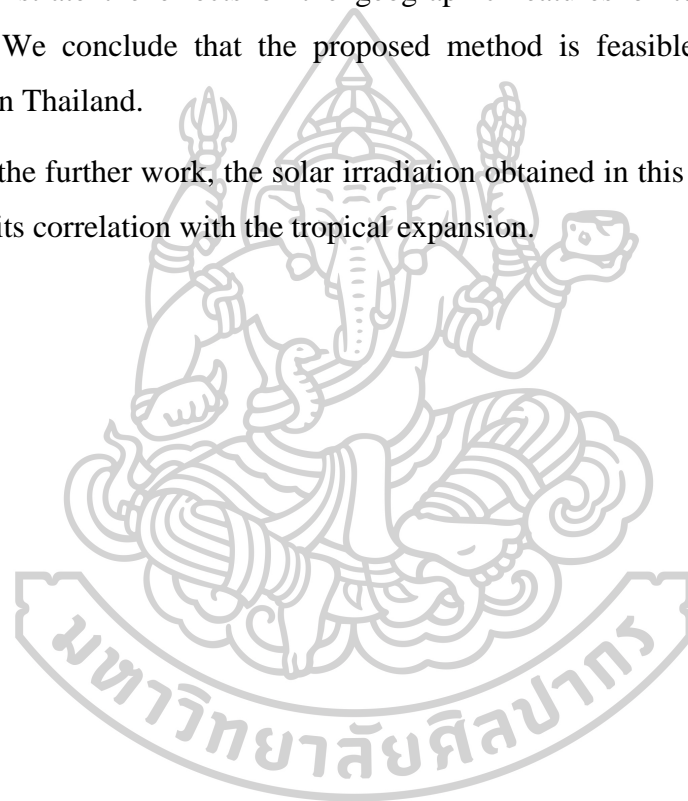


Figure 5 Yearly solar irradiation map of Thailand.

#### 4 Conclusion

An approach to map surface solar irradiation is developed using the calculation of solar irradiation from a simple semi-empirical model. The compositions of the atmosphere affecting the incoming solar irradiation were involved empirically in the model. The data on these compositions are commonly available, thus facilitating the modeling and mapping processes. The model performance is comparable to that of sophisticated models, but the proposed model is relatively simple. Our solar irradiation maps demonstrate the effects of the geographic features of terrains and those of monsoons. We conclude that the proposed method is feasible for mapping solar irradiation in Thailand.

For the further work, the solar irradiation obtained in this study can be used to investigate its correlation with the tropical expansion.



## Appendix 2

### List of publications and conferences

#### Publications

1. **Chanalert, W.**, Buntoung, S., Nunez, M., Itsara, M., Nimnuan, P., Choosri, P., Charuchittipan, D., Janjai, S. & Cao, J. (2022). The Greater Mekong Subregion (GMS) and tropical expansion: A regional study of convection and precipitation. *Advances in Space Research*, 69(6), 2443-2459.
2. **Chanalert, W.**, Janjai, S., & Buntoung, S. (2019, November). An investigation of poleward expansion of the Hadley circulation using cloud cover. In *Journal of Physics: Conference Series* (Vol. 1380, No. 1, p. 012007). IOP Publishing.
3. **Chanalert, W.**, Tohsing, K., Janjai, S. & Panjainam, Y. (Accepted, 14 March 2022). Mapping solar irradiation from ground- and satellite-based data over Thailand using a simple semi-empirical model. *Science, Engineering and Health Studies*.

#### Conferences

1. **Chanalert, W.**, Janjai, S. & Buntoung, S. An investigation of tropical expansion using cloud cover covering longitude range of Thailand. (Oral presentation), RGJ-University Forum, 24 May 2019, Tawana Bangkok Hotel, Thailand.
2. **Chanalert, W.**, Buntoung, S. & Janjai, S. A study of the expansion of Hadley cells from high cloud cover data. (Oral presentation), 10th National Graduate Conference, Silpakorn University, Nakhon Pathom, Thailand.





Figure 1 Partial of the thesis has been published in Advances in Space Research.

## An investigation of poleward expansion of the Hadley circulation using cloud cover

W Chanalert\*, S Janjai and S Buntoung

Laboratory of Tropical Atmospheric Physics, Department of Physics, Faculty of Science, Silpakorn University, Nakhon Pathom 73000, Thailand

\*E-mail: wanlert99@gmail.com

**Abstract.** Amongst the issues associated with global climate change, the expansion of the tropics has become increasingly important. This expansion is normally demonstrated in the form of changes in the Hadley circulation. In this study the changes of the Hadley circulation were investigated using high cloud cover from the ERA-Interim reanalysis data. Trends of zonal-mean cloud cover computed over the period 1979-2017 in both hemispheres show that poleward expansion of the Hadley circulation is about 1.6 and 1.2 degree of latitude per 39 years in northern hemisphere and southern hemisphere, respectively. In addition, the expansion for all four seasons was also analysed. The analysis results show that poleward expansion occurs mostly in all seasons and the expansion of the Hadley circulation results in a poleward expansion of the subtropical dry regions.

### 1. Introduction

The Hadley circulation generally refers to closed cells of the atmospheric circulation between the equator and the subtropics, both in the northern and southern hemispheres. The air rises up near the equator to a height of about 15 km, and then flows toward the north and south poles and sinks in the subtropics. Afterwards the air flows back toward equator along the surface of the Earth. The impacts of this phenomenon can cause more moist air, cloud and rain in the equator region, while subtropical regions are very dry. Thus, the Hadley cells can dominate tropical and subtropical climates. Various studies of the Hadley cell suggested that the tropical zones are poleward expanded since 1979 [1-3]. However, they measured the magnitude of the expansion differently [4] which may be due to the difference of datasets and the length of period. The effects of the tropical expansion may increase drought in subtropical zones and increase floods in the tropical zone. Therefore, it is interesting to study this expansion.

Therefore, the objective of this study is to investigate the expansion of the Hadley cell in both hemispheres. As from the feature of the circulation, in the tropical zones, there are a lot of clouds. In contrast, in the subtropical zones, there is less cloud. Thus, in this work, the variation of cloud cover was used as an indicator of the expansion of the Hadley cells.

### 2. Data

To analyse the expansion of the Hadley circulation, we collected the high cloud cover from the European Centre for Medium-Range Weather Forecasts (ECMWF), denoted by ERA-Interim reanalysis [5]. The monthly high cloud cover data used here is from January 1979 to December 2017 (39 years). The resolution of the data is  $0.25^\circ$  latitude  $\times$   $0.25^\circ$  longitude. The zonal-mean cloud covers

Figure 2 Partial of the thesis has been published in Journal of Physics: Conference Series.

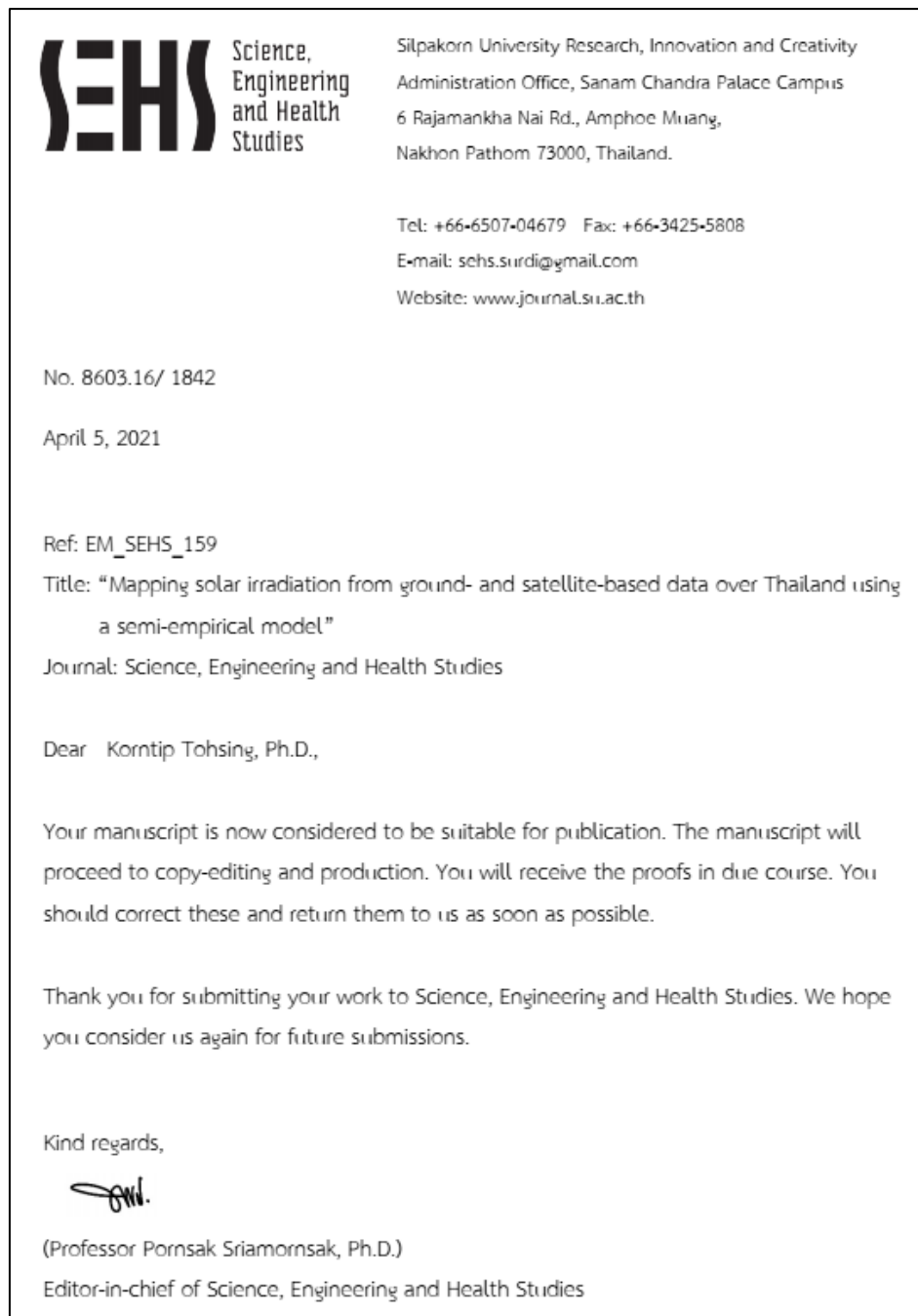


Figure 3 Partial of the thesis has been accepted for publication in Science, Engineering and Health Studies (SEHS).

## **An investigation of tropical expansion using cloud cover covering longitude range of Thailand**

Wanchalerm Chanalert, Serm Janjai, Sumaman Buntoung  
*Laboratory of Tropical Atmospheric Physics, Department of Physics, Faculty of Science, Silpakorn University, Nakhon Pathom 73000, Thailand*

Global climate change causes the expansion of the tropical zone where Thailand is included. In the tropics, there are a lot of clouds near equator region because the air in this region is raised up to the atmosphere. In contrast, the air sinks in the subtropical region, causing less cloud in this region. Consequently, these features of cloud cover can be used to represent the edge of the tropics. Thus, in this work, we investigated tropical expansion using cloud cover as an indicator. In the investigation, monthly cloud cover from the ERA-Interim reanalysis dataset covering the period: 1979-2017 was analyzed. The resolution of cloud cover data used here is  $0.25^\circ$  latitude $\times$  $0.25^\circ$  longitude. The monthly cloud covers were averaged over longitudes of  $90^\circ\text{E}$ - $110^\circ\text{E}$  for each degree of latitude from  $0^\circ$  N- $90^\circ$  N, covering all areas of Thailand. The results show that there is poleward expansion of the tropical zone during 1979-2017 and the expansion was estimated to be approximately  $0.54$  degree of latitude. In addition, the expansion of the tropics for each season was also separately examined and the results reveal that the poleward expansion occurs mostly in all seasons.

**Keywords:** Global climate change, Tropical expansion, Cloud cover

**Selected Reference:**

Hu Y., Zhou C. and Liu J. Observational evidence for poleward expansion of the Hadley circulation. *Advances in Atmospheric Sciences*. 2011; 28(1): 33-44.

Lucas C., Timbal B. and Nguyen H. The expanding tropics: a critical assessment of the observational and modeling studies. *Wiley Interdisciplinary Reviews: Climate Change*. 2014; 5(1): 89-112.



**Wanchalerm Chanalert**

Silpakorn University, Thailand, Physics, B.Sc. 2013

Silpakorn University, Thailand, Physics, M.Sc. 2016

Research field: Tropical atmospheric physics

Figure 4 Partial of the thesis has been presented in RGJ-University Forum conference.

การศึกษาการขยายตัวของแฮดลีย์เซลล์จากข้อมูลปริมาณเมฆชั้นสูง  
A study of the expansion of Hadley cells from high cloud cover data

วันเฉลิม ชนะเลิศ<sup>1</sup> สุมาลย์ บรรเทิง<sup>1</sup> และ เสริม จันทร์ฉาย<sup>1</sup>  
Wanchalerm Chanalert<sup>1</sup> Sumaman Buntoung<sup>1</sup> and Serm Janjai<sup>1</sup>

**บทคัดย่อ**

งานวิจัยนี้ใช้ข้อมูลปริมาณเมฆชั้นสูงที่ได้จากศูนย์พยากรณ์อากาศระยะปานกลางแห่งยุโรป (European Centre for Medium-Range Weather Forecasts, ECMWF) ของเดือนธันวาคมถึงเดือนกุมภาพันธ์ ในปี ค.ศ. 1979 ถึง ปี ค.ศ. 2018 มาวิเคราะห์เพื่อหาขอบของแฮดลีย์เซลล์ซึ่งเป็นการหมุนเวียนของอากาศในแถบเขตร้อนของโลก เพื่อตรวจสอบความถูกต้องของผลที่ได้ ผู้วิจัยจึงทำการเปรียบเทียบขอบของแฮดลีย์เซลล์ที่ได้จากข้อมูลปริมาณเมฆชั้นสูงกับที่ได้จากการคำนวณค่าฟังก์ชันกระแสเชิงมวล (mass stream function) ซึ่งผลที่ได้พบว่ามีความสัมพันธ์กันอยู่ในเกณฑ์ที่ค่อนข้างดี จากนั้นทำการหาขนาดของการขยายตัวของแฮดลีย์เซลล์โดยวิเคราะห์จากกราฟแนวโน้มอนุกรมเวลาของขอบแฮดลีย์เซลล์ที่ได้จากข้อมูลปริมาณเมฆชั้นสูง พบว่าการขยายตัวของเขตร้อนเท่ากับ 6.13 องศาละติจูดในซีกโลกเหนือและ 1.15 องศาละติจูดในซีกโลกใต้

**คำสำคัญ:** ปริมาณเมฆชั้นสูง, แฮดลีย์เซลล์, การขยายตัวของเขตร้อน

**Abstract**

In this work, high cloud cover data from European Centre for Medium-Range Weather Forecasts (ECMWF) (from December to February in 1979 to 2018) were used to investigate the expansion of the Hadley cells, which are the tropical circulation. To verify the result, the edges of Hadley cells obtained from the high cloud cover data were compared with those calculated from the mass stream function. The comparison results show a reasonable agreement. Afterward, the expansion of the edge of the Hadley cells were analyzed using time series of the edge of the Hadley cells from high cloud data. The tropical expansion was found to be 6.13 degree latitude in northern hemisphere and 1.15 degree latitude in southern hemisphere.

Keyword: High cloud cover, Hadley cells, Tropical expansion

<sup>1</sup> ภาควิชาฟิสิกส์ คณะวิทยาศาสตร์ มหาวิทยาลัยศิลปากร นครปฐม 73000 ประเทศไทย  
Department of Physics, Faculty of Science, Silpakorn University, Nakhon Pathom 73000, Thailand.  
การประชุมวิชาการบัณฑิตศึกษาระดับชาติ ครั้งที่ 10

Figure 5 Partial of the thesis has been presented in 10th National Graduate Conference at Silpakorn University, Thailand.

## REFERENCES

- Adeyewa, Z. D., & Nakamura, K. (2003). Validation of TRMM radar rainfall data over major climatic regions in Africa. *Journal of Applied Meteorology*, 42(2), 331-347.
- Ahrens, C. D. (1998). *Meteorology Today: An Introduction to Weather, Climate, and the Environment*. *Meteorologie*, 9(24), 74-75.
- Albright, M. D., Recker, E. E., Reed, R. J., & Dang, R. (1985). The diurnal variation of deep convection and inferred precipitation in the central tropical Pacific during January–February 1979. *Monthly weather review*, 113(10), 1663-1680.
- Allen, R. J., & Ajoku, O. (2016). Future aerosol reductions and widening of the northern tropical belt. *Journal of Geophysical Research: Atmospheres*, 121(12), 6765-6786.
- Allen, R. J., & Kovilakam, M. (2017). The role of natural climate variability in recent tropical expansion. *Journal of Climate*, 30(16), 6329-6350.
- Allen, R. J., Sherwood, S. C., Norris, J. R., & Zender, C. S. (2012). Recent Northern Hemisphere tropical expansion primarily driven by black carbon and tropospheric ozone. *Nature*, 485(7398), 350-354.
- Bates, J. J., Wu, X., & Jackson, D. (1996). Interannual variability of upper-troposphere water vapor band brightness temperature. *Journal of Climate*, 9(2), 427-438.
- Bengtsson, L., Hagemann, S., & Hodges, K. I. (2004). Can climate trends be calculated from reanalysis data? *Journal of Geophysical Research: Atmospheres*, 109(D11).
- Berrisford, P., Kållberg, P., Kobayashi, S., Dee, D., Uppala, S., Simmons, A., Poli, P., & Sato, H. (2011). Atmospheric conservation properties in ERA-Interim. *Quarterly Journal of the royal meteorological society*, 137(659), 1381-1399.
- Bestari, N., Shrestha, S., & Mongcopa, C. (2006). Lao PDR: An evaluation synthesis on rice. A case study from the 2005 Sector Assistance Program evaluation for the agriculture and natural resources sector in the Lao People's Democratic Republic. In: Asian Development Bank, Operations Evaluation Department, Manila ....
- Birner, T., Davis, S. M., & Seidel, D. J. (2014). Earth's tropical belt. *Phys. Today*, 67(12), 38-44.
- Bonan, G. B. (2008). Forests and climate change: forcings, feedbacks, and the climate benefits of forests. *Science*, 320(5882), 1444-1449.
- Bosch, J., Batlles, F., Zarzalejo, L., & López, G. (2010). Solar resources estimation combining digital terrain models and satellite images techniques. *Renewable Energy*, 35(12), 2853-2861.
- Byrne, M. P., & Schneider, T. (2016). Narrowing of the ITCZ in a warming climate: Physical mechanisms. *Geophysical Research Letters*, 43(21), 11,350-311,357.

- Cano, D., Monget, J.-M., Albuissou, M., Guillard, H., Regas, N., & Wald, L. (1986). A method for the determination of the global solar radiation from meteorological satellite data. *Solar energy*, 37(1), 31-39.
- Casella, D., Dietrich, S., Paola, F. D., Formenton, M., Mugnai, A., Porcù, F., & Sanò, P. (2012). PM-GCD—a combined IR–MW satellite technique for frequent retrieval of heavy precipitation. *Natural Hazards and Earth System Sciences*, 12(1), 231-240.
- Chainuvati, C., & Athipanan, W. (2001). Crop diversification in Thailand. *Bangkok, FAO Regional office for Asia and the Pacific*, 130-146.
- Chanalert, W., Buntoung, S., Nunez, M., Itsara, M., Nimnuan, P., Choosri, P., Charuchittipan, D., Janjai, S., & Cao, J. (2022). The Greater Mekong Subregion (GMS) and tropical expansion: A regional study of convection and precipitation. *Advances in Space Research*, 69(6), 2443-2459.
- Charuchittipan, D., Janjai, S., Pretummasoot, N., Buntoung, S., & Peengam, S. (2018). Mapping of cloud cover from satellite data over Thailand. *Science, Engineering and Health Studies*, 69-76.
- Climatological Group, M. D. B., Meteorological Department. (2015). *The Climate of Thailand* [https://www.tmd.go.th/en/archive/thailand\\_climate.pdf](https://www.tmd.go.th/en/archive/thailand_climate.pdf)
- Commission, M. R. (2005). Overview of the Hydrology of the Mekong Basin. *Mekong River Commission, Vientiane*, 82.
- Commission, M. R. (2010). State of the basin report. *Mekong River Commission (MRC)*.
- Commission, M. R. (2018). *State of the Basin Report 2018*. [https://reliefweb.int/sites/reliefweb.int/files/resources/SOBR-v8\\_Final-for-web.pdf](https://reliefweb.int/sites/reliefweb.int/files/resources/SOBR-v8_Final-for-web.pdf)
- Cowan, T., & Cai, W. (2011). The impact of Asian and non-Asian anthropogenic aerosols on 20th century Asian summer monsoon. *Geophysical Research Letters*, 38(11).
- Crocetti, L., Forkel, M., Fischer, M., Jurečka, F., Grlj, A., Salentinig, A., Trnka, M., Anderson, M., Ng, W.-T., & Kokalj, Ž. (2020). Earth Observation for agricultural drought monitoring in the Pannonian Basin (southeastern Europe): current state and future directions. *Regional Environmental Change*, 20(4), 1-17.
- Davis, N., & Birner, T. (2017). On the discrepancies in tropical belt expansion between reanalyses and climate models and among tropical belt width metrics. *Journal of Climate*, 30(4), 1211-1231.
- Davis, S. M., & Rosenlof, K. H. (2012). A multidiagnostic intercomparison of tropical-width time series using reanalyses and satellite observations. *Journal of Climate*, 25(4), 1061-1078.
- Dee, D. P., Uppala, S. M., Simmons, A. J., Berrisford, P., Poli, P., Kobayashi, S., Andrae, U., Balmaseda, M., Balsamo, G., & Bauer, d. P. (2011). The ERA-Interim reanalysis: Configuration and performance of the data assimilation

- system. *Quarterly Journal of the royal meteorological society*, 137(656), 553-597.
- Dhakal, C. P. (2018). Interpreting the basic outputs (SPSS) of multiple linear regression. *International Journal of Science and Research (IJSR)*, 8(6), 1448-1452.
- Duffie, J. A., & Beckman, W. A. (2013). *Solar engineering of thermal processes*. John Wiley & Sons.
- Edwards, D. C., & McKee, T. B. (1997). *Characteristics of 20th Century drought in the United States at multiple time scales*.
- Emerton, R., Cloke, H., Stephens, E., Zsoter, E., Woolnough, S., & Pappenberger, F. (2017). Complex picture for likelihood of ENSO-driven flood hazard. *Nature communications*, 8(1), 1-9.
- Exell, R. (2017). Mapping Solar Radiation by Meteorological Satellite. *International Energy Journal*, 6(1).
- FAO. (2011). *AQUASTAT Country Profile – Thailand*.
- Free, M., Sun, B., & Yoo, H. L. (2016). Comparison between total cloud cover in four reanalysis products and cloud measured by visual observations at US weather stations. *Journal of Climate*, 29(6), 2015-2021.
- Freedman, D., Pisani, R., & Purves, R. (2018). *Statistics* (Fourth edition ed.). WW Norton & Co, New York, United States.
- Fu, Q., Johanson, C. M., Wallace, J. M., & Reichler, T. (2006). Enhanced mid-latitude tropospheric warming in satellite measurements. *Science*, 312(5777), 1179-1179.
- Fu, Q., & Lin, P. (2011). Poleward shift of subtropical jets inferred from satellite-observed lower-stratospheric temperatures. *Journal of Climate*, 24(21), 5597-5603.
- Ganguly, D., Rasch, P. J., Wang, H., & Yoon, J. H. (2012). Climate response of the South Asian monsoon system to anthropogenic aerosols. *Journal of Geophysical Research: Atmospheres*, 117(D13).
- Granato, G. E. (2006). *Kendall-Theil Robust Line (KTRLine-version 1.0): A visual basic program for calculating and graphing robust nonparametric estimates of linear-regression coefficients between two continuous variables*. US Department of the Interior, US Geological Survey.
- Grise, K. M., Davis, S. M., Simpson, I. R., Waugh, D. W., Fu, Q., Allen, R. J., Rosenlof, K. H., Ummenhofer, C. C., Karlsruh, K. B., & Maycock, A. C. (2019). Recent tropical expansion: Natural variability or forced response? *Journal of Climate*, 32(5), 1551-1571.
- Grise, K. M., & Polvani, L. M. (2014). Is climate sensitivity related to dynamical sensitivity? A Southern Hemisphere perspective. *Geophysical Research Letters*, 41(2), 534-540.
- Hahn, C. J., Rossow, W. B., & Warren, S. G. (2001). ISCCP cloud properties associated with standard cloud types identified in individual surface observations. *Journal of Climate*, 14(1), 11-28.



- Halladay, K., Malhi, Y., & New, M. (2012). Cloud frequency climatology at the Andes/Amazon transition: 1. Seasonal and diurnal cycles. *Journal of Geophysical Research: Atmospheres*, 117(D23).
- Heffernan, O. (2016). The mystery of the expanding tropics. *Nature News*, 530(7588), 20.
- Helsel, D., & Hirsch, R. (2002). Statistical Methods in Water Resources Techniques of Water Resources Investigations, Book 4. United States Geological Survey, 522p. In.
- Hirsch, P., Kim, S., So, S., Suon, V., Khiev, D., Neave, M., Griffiths, K., Wales, N., Gillespie, J., & Ham, K. (2008). *Framing research on water resources management and governance in Cambodia: A literature review*.
- Hoanh, C. T., Tuong, T. P., Gallop, K., Gowing, J., Kam, S. P., Khiem, N., & Phong, N. (2003). Livelihood impacts of water policy changes: evidence from a coastal area of the Mekong River Delta. *Water Policy*, 5(5-6), 475-488.
- Hoerling, M., Eischeid, J., & Perlwitz, J. (2010). Regional precipitation trends: Distinguishing natural variability from anthropogenic forcing. *Journal of Climate*, 23(8), 2131-2145.
- Hu, Y., & Fu, Q. (2007). Observed poleward expansion of the Hadley circulation since 1979. *Atmospheric Chemistry and Physics*, 7(19), 5229-5236.
- Hu, Y., Huang, H., & Zhou, C. (2018). Widening and weakening of the Hadley circulation under global warming. *Science Bulletin*, 63(10), 640-644.
- Hu, Y., Zhou, C., & Liu, J. (2011). Observational evidence for poleward expansion of the Hadley circulation. *Advances in Atmospheric Sciences*, 28(1), 33-44.
- Huang, G., Li, Z., Li, X., Liang, S., Yang, K., Wang, D., & Zhang, Y. (2019). Estimating surface solar irradiance from satellites: Past, present, and future perspectives. *Remote Sensing of Environment*, 233, 111371.
- Hudson, R., Andrade, M., Follette, M., & Frolov, A. (2006). The total ozone field separated into meteorological regimes—Part II: Northern Hemisphere mid-latitude total ozone trends. *Atmospheric Chemistry and Physics*, 6(12), 5183-5191.
- Iqbal, M. (1983). *An Introduction to Solar Radiation*. Academic Press, New York. <https://doi.org/https://doi.org/10.1016/B978-0-12-373750-2.X5001-0>
- Issac, J., & Turton, S. (2014). Expansion of the tropics—evidence and implications In: State of the tropics 2014 report. *James Cook University, Cairnes, Australia*.
- Janjai, S. (2007). *Assessment of Solar Energy Potentials for Lao People's Democratic Republic*. B. Department of Alternative Energy Development and Efficiency of Thailand.
- Janjai, S. (2009). *Assessment of Solar Energy Potentials for Myanmar*. B. Department of Alternative Energy Development and Efficiency of Thailand.

- Janjai, S., Laksanaboonsong, J., Nunez, M., & Thongsathitya, A. (2005). Development of a method for generating operational solar radiation maps from satellite data for a tropical environment. *Solar energy*, 78(6), 739-751.
- Janjai, S., Masiri, I., Pattarapanitchai, S., & Laksanaboonsong, J. (2013). Mapping global solar radiation from long-term satellite data in the tropics using an improved model. *International Journal of Photoenergy*, 2013.
- Janjai, S., Nimnuan, P., Nunez, M., Buntoung, S., & Cao, J. (2015). An assessment of three satellite-based precipitation data sets as applied to the Thailand region. *Physical Geography*, 36(4), 282-304.
- Johanson, C. M., & Fu, Q. (2009). Hadley cell widening: Model simulations versus observations. *Journal of Climate*, 22(10), 2713-2725.
- Kämpfer, N. (2013). *Monitoring atmospheric water vapour: ground-based remote sensing and in-situ methods* (Vol. 10). Springer, New York.  
<https://doi.org/https://doi.org/10.1007/978-1-4614-3909-7>
- Kim, M. K., Lau, W. K., Kim, K. M., & Lee, W. S. (2007). A GCM study of effects of radiative forcing of sulfate aerosol on large scale circulation and rainfall in East Asia during boreal spring. *Geophysical Research Letters*, 34(24).
- Kovilakam, M., & Mahajan, S. (2016). Confronting the “Indian summer monsoon response to black carbon aerosol” with the uncertainty in its radiative forcing and beyond. *Journal of Geophysical Research: Atmospheres*, 121(13), 7833-7852.
- Lanzante, J. R., & Gahrs, G. E. (2000). The “clear-sky bias” of TOVS upper-tropospheric humidity. *Journal of Climate*, 13(22), 4034-4041.
- Lau, K., Kim, M., & Kim, K. (2006). Asian summer monsoon anomalies induced by aerosol direct forcing: the role of the Tibetan Plateau. *Climate dynamics*, 26(7-8), 855-864.
- Lau, W. K., & Kim, K.-M. (2015). Robust Hadley circulation changes and increasing global dryness due to CO2 warming from CMIP5 model projections. *Proceedings of the National Academy of Sciences*, 112(12), 3630-3635.
- Liu, J., Song, M., Hu, Y., & Ren, X. (2012). Changes in the strength and width of the Hadley circulation since 1871. *Climate of the Past*, 8(4), 1169-1175.
- Liu, Z., Ostrenga, D., Teng, W., & Kempler, S. (2012). Tropical Rainfall Measuring Mission (TRMM) precipitation data and services for research and applications. *Bulletin of the American Meteorological Society*, 93(9), 1317-1325.
- Lu, J., Vecchi, G. A., & Reichler, T. (2007). Expansion of the Hadley cell under global warming. *Geophysical Research Letters*, 34(6).
- Lucas, C., & Nguyen, H. (2015). Regional characteristics of tropical expansion and the role of climate variability. *Journal of Geophysical Research: Atmospheres*, 120(14), 6809-6824.

- Lucas, C., Timbal, B., & Nguyen, H. (2014). The expanding tropics: A critical assessment of the observational and modeling studies. *Wiley Interdisciplinary Reviews: Climate Change*, 5(1), 89-112.
- Manney, G. L., & Hegglin, M. I. (2018). Seasonal and regional variations of long-term changes in upper-tropospheric jets from reanalyses. *Journal of Climate*, 31(1), 423-448.
- Manney, G. L., Hegglin, M. I., Lawrence, Z. D., Wargan, K., Millán, L. F., Schwartz, M. J., Santee, M. L., Lambert, A., Pawson, S., & Knosp, B. W. (2017). Reanalysis comparisons of upper tropospheric–lower stratospheric jets and multiple tropopauses. *Atmospheric Chemistry and Physics*, 17(18), 11541-11566.
- Mantsis, D. F., Sherwood, S., Allen, R., & Shi, L. (2017). Natural variations of tropical width and recent trends. *Geophysical Research Letters*, 44(8), 3825-3832.
- Mantua, N. J., Hare, S. R., Zhang, Y., Wallace, J. M., & Francis, R. C. (1997). A Pacific interdecadal climate oscillation with impacts on salmon production. *Bulletin of the American Meteorological Society*, 78(6), 1069-1080.
- Marks, D. (2011). Climate change and Thailand: Impact and response. *Contemporary Southeast Asia: A Journal of International and Strategic Affairs*, 33(2), 229-258.
- McKee, T. B., Doesken, N. J., & Kleist, J. (1993). The relationship of drought frequency and duration to time scales. Proceedings of the 8th Conference on Applied Climatology,
- Meehl, G. A., Arblaster, J. M., & Collins, W. D. (2008). Effects of black carbon aerosols on the Indian monsoon. *Journal of Climate*, 21(12), 2869-2882.
- Möser, W., & Raschke, E. (1984). Incident solar radiation over Europe estimated from METEOSAT data. *Journal of Applied Meteorology and Climatology*, 23(1), 166-170.
- Nguyen, H., Evans, A., Lucas, C., Smith, I., & Timbal, B. (2013). The Hadley circulation in reanalyses: Climatology, variability, and change. *Journal of Climate*, 26(10), 3357-3376.
- Oldeman, L., & Frere, M. (1982). *Technical Report on a Study of the Agroclimatology of the Humid Tropics of Southeast Asia*. Food & Agriculture Org.
- Pinker, R., & Laszlo, I. (1992). Modeling surface solar irradiance for satellite applications on a global scale. *Journal of Applied Meteorology and Climatology*, 31(2), 194-211.
- Polo, J. (2015). Solar global horizontal and direct normal irradiation maps in Spain derived from geostationary satellites. *Journal of Atmospheric and Solar-Terrestrial Physics*, 130, 81-88.
- Polo, J., Zarzalejo, L., Cony, M., Navarro, A., Marchante, R., Martin, L., & Romero, M. (2011). Solar radiation estimations over India using Meteosat satellite images. *Solar energy*, 85(9), 2395-2406.

- Prasetya, R., As-syakur, A. R., & Osawa, T. (2013). Validation of TRMM Precipitation Radar satellite data over Indonesian region. *Theoretical and applied climatology*, 112(3), 575-587.
- Press, W. H., Teukolsky, S. A., Flannery, B. P., & Vetterling, W. T. (1992). *Numerical recipes in Fortran 77: volume 1, volume 1 of Fortran numerical recipes: the art of scientific computing*. Cambridge university press.
- Quan, X.-W., Hoerling, M. P., Perlwitz, J., Diaz, H. F., & Xu, T. (2014). How fast are the tropics expanding? *Journal of Climate*, 27(5), 1999-2013.
- Reichler, T. (2009). Changes in the atmospheric circulation as indicator of climate change. In *Climate Change* (pp. 145-164). Elsevier.
- Rienecker, M. M., Suarez, M., Todling, R., Bacmeister, J., Takacs, L., Liu, H., Gu, W., Sienkiewicz, M., Koster, R., & Gelaro, R. (2008). The GEOS-5 Data Assimilation System: Documentation of Versions 5.0. 1, 5.1. 0, and 5.2. 0.
- Ropelewski, C. F., & Jones, P. D. (1987). An extension of the Tahiti–Darwin southern oscillation index. *Monthly weather review*, 115(9), 2161-2165.
- Salby, M. L. (1996). *Fundamentals of atmospheric physics*. Elsevier.
- Schiffer, R. A., & Rossow, W. B. (1983). The International Satellite Cloud Climatology Project (ISCCP): The first project of the world climate research programme. *Bulletin of the American Meteorological Society*, 64(7), 779-784.
- Schmidt, D. F., & Grise, K. M. (2017). The response of local precipitation and sea level pressure to Hadley cell expansion. *Geophysical Research Letters*, 44(20), 10,573-510,582.
- Seager, R., Naik, N., & Vecchi, G. A. (2010). Thermodynamic and dynamic mechanisms for large-scale changes in the hydrological cycle in response to global warming. *Journal of Climate*, 23(17), 4651-4668.
- Seidel, D., Fu, Q., Randel, W., & Reichler, T. (2007). Widening of the tropical belt in a changing climate. *Nat. Geosci.*, 1, 21–24. In.
- Seidel, D. J., Fu, Q., Randel, W. J., & Reichler, T. J. (2008). Widening of the tropical belt in a changing climate. *Nature geoscience*, 1(1), 21-24.
- Seidel, D. J., & Randel, W. J. (2007). Recent widening of the tropical belt: Evidence from tropopause observations. *Journal of Geophysical Research: Atmospheres*, 112(D20).
- Shi, L., & Bates, J. J. (2011). Three decades of intersatellite-calibrated High-Resolution Infrared Radiation Sounder upper tropospheric water vapor. *Journal of Geophysical Research: Atmospheres*, 116(D4).
- Shi, L., Schreck III, C., & John, V. (2013). HIRS channel 12 brightness temperature dataset and its correlations with major climate indices. *Atmospheric Chemistry and Physics*, 13(14), 6907-6920.
- Simmons, A. (2006). ERA-Interim: New ECMWF reanalysis products from 1989 onwards. *ECMWF newsletter*, 110, 25-36.

- Soden, B. J., & Bretherton, F. P. (1993). Upper tropospheric relative humidity from the GOES 6.7  $\mu\text{m}$  channel: Method and climatology for July 1987. *Journal of Geophysical Research: Atmospheres*, 98(D9), 16669-16688.
- Soden, B. J., & Lanzante, J. R. (1996). An assessment of satellite and radiosonde climatologies of upper-tropospheric water vapor. *Journal of Climate*, 9(6), 1235-1250.
- Solomon, A., Polvani, L., Waugh, D., & Davis, S. (2016). Contrasting upper and lower atmospheric metrics of tropical expansion in the Southern Hemisphere. *Geophysical Research Letters*, 43(19), 10,496-410,503.
- Sorapipatana, C., Exell, R., & Borel, D. (1988). A bispectral method for determining global solar radiation from meteorological satellite data. *Solar & wind technology*, 5(3), 321-327.
- Staten, P. W., Lu, J., Grise, K. M., Davis, S. M., & Birner, T. (2018). Re-examining tropical expansion. *Nature Climate Change*, 8(9), 768-775.
- Suwantragul, B. (1984). *Solar and wind energy potential assessment of Thailand*. Meteorological Department, Ministry of Communications, and King Mongkut's Institute of Technology, Thonburi Campus, Bangkok, Thailand.
- Titapiwatanakun, B. (2012). The rice situation in Thailand. *Technical Assistance Consultant's Report, TA-REG, 74595*.
- Tselioudis, G., Lipat, B. R., Konsta, D., Grise, K. M., & Polvani, L. M. (2016). Midlatitude cloud shifts, their primary link to the Hadley cell, and their diverse radiative effects. *Geophysical Research Letters*, 43(9), 4594-4601.
- Van Dau, Q., Kuntiyawichai, K., & Suryadi, F. (2017). Drought severity assessment in the lower Nam Phong river basin, Thailand. *Songklanakarin J. Sci. Technol*, 40, 985-992.
- Wang, L., & Chen, W. (2014). An intensity index for the East Asian winter monsoon. *Journal of Climate*, 27(6), 2361-2374.
- Waugh, D. W., Grise, K., Seviour, W., Davis, S., Davis, N., Adam, O., Son, S.-W., Simpson, I., Staten, P., & Maycock, A. (2018). Revisiting the relationship among metrics of tropical expansion. *Journal of Climate*, 31(18), 7565-7581.
- Wolff, D. B., Marks, D., Amitai, E., Silberstein, D., Fisher, B., Tokay, A., Wang, J., & Pippitt, J. (2005). Ground validation for the tropical rainfall measuring mission (TRMM). *Journal of Atmospheric and Oceanic Technology*, 22(4), 365-380.
- Worku, L. Y., Mekonnen, A., & Schreck III, C. J. (2019). Diurnal cycle of rainfall and convection over the Maritime Continent using TRMM and ISCCP. *International Journal of Climatology*, 39(13), 5191-5200.
- Wyser, K., O'Hirok, W., Gautier, C., & Jones, C. (2002). Remote sensing of surface solar irradiance with corrections for 3-D cloud effects. *Remote Sensing of Environment*, 80(2), 272-284.
- Xia, Y., Hu, Y., & Liu, J. (2020). Comparison of trends in the Hadley circulation between CMIP6 and CMIP5. *Science Bulletin*, 65(19), 1667-1674.

- Yang, S., & Lau, K. (1998). Influences of sea surface temperature and ground wetness on Asian summer monsoon. *Journal of Climate*, 11(12), 3230-3246.
- You, Q., Jiang, Z., Bao, Y., Pepin, N., & Fraedrich, K. (2016). Trends in upper tropospheric water vapour over the Tibetan Plateau from remote sensing. *International Journal of Climatology*, 36(15), 4862-4872.
- You, Q., Min, J., Kang, S., & Pepin, N. (2015). Poleward expansion of the tropical belt derived from upper tropospheric water vapour. *International Journal of Climatology*, 35(9), 2237-2242.
- Zhou, W., Xie, S.-P., & Yang, D. (2019). Enhanced equatorial warming causes deep-tropical contraction and subtropical monsoon shift. *Nature Climate Change*, 9(11), 834-839.





## VITA

**NAME** Wanchalerm Chanalert

**DATE OF BIRTH** 21 August 1991

**PLACE OF BIRTH** Bangkok

**INSTITUTIONS ATTENDED** 2014, Bachelor of Science (Physics) Silpakorn University, Nakhon Pathom Thailand.  
2017, Master of Science (Physics) Silpakorn University, Nakhon Pathom Thailand.

**HOME ADDRESS** 74/1, Tambon khaokhlung, Amphur Banpong, Ratchaburi 70110

